View metadata, citation and similar papers at core.ac.uk

brought to you by CORE

provided by Digital Commons@Wayne State University

DIGITALCOMMONS @WAYNESTATE

Wayne State University

Wayne State University Dissertations

1-1-2018

Reliability Analysis By Considering Steel Physical Properties

Wujun Si
Wayne State University,

Follow this and additional works at: https://digitalcommons.wayne.edu/oa_dissertations

Part of the Industrial Engineering Commons

Recommended Citation
Si, Wujun, "Reliability Analysis By Considering Steel Physical Properties" (2018). *Wayne State University Dissertations*. 2070.
https://digitalcommons.wayne.edu/oa_dissertations/2070

This Open Access Dissertation is brought to you for free and open access by DigitalCommons@WayneState. It has been accepted for inclusion in Wayne State University Dissertations by an authorized administrator of DigitalCommons@WayneState.

RELIABILITY ANALYSIS BY CONSIDERING STEEL PHYSICAL PROPERTIES

by

WUJUN SI

DISSERTATION

Submitted to the Graduate School

Of Wayne State University,

Detroit, Michigan

in partial fulfillment of the requirements

for the degree of

DOCTOR OF PHILOSOPHY

2018

Major: INDUSTRIAL ENGINEERING

Approved By:

_____

Advisor Date

_____

_____

_____

_____

© COPYRIGHT BY

WUJUN SI

2018

All Rights Reserved

DEDICATION

To my parents

ACKNOWLEDGMENTS

This thesis would not have been possible without the advice, support and help from several people. First and foremost, I would like to express my special appreciation and gratitude to my advisor Dr. Qingyu Yang, who has enthusiastically and continuously guided/supported me in my PhD study, research, and career development. I am also grateful to my co-advisor Dr. Xin Wu from the department of mechanical engineering, who has helped me build up solid knowledge and skills of mechanics and materials science.

Moreover, I would like to thank Dr. Leslie Monplaisir for his tremendous support during my PhD study in the ISE department as well as in my faculty job application. I would also like to extend my thanks and appreciations to Dr. Saravanan Venkatachalam and Dr. Dajun Zhou, who have served as my dissertation committee members, for their valuable comments and constructive suggestions on this thesis work.

In the end, I would like to thank my parents and brother for their endless love and support.

TABLE OF CONTENTS

DEDICATION ii

ACKNOWLEDGMENTS iii

LIST OF TABLES vii

LIST OF FIGURES viii

CHAPTER 1. INTRODUCTION 1

1.1 Background and Motivation 1

1.2 Literature Work 2

1.3 Dissertation Objective 4

1.4 Dissertation Organization 5

CHAPTER 2. RELIABILITY ANALYSIS BY CONSIDERING STEEL MACRO-SCALE OVERLOAD RETARDATION PROPERTY 6

2.1 Overview 6

2.2 Introduction 6

2.3 Physical-Statistical Model 11

2.4 Model Parameter Estimation 15

2.4.1 Likelihood Function 15

2.4.2 Model Approximation in the Physical Domain 16

2.4.3 Estimation of $\boldsymbol{\theta}$ and Its Standard Errors 19

2.5 Testing of Material Property Subject to an Overload 20

2.6 Application to Reliability Estimation 21

2.7 Case Study 24

2.7.1 Parameter Estimation 25

2.7.2 Overload Property Testing 27

2.7.3 Reliability Estimation 27

2.8 Summary 29

CHAPTER 3. RELIABILITY ANALYSIS BY CONSIDERING STEEL LOCAL-SCALE DYNAMIC DEFORMATION 31

3.1 Overview 31

3.2 Introduction 31

3.3 Statistical Model 36

3.3.1 Multivariate General Path Model 37

3.3.2 Two-stage Model Parameter Estimation 38

3.4 Variance-based Failure Criterion 41

3.5 Reliability Analysis 42

3.5.1 Multivariate Linear Path Model 43

3.5.2 Special Nonlinear Multivariate Path Models 47

3.5.2.1 Multivariate Power Law Path Model 47

3.5.2.2 Multivariate Exponential Path Model 48

3.5.3 Multivariate General Path Model 49

3.6 Simulation Study 50

3.7 Case Study 54

3.8 Summary 57

CHAPTER 4. RELIABILITY ANALYSIS BY CONSIDERING STEEL MICROSTRUCTURE INFORMATION 59

4.1 Overview 59

4.2 Introduction 59

4.3 Statistical Model 62

4.3.1 The Two-point Correlation Function 63

4.3.2 A Novel Distribution-based Functional Linear Model 65

4.4 Model Parameter Estimation 68

4.5 Simulation Study 73

4.6 Case Study 77

4.7 Summary 81

CHAPTER 5. GENERAL CONCLUSIONS 83

APPENDIX 1. Proof of Proposition 1 86

APPENDIX 2. Proof of Proposition 2 87

APPENDIX 3. Asymptotic Analysis of the Two-stage Parameter Estimation Method …….. 91

APPENDIX 4. Proof of Proposition 3 92

APPENDIX 5. Proof of Proposition 4 94

APPENDIX 6. Proof of Proposition 5 95

APPENDIX 7. Proof of Corollary 1 96

APPENDIX 8. Proof of Corollary 2 97

APPENDIX 9. Proof of Theory 1 98

APPENDIX 10. Proof of Theory 2 100

REFERENCES 103

ABSTRACT 118

AUTOBIOGRAPHICAL STATEMENT 120

LIST OF TABLES

Table 2.1: Estimated model parameters and standard errors in case study ……..… 26

Table 2.2: Result of overload retardation property testing ……...… 27

Table 3.1: RMSEs of parameter estimators ……...…… 53

Table 4.1: Estimated model parameters and standard errors for a simulated data set ……. 75

Table 4.2: Estimated model parameters and standard errors for the experimental data set …. 79

LIST OF FIGURES

Figure 2.1: Crack length – cumulative number of loading cycles curves 8

Figure 2.2: Crack growth modeling in physical and time domains 12

Figure 2.3: Crack growth rate vs. range of stress intensity factor (log-scale) in physical domain 14

Figure 2.4: Illustration of physical domain modeling (left) and its approximation (right) 17

Figure 2.5: Instron 8801 testing system (left) and the compact tension specimen (right) 25

Figure 2.6: The observed crack propagation path vs. the model crack propagation path 26

Figure 2.7: The estimated failure time CDF and the 95% pointwise confidence intervals 28

Figure 3.1: Plate deformation over time 32

Figure 3.2: Deformation over time paths of one plate sample 36

Figure 3.3: Instron 8801 testing system (left) and deformation paths of a sample (right) 42

Figure 3.4: Simulated deformation paths of ten samples 52

Figure 3.5: Reliability functions for two failure thresholds and the corresponding 95% PCIs 56

Figure 4.1: High strength dual-phase steel (left) and its microstructure image (right) 60

Figure 4.2: The framework of lifetime prediction using material microstructure image 63

Figure 4.3: Estimated vs. true functional coefficients 74

Figure 4.4: Error of parameter estimates vs. sample size 76

Figure 4.5: Lifetime parameter estimates vs. number of basis functions 77

Figure 4.6: Instron 8801 testing machine (left), a failed DP steel sample (middle) and a microstructure image (right) 78

Figure 4.7: Estimated functional coefficients 80

Figure 4.8: Lifetime distribution prediction for a DP steel sample 81

CHAPTER 1. INTRODUCTION

1.1 Background and Motivation

Reliability assessment and failure prediction of materials/assets are receiving increasing attention in modern industries such as the automotive industry, steel industry, and aircraft industry. General purposes of reliability analysis include field life prediction [1], residual/remaining life assessment [2], accelerated life testing [3], maintenance planning [4, 5], etc. Effective reliability analysis not only remarkably improves assets' reliability performance estimation and failure prediction but also contributes to making more efficient maintenance policies which can significantly lower the assets' operational cost. As a result, more and more investment has been devoted to pursue a high degree of reliability evaluation accuracy in recent years.

In materials science, it has been shown that material physical properties significantly impact materials reliability and failure. For example, steels with higher strength and toughness oftentimes demonstrate longer service lifetimes when they are subject to mechanical force loadings. Rocks with a larger volume fraction of porosity usually are more prone to crack failures. Composite materials with fibers that have a larger Young's modulus may exhibit a higher overall strength and thus are less susceptible to failure. In this dissertation research, we shall focus on studying three steel physical properties of various scales that significantly impact steel reliability. That is, 1) a macro-scale property called overload retardation; 2) a local-scale property called dynamic local deformation; and 3) a micro-scale property called microstructure effect. More specifically, property 1) takes effect under a context of crack propagation subject to fatigue loading. When loads are not exactly cyclic either due to environmental randomness

or artificial designs, those with amplitudes higher than a threshold limit are referred to as overloads. Researchers have revealed that for some materials overloads decelerate rather than accelerate the crack propagation process. Such counterintuitive effect is called overload retardation. Property 2) regards a dynamic deformation process of a material when it is subject to force loadings, and local deformation is defined as the displacements of various local points of the material. Local deformation contains richer information compared to global deformation (such as overall elongation) and more fundamentally determines material failures. In property 3), material microstructure refers to a small scale structure of a material, defined as the structure of a prepared material surface as revealed by a microscope using a magnification no less than 25×. Material microstructure has been shown to strongly influence material macroscopic properties such as strength, hardness, toughness, and wear resistance, which in turn affect material service lifetime. As a result, reliability analysis of steels could be significantly biased if we ignore properties 1) - 3).

As physical properties 1) - 3) have strong impacts on steel reliability, in this dissertation we aim at developing systematic and effective methodologies to incorporate them into steel reliability analysis.

1.2 Literature Work

In reliability engineering, most existing analyses have been conducted based on two types of data, termed time-to-failure/lifetime data [6] and degradation data [7]. Examples of lifetime based reliability analysis (possibly subject to time censoring) can be found in [3, 8-11]. When covariates such as environmental variables and stress/loading conditions are available, covariate adjusted lifetime analyses are developed in various application fields, e.g., see Hong

and Meeker [6], Zhao and Elsayed [3], and Si and Yang [12]. Compared to time-to-failure data, degradation data often provide more useful information in assessing asset reliability as they present detailed deterioration paths to failure rather than report the final failure times. Common examples of degradation data (over time) include the crack growth on a plate, the deformation of a material, the fatigue damage of a mechanical structure, the light output from an LED array, and the power capacity of a battery. Statistical methods for degradation data analysis mainly include the general path model [7] and stochastic process models such as Wiener process [13], gamma process [14], and Inverse Gaussian (IG) process [15]. In addition to degradation measurements, some other useful data may also be simultaneously recorded, e.g., environmental conditions (temperature, voltage, humidity, etc.), loading conditions (loading force, loading frequency, etc.) and material property information (strength, toughness, hardness, etc.). These data are termed as covariates and contain valuable information in assessing asset degradation. Incorporating covariates into degradation analysis has been shown to result in more accurate reliability estimation and more efficient maintenance planning, e.g., see Liao and Tian [16] and Chen*, et al.* [17]. Although a large amount of model-based and data-driven methods have been proposed for product reliability evaluation, none of the existing studies quantitatively incorporates properties 1) - 3) into material reliability modeling.

In materials science, properties 1) - 3) have been widely studied with focuses on their mechanism explanations/interpretations, mechanical effects, experimental designs, and impacts on material failures. Often physical models and finite element methods (FEM) are utilized to model the aforementioned properties. For examples of investigations on overload retardation, one can refer to Lankford and Davidson [18], Daneshpour*, et al.* [19], and

Dominguez*, et al.* [20]. For the material local deformation, some literature works can be found in Hashimoto*, et al.* [21], Kolednik [22], and Springmann and Kuna [23]. For material microstructure analysis, examples of studies include Modi*, et al.* [24], Sarwar and Priestner [25], and Carpinteri [26]. However, most existing studies do not quantitatively link properties 1) - 3) to material time-to-failure/lifetime, and they often do not consider failure uncertainties of materials that widely exist in real applications. Moreover, many aforementioned studies also ignore measurement errors in their modeling.

As properties 1) - 3) strongly impact material failures, material reliability analysis without considering them could result in significant bias, and material lifetime inference may also be strongly distorted in some situations. The major challenges of incorporating properties 1) - 3) into material reliability estimation are three-fold. First, there is no existing quantitative physical equations/models to directly link material lifetime with the three physical properties. Second, the quantitative modeling of the three properties themselves is difficult. Third, it is challenging to incorporate the failure uncertainties and measurement errors into reliability modeling.

1.3 Dissertation Objective

In this dissertation, the objective is to develop systematic and quantitative methodologies for steel reliability analysis by incorporating physical properties 1) - 3). Failure uncertainties and measurement errors are considered in the proposed modeling. More specifically, the key points of the objective are listed as follows:

a) Develop efficient statistical/physical-statistical methods to characterize or extract features from material properties 1) - 3);

b) By applying results of (b), build statistical models to establish quantitative relationships

between material properties 1) - 3) (or the extracted features) and material reliability/failure;

c) Investigate theoretical properties of the proposed methodologies through statistical inferences as well as simulation studies;

d) Design and conduct appropriate physical experiments, and then apply the proposed methodologies to demonstrate their real application performances.

1.4 Dissertation Organization

This dissertation consists of three major chapters, preceded by the current introduction chapter (i.e., CHAPTER 1) and followed by a conclusion (i.e., CHAPTER 5). Specifically, in CHAPTER 2 a novel physical-statistical model is proposed for steel reliability estimation by incorporating the macro-scale overload retardation property. In CHAPTER 3, a novel multivariate general path model is proposed for reliability analysis by considering the local-scale steel dynamic deformation property. In CHAPTER 4, a novel distribution-based functional linear model is proposed for reliability analysis by utilizing steel microstructure image information.

CHAPTER 2. RELIABILITY ANALYSIS BY CONSIDERING STEEL MACRO-SCALE OVERLOAD RETARDATION PROPERTY

2.1 Overview

Crack propagation subjected to fatigue loading has been widely studied under the assumption that loads are ideally cyclic with a constant amplitude. In the real world, often loads are not exactly cyclic either due to environmental randomness or artificial designs. Loads with amplitudes higher than a threshold limit are referred to as overloads. Researchers have revealed that for some materials overloads decelerate rather than accelerate the crack propagation process. This effect is called overload retardation. Ignoring overload retardation in reliability analysis can result in a biased estimation of product life. In the literature, however, research on overload retardation mainly focuses on studying its mechanical properties without modeling the effect quantitatively and therefore cannot be incorporated into reliability analysis of fatigue failures. In this chapter, we propose a physical-statistical model to quantitatively describe overload retardation considering random errors. A maximum likelihood estimation approach is developed to estimate the model parameters. In addition, a likelihood ratio test is developed to determine whether a tested material has an overload retardation or overload acceleration effect. The proposed model is further applied to reliability estimation of crack failures when a material has the overload retardation effect. Specifically, two algorithms are developed to calculate the cumulative distribution function of time-to-failure and the corresponding pointwise confidence intervals. Finally, designed experiments using 304 stainless steel are conducted to verify and illustrate the developed methods along with simulation studies.

2.2 Introduction

Fatigue failure has been widely studied in the literature as approximately 90% of

mechanical failures are due to the presence of material fatigue [27]. Examples of fatigue failures in history include the Silver Bridge collapse [28], the German ICE train accident [29], the Liberty ship fracture [30], etc. Crack propagation induced by fatigue loads, which results in fatigue failure, has been investigated in both mechanical and statistical fields. In the mechanical field, most of the existing research focuses on studying the mechanical properties of fatigue crack propagation. Ritchie [31] reviewed various types of mechanisms and theories of fatigue crack propagation proposed by researchers. Based on these mechanical theories, numerical simulation models [32] and finite element models [33] were also developed to delineate fatigue crack propagation. In the statistical field, stochastic processes such as the Markov process [34], Semi-Markov Process [35], and gamma process [36] were used to describe the fatigue crack propagation. Furthermore, statistical degradation models [37] were also applied to characterize the crack propagation as a crack propagation (over time) path can be treated as a degradation path.

Most of the existing research on fatigue crack propagation assumes that fatigue loads are ideally cyclic with a constant amplitude. In this situation, the crack propagation can be modeled by the Paris law [38] as follows.

$$\frac{da}{dN} = c\left(\Delta K\right)^{m} \tag{1}$$

where N is the cumulative number of fatigue loading cycles; a is the crack length; da/dN represents the crack growth rate; c and m are material parameters; and ΔK is the range of stress intensity factor, a physical descriptor of the stress intensity fluctuation at the crack tip during a loading cycle.

In the real world, however, either due to environmental randomness or as a result of

artificial designs, fatigue loads may not be ideally cyclic. Loads with amplitudes exceeding a threshold limit are referred to as overloads. In the literature, it has been found that for some materials overloads decelerate rather than accelerate crack propagation [39]. This counter-intuitive effect is called overload retardation.

Figure 2.1 depicts three possible types of crack propagation paths when an overload occurs at cycle N_0: curve 1 shows an accelerated crack propagation process when the material has an overload acceleration effect, curve 2 presents a decelerated crack propagation process when the material has an overload retardation effect, and curve 3 illustrates a crack propagation process following the conventional Paris law when the material has neither overload retardation nor overload acceleration effect. The material effect represented by curve 3 is called overload stationary in this chapter.

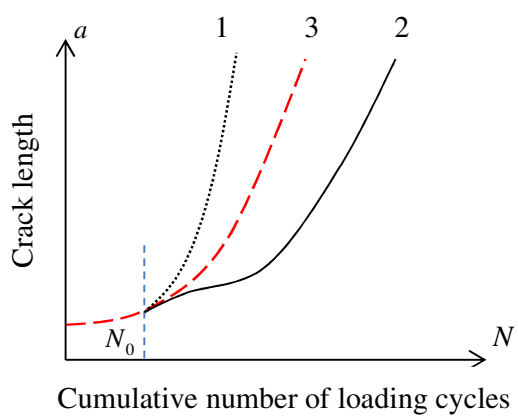

Figure 2.1: Crack length – cumulative number of loading cycles curves

The overload retardation effect has been widely observed in the real world for various materials, including structural steels, aluminum alloys, and titanium alloys [40-42], under various combinations of loading parameters, product geometries, and environmental conditions [43, 44]. As overload retardation significantly affects crack propagation, ignoring this effect can result in a biased estimation of product life in the life design stage [45]. In many situations

of product life design, overloads are added to regular fatigue loads during fatigue tests to accelerate the life testing procedure. If the added overloads are expected to accelerate the crack propagation, the designed product life is set longer than the product life obtained in the testing stage. However, if the tested material has an overload retardation effect, the added overloads actually decelerate rather than accelerate the crack propagation; thus, the real product life should be shorter than the tested life. As a result, the original design ignoring overload retardation leads to an overestimation of product life in the design stage. This is one of the causes of the Comet airplane crash [46].

In the literature, most of the research on overload retardation focuses on studying the physical explanation and its mechanical properties. Lankford and Davidson [18] proposed a theory of mechanics to explain the overload retardation effect by attributing the effect to a formation of a special plasticity area at the crack tip when an overload occurs, and they claimed that this plasticity area retarded crack propagation. Based on the aforementioned theory, mechanical properties of overload retardation, such as the crack tip blunting, strain hardening, crack closure and compressive residual stresses ahead of crack tip, have been widely studied in the literature [19]. Although these studies discussed retardation effect, they did not model it quantitatively. Moreover, based on the mechanical theories and studies of overload retardation, some simulation models have also been developed to study the time of fatigue failure considering overloads. Dominguez *et al*. [20] developed a simulation model to estimate the failure time when random overloads were added in fatigue loads. Although their simulated failure times are close to those obtained in physical experiments, the analysis is based on time-to-failure data rather than degradation paths that can capture more precise failure information.

Another simulation model was developed by Kim and Shim [47] to describe the crack propagation subjected to a single overload. However, the research does not provide a systematic method to estimate model parameters considering random errors. In addition, the study is based on a restricted assumption that the occurring time of the overload is fixed and predetermined though the assumption may not be feasible in real world applications.

In the area of statistical reliability engineering, reliability studies are primarily based on analyses of time-to-failure data [8, 9] or degradation path data [48] obtained in normal or accelerated life tests [49, 50], through parametric, nonparametric modeling methods [51] or Monte Carlo simulation method [52], aiming at time-to-failure estimation, remaining life prediction, etc. [53, 54]. Besides system lifetime analysis, some other applications of reliability studies include maintenance optimization [5] and fault diagnosis [55, 56]. For our problem, conventional reliability methods based on analyses of degradation paths [48, 57] cannot be directly applied to analyzing crack propagation paths when the material has an overload retardation effect. Although crack propagation paths in the time domain can be directly described by applying curve fitting methods (e.g., polynomial approximation, B-spline), such direct application may violate the physical mechanism of overload retardation. For example, before an overload arrives, the physical domain curve should be a straight line. Nonetheless, in the time domain, the directly fitted curve is inevitably contaminated with random errors, and the contaminated time domain curve uniquely determines a physical domain curve which could not be a straight line, therefore violating the Paris law. Furthermore, the multiple samples of crack propagation paths with overloads being applied at different time points cannot be assumed coming from the same degradation population, which is usually the presumption of

existing degradation models.

In this chapter, we propose a physical – statistical model to quantitatively model the overload retardation as well as the overload acceleration effect. A maximum likelihood estimation method is developed to estimate the model parameters. Given an observed crack propagation path, a likelihood ratio test is developed to determine whether the tested material has an overload retardation or overload acceleration effect. The proposed model is further applied to reliability estimation of crack failures.

The layout of this chapter is as follows: Section 2.3 presents the proposed physical-statistical model; Section 2.4 develops the maximum likelihood estimation for model parameters; Section 2.5 develops the likelihood ratio test to determine whether a material has an overload retardation or acceleration effect; Section 2.6 applies the developed physical – statistical model to reliability estimation; Section 2.7 verifies the proposed model by using a designed physical experiment, along with a simulation study; and Section 2.8 concludes the chapter and discusses future work.

2.3 Physical – Statistical Model

A physical – statistical model is proposed for overload retardation in crack propagation in which both physical mechanisms and random errors are considered. With minor changes this model can also describe overload acceleration. In this research, we focus on modeling the effect of a single overload that is added into regular fatigue loads.

In the proposed physical – statistical model, the crack propagation paths are characterized in two domains. The first domain is the crack growth rate – range of stress intensity factor ($da/dN - \Delta K$) domain (later called physical domain in this chapter), and the domain is most

popularly employed in mechanical property analysis of crack propagations as it reveals the physical inner rules [58]. For example, the conventional Paris law depicted by (1) is established in this domain. Specifically, ΔK in (1) is a physical descriptor that characterizes the stress intensity fluctuation at a crack tip; the stress intensity fluctuation in nature causes a crack to open and close, and in turn drives the crack propagation. Figure 2.2 (a) below illustrates a crack propagation process in the physical domain, where x denotes $\log(\Delta K)$, y denotes $\log(da/dN)$, and line *DE* represents a crack propagation process following the Paris law. The path *D-A-B-C-E* in Figure 2.2 (a) illustrates a crack propagation with overload retardation when an overload occurs at point *A*; after point *A* the crack growth rate plummets and then returns back to the Paris law that is represented by line *DE*. The second domain is the observed crack length – cumulative loading cycles ($a_o - N$) domain (later called time domain in this chapter), where a_o is the observed crack length. The time domain is mostly adopted in statistical models to describe degradation paths. The solid curve in Figure 2.2 (b) illustrates the crack propagation process with the same overload retardation effect as illustrated in Figure 2.2 (a), where the overload is applied at cycle N_0, and the observed data is denoted by symbol "x".

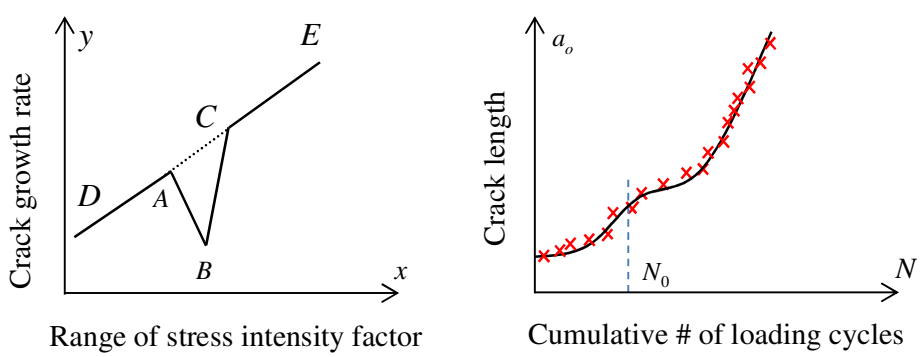

(a) Physical domain (b) Time domain

Figure 2.2: Crack growth modeling in physical and time domains

To quantitatively model overload retardation, we use piecewise linear segments *DA-AB-*

BC-CE as illustrated in Figure 2.2 (a) to delineate the logarithm of crack growth rate in the physical domain. The random errors are further captured and modeled in the time domain. The piecewise linear assumption in the physical domain is consistent with research results in the literature [59], as well as the crack propagation paths observed in our experiments. Under this assumption, the physical domain modeling is given as follows.

$$g_0(x)=\begin{cases} k_1x+b_1; x\in(-\infty,x_A]\cup(x_C,+\infty) \\ k_2x+b_2; x\in(x_A,x_B] \\ k_3x+b_3; x\in(x_B,x_C] \end{cases} \tag{2}$$

where k_i, b_i (i =1,2,3) are the slopes and intercepts of segment *DE*, *AB*, and *BC*, respectively, and $x_j=\log(\Delta K_j)$ is the abscissa of point j ($j=A,B,C$).

Considering the overload retardation behavior, Equation (2) is subject to two constraints: $\Delta k_{2,1}<0$ and $\Delta k_{3,1}>0$, where $\Delta k_{2,1}=k_2-k_1$ and $\Delta k_{3,1}=k_3-k_1$ as illustrated by the crack path *D-A-B-C-E* in Figure 2.2. Specifically, the first constraint $\Delta k_{2,1}<0$ is used to depict the decrement of crack growth rate compared to the straight line *DE* following the Paris law, and the second constraint $\Delta k_{3,1}>0$ is to ensure that the crack growth rate is able to return back to the Paris law after some time.

Although model (2) is straightforward in describing the overload retardation in the physical domain, not all the parameters in (2) have physical interpretations. A physically interpretable parameter set $\boldsymbol{\theta}_1=\{k_1,\Delta k_{2,1},\ \Delta k_{3,1},b_1,l,d\}$ is thus introduced. Specifically, the parameters b_2 and b_3 in (2) are replaced by the following equations.

$$\begin{cases} b_2=-\Delta k_{2,1}\times l+b_1 \\ b_3=-\Delta k_{3,1}\times l+b_1+\dfrac{\Delta k_{3,1}-\Delta k_{2,1}}{k_1+\Delta k_{2,1}}\times d \end{cases} \tag{3}$$

In $\boldsymbol{\theta}_1$, the slope k_1 determines the varying rate of crack growth speed before an overload;

$\Delta k_{2,1}$ and $\Delta k_{3,1}$ capture the varying rate changes caused by the overload compared to k_1; b_1 corresponds to the material constant c in the Paris law with relationship $b_1 = \log(c)$; and l and d, respectively, denotes the occurring time of the overload in the physical domain and the maximum decreasing amount of crack growth rate which captures the degree of overload retardation, as shown in Figure 2.3.

In the time domain, let $a_o(N)$ denote the observed crack length at cycle N and let $a(N)$ denote the crack propagation associated with the piecewise model in the physical domain represented by Equation (2). The relationship of $a_o(N)$ and $a(N)$ is modeled as follows.

$$a_o(N) = a(N) + \varepsilon(N) \tag{4}$$

where $\varepsilon(N)$ is the random error at cycle N, which is assumed to be independently, identically, and normally distributed with mean zero and variance σ^2.

With minor changes, the developed physical - statistical model can be used to describe the overload acceleration effect by changing the constraints of (2) to $\Delta k_{2,1} > 0$ and $\Delta k_{3,1} < 0$. The corresponding path of the crack growth rate of overload acceleration in the physical domain is illustrated by path *D-A-B*-C-E* in Figure 2.3.

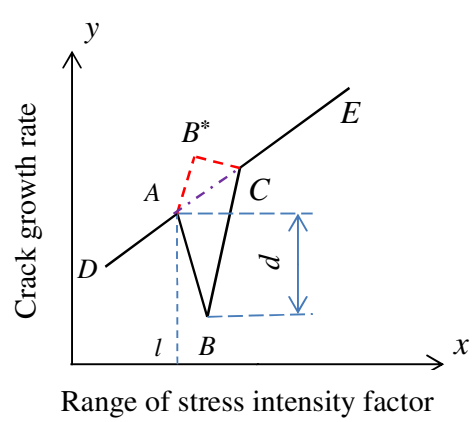

Figure 2.3: Crack growth rate vs. range of stress intensity factor (log-scale) in physical domain

2.4 Model Parameter Estimation

The parameters in the proposed physical – statistical model include $\boldsymbol{\theta}_1$ for the physical domain modeling and σ for the time domain modeling, i.e., $\boldsymbol{\theta} = \{\boldsymbol{\theta}_1, \sigma\}$. We develop a Maximum Likelihood Estimation (MLE) method to estimate $\boldsymbol{\theta}$ given an observed crack propagation curve in the time domain. In Section 2.4.1, the likelihood function is derived. The likelihood function is piecewise with unknown breakpoints, and thus makes the MLE difficult to implement. To overcome this difficulty, we propose an approximation of the physical Equation (2) in Section 2.4.2. The approximation makes the likelihood function a single piece of function that is continuously differentiable with respect to $\boldsymbol{\theta}$. Next, $\boldsymbol{\theta}$ is estimated along with its corresponding standard errors in Section 2.4.3.

2.4.1 Likelihood Function

Before deriving the likelihood function, the model constraints are eliminated by a variable transformation technique. Considering the overload retardation case, we introduce two parameters $\Delta k_{2,1}^*$ and $\Delta k_{3,1}^*$ to replace $\Delta k_{2,1}$ and $\Delta k_{3,1}$ by using two equations $\Delta k_{2,1} = -\exp\left(\Delta k_{2,1}^*\right)$ and $\Delta k_{3,1} = \exp\left(\Delta k_{3,1}^*\right)$ so that the two constraints $\Delta k_{2,1} < 0$ and $\Delta k_{3,1} > 0$ are eliminated. The transformed model parameters are denoted by $\boldsymbol{\theta}^* = \left\{k_1, \Delta k_{2,1}^*, \Delta k_{3,1}^*, b_1, l, d, \sigma\right\}$.

With respect to $\boldsymbol{\theta}^*$, the likelihood function is derived based on the observed crack propagation path, denoted by $\mathbf{X} = \left\{\left(N_k, a_o\left(N_k\right)\right), k = 1, 2, ..., n\right\}$, where N_k and $a_o(N_k)$ are the kth cumulative number of loading cycles and the corresponding observed crack length at cycle N_k; n is the total number of observations. Based on (4), the likelihood function is constructed as follows.

$$L\left(\boldsymbol{\theta}^{*} \mid \mathbf{X}\right)=\prod_{k=1}^{n} \frac{1}{\sigma\sqrt{2\pi}} e^{-\frac{\left[a_{o}(N_{k})-a(N_{k})\right]^{2}}{2\sigma^{2}}} \tag{5}$$

where $a(N_k)$ is the model crack length at cycle N_k.

In particular, $a(N_k)$ is calculated by solving Equation (2), noticing that in (2) x denotes $\log(\Delta K)$, and $g_0(x)$ denotes $\log(da/dN)$ at location x. The item ΔK is determined by the real time crack length, loading parameters, and specimen geometry. For specimens that have regular shapes such as cuboids, ΔK can be calculated with explicit approximate equations. However, when specimens have complicated shapes, direct calculation of ΔK is arduous. In this case, mechanical models of the specimens, based on which finite element methods can be applied to calculate ΔK [60], need to be established.

2.4.2 Model Approximation in the Physical Domain

In the likelihood function (5), $a(N_k)$ is piecewise because $g_0(x)$ in (2) is piecewise. As a result, the likelihood function will also be piecewise with unknown breakpoints. This makes the implementation of MLE difficult. To overcome this challenge, we approximate $g_0(x)$ with a single piece of function that is continuously differentiable with respect to $\boldsymbol{\theta}$. Furthermore, we will show that the proposed approximate function converges to $g_0(x)$ as the approximation parameters go to infinity.

To approximate the function $g_0(x)$ in (2), we start by rewriting it as the following function $g_1(x)$.

$$g_1(x)=\min\left\{\max\left\{k_2x+b_2, k_3x+b_3\right\}, k_1x+b_1\right\},\ x\in\mathbb{R} \tag{6}$$

where $\max\{m,n\}=\begin{cases} m, & \text{if } m\geq n \\ n, & else \end{cases}$ and $\min\{m,n\}=\begin{cases} n, & \text{if } m\geq n \\ m, & else \end{cases}$.

As shown in Figure 2.4 (left), the term $\max\{k_2x+b_2, k_3x+b_3\}$ in $g_1(x)$ corresponds to the

two half lines *BA* and *BC*, and $g_1(x)$ describes the path *D-A-B-C-E* for $x \in \mathbb{R}$. Thus, $g_1(x)$ is equivalent to $g_0(x)$.

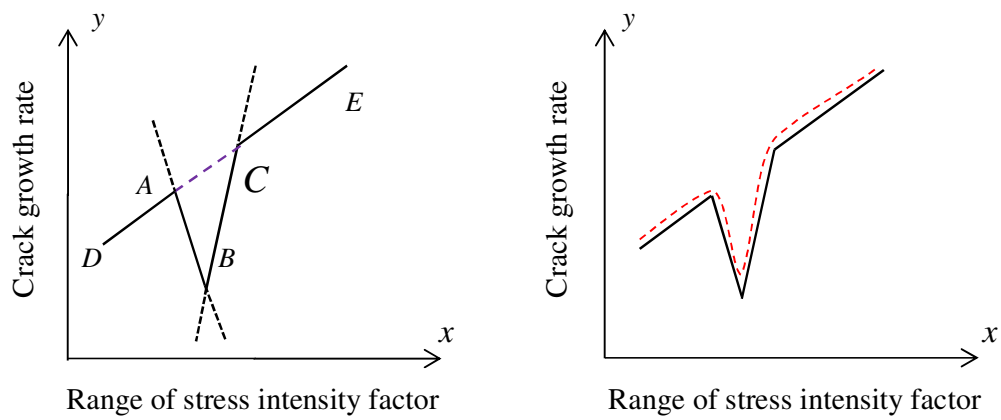

Figure 2.4: Illustration of physical domain modeling (left) and its approximation (right)

Next, we approximate $g_1(x)$ by a single function that is continuously differentiable. In the literature, Hardy *et al*. [61] developed a method to approximate $\max\{m_1, m_2\}$, where m_1 and m_2 are two given positive numbers. In this research, we extend Hardy's method to approximate the function $g_1(x)$ that contains mixed operators of max and min acting on three functions. The following Proposition 1 is derived to approximate $g_1(x)$. The detailed proof of Proposition 1 is listed in Appendix 1.

Proposition 1. The following function $g_2(x;p,q)$ satisfies $\lim_{p,q\to+\infty} g_2(x;p,q) = g_1(x)$, and thus approximates $g_1(x)$ when *p* and *q* are selected as finite values.

$$g_2(x;p,q) = -\omega(x)\left\{\left(\frac{B(x)-U(x)}{\omega(x)}\right)^p + \left(\frac{B(x)-(k_1x+b_1)}{\omega(x)}\right)^p\right\}^{\frac{1}{p}} + B(x) \tag{7}$$

where $x \in \mathbb{R}$; $U(x) = \delta(x)\left\{\sum_{i=2}^{3}\left(\frac{M(x)+k_ix+b_i}{\delta(x)}\right)^q\right\}^{\frac{1}{q}} - M(x)$; $M(x)$ and $B(x)$ are positive functions selected to keep functions $M(x)+k_ix+b_i$ $(i=2,3)$ and $B(x)-(k_ix+b_i)$

$(i=1,2,3)$ positive. In this research, we select $M(x)=B(x)=\sum_{i=1}^{3}|k_i x+b_i|+1$. In addition, $\delta(x)$ and $\omega(x)$ are chosen to avoid the overload flow problem when large values of p and q are selected. Specifically, $\delta(x)=\sum_{i=2}^{3}|k_i x+b_i|+|M(x)|$ is to ensure $0\le\frac{M(x)+k_i x+b_i}{\delta(x)}\le 1$ for $i=2,3$; and $\omega(x)=|B(x)|+\sum_{i=1}^{3}|k_i x+b_i|+1$ is to ensure $0\le\frac{B(x)-\max\{k_2x+b_2,k_3x+b_3\}}{\omega(x)}\le 1$ and $0\le\frac{B(x)-(k_1x+b_1)}{\omega(x)}\le 1$.

In Proposition 1, the function $g_2(x;p,q)$ is continuously differentiable with respect to both the dependent variable x and model parameters. When p and q go to infinity, $g_2(x;p,q)$ converges to $g_1(x)$. Thus, $g_2(x;p,q)$ can approximate $g_1(x)$ when finite values of p and q are selected. To assess the accuracy of approximation, the error bounds are derived in Proposition 2. The detailed proof of Proposition 2 is listed in Appendix 2.

Proposition 2. The approximation error $\xi(x)$ in Proposition 1, defined as $\xi(x)=g_2(x;p,q)-g_1(x)$, is bounded as follows.

$$-\frac{c_2(x)}{q}\le\xi(x)\le\frac{c_1(x)}{p}-\frac{c_2(x)}{q} \tag{8}$$

where for any fixed $x\in\mathbb{R}$, $c_1(x)$ and $c_2(x)$ are constants defined as $c_1(x)=2\log 2\times\left(M^*(x)+\max\{k_2x+b_2,k_3x+b_3\}\right)$ and $c_2(x)=2\log 2\times\left(B^*(x)+\max\{-\max\{k_2x+b_2,k_3x+b_3\},-k_1x-b_1\}\right)$.

Based on (8), as p and q increase, the approximation errors can be uniformly small. The error bounds also provide a guideline for selecting p and q. As illustrated in Figure 2.4 (right), the dash curve is the approximate crack propagation path in the physical domain.

The approximation of Equation (2) for the overload acceleration effect is similar to that

for the overload retardation effect. To handle this approximation, the following $\bar{g}_1(x)$ needs to be applied to replace $g_1(x)$ in (6).

$$\bar{g}_1(x) = \max\{\min\{k_2x+b_2, k_3x+b_3\}, k_1x+b_1\},\ x \in \mathbb{R} \tag{9}$$

Similar to function $g_2(x;p,q)$ in (7), the following function $\bar{g}_2(x;p,q)$ approximates $\bar{g}_1(x)$.

$$\bar{g}_2(x;p,q) = \omega(x)\left\{\left(\frac{B(x)+U^*(x)}{\omega(x)}\right)^p + \left(\frac{B(x)+(k_1x+b_1)}{\omega(x)}\right)^p\right\}^{\frac{1}{p}} - B(x) \tag{10}$$

where $x \in \mathbb{R}$; $U^*(x) = -\delta(x)\left\{\sum_{i=2}^{3}\left(\frac{M(x)-(k_ix+b_i)}{\delta(x)}\right)^q\right\}^{\frac{1}{q}} + M(x)$; and $\delta(x)$, $M(x)$, $B(x)$ and $\omega(x)$ are defined in (7). For the overload stationary case, the conventional Paris law equation is a single piece of continuously differentiable function that does not need to be further approximated.

2.4.3 Estimation of θ and Its Standard Errors

By maximizing the likelihood function $L(\boldsymbol{\theta}^* \mid \mathbf{X})$ in (5) with the model crack length $a(N_k)$ being calculated by numerically solving the approximate Equation (7), the parameters $\boldsymbol{\theta}^*$ are estimated as follows.

$$\widehat{\boldsymbol{\theta}^*} = \arg\max_{\boldsymbol{\theta}^*} L(\boldsymbol{\theta}^* \mid \mathbf{X}) \tag{11}$$

Based on the maximum likelihood estimation theory, $\widehat{\boldsymbol{\theta}^*}$ is asymptotically normal under the large sample assumption [62]. Hence, the asymptotic covariance matrix $\widehat{\boldsymbol{\Sigma}}_{\widehat{\boldsymbol{\theta}^*}}$ for $\widehat{\boldsymbol{\theta}^*}$ can be calculated from the observed Fisher information matrix $\mathbf{I}(\widehat{\boldsymbol{\theta}^*})$. Specifically, $\widehat{\boldsymbol{\Sigma}}_{\widehat{\boldsymbol{\theta}^*}} = \mathbf{I}^{-1}(\widehat{\boldsymbol{\theta}^*})$ and the observed Fisher information matrix can be calculated as

$$\mathbf{I}\left(\widehat{\boldsymbol{\theta}}^{*}\right)=-\left.\frac{\partial^{2}\log\left(L\left(\boldsymbol{\theta}^{*}\mid\mathbf{X}\right)\right)}{\partial\boldsymbol{\theta}^{*}\partial\boldsymbol{\theta}^{*T}}\right|_{\boldsymbol{\theta}^{*}=\widehat{\boldsymbol{\theta}}^{*}}\quad[62].$$

The estimate of model parameters $\boldsymbol{\theta}$, denoted by $\hat{\boldsymbol{\theta}}$, can be computed based on $\widehat{\boldsymbol{\theta}}^{*}$ obtained in (11). Specifically, the estimates of $\widehat{\Delta k_{2,1}}$ and $\widehat{\Delta k_{3,1}}$ in $\hat{\boldsymbol{\theta}}$ are computed as $\widehat{\Delta k_{2,1}}=-\exp\left(\widehat{\Delta k_{2,1}^{*}}\right)$ and $\widehat{\Delta k_{3,1}}=\exp\left(\widehat{\Delta k_{3,1}^{*}}\right)$, where $\widehat{\Delta k_{2,1}^{*}}$ and $\widehat{\Delta k_{3,1}^{*}}$ are given in $\widehat{\boldsymbol{\theta}}^{*}$. The asymptotic covariance matrix $\widehat{\boldsymbol{\Sigma}}_{\hat{\boldsymbol{\theta}}}$ for $\hat{\boldsymbol{\theta}}$ can be calculated by applying the delta method [63] as follows.

$$\widehat{\boldsymbol{\Sigma}}_{\hat{\boldsymbol{\theta}}}=\left.\left(\frac{\partial\boldsymbol{\theta}}{\partial\boldsymbol{\theta}^{*}}\right)^{T}\widehat{\boldsymbol{\Sigma}}_{\widehat{\boldsymbol{\theta}}^{*}}\left(\frac{\partial\boldsymbol{\theta}}{\partial\boldsymbol{\theta}^{*}}\right)\right|_{\boldsymbol{\theta}^{*}=\hat{\boldsymbol{\theta}}}\tag{12}$$

The estimates of the standard errors of $\boldsymbol{\theta}$ are square roots of the diagonal elements in $\widehat{\boldsymbol{\Sigma}}_{\hat{\boldsymbol{\theta}}}$.

It needs to be noted that the likelihood function (5) is calculated based on a single crack propagation path. The developed MLE method can be easily extended to handle multiple crack propagation paths. An example of such an extension to handle multiple crack propagation paths with different occurring times of overloads is given in Section 2.6.

2.5 Testing of Material Overload Property Subject to an Overload

Materials can have overload retardation, overload stationary, or overload acceleration effects. Given an observed crack propagation curve of a tested material that is subject to an overload, it is important to determine whether the overload retardation/acceleration takes effect. Thus, we develop the following likelihood ratio hypothesis test.

H_0, the tested material does not have an overload retardation nor overload acceleration effect vs. H_1, the tested material has either an overload retardation or overload acceleration effect.

(13)

Based on the aforementioned hypothesis, the test statistic D is developed as:

$$D = -2\log\frac{\sup\left\{L\left(\boldsymbol{\theta}\middle|\mathbf{X},H_0\right)\right\}}{\sup\left\{L\left(\boldsymbol{\theta}\middle|\mathbf{X},H_0\cup H_1\right)\right\}} \tag{14}$$

where " sup " is the supremum operator; $L\left(\boldsymbol{\theta}\middle|\mathbf{X},H_0\right)$ and $L\left(\boldsymbol{\theta}\middle|\mathbf{X},H_0\cup H_1\right)$ are the likelihood functions under the null hypothesis and the full model, respectively. Specifically, $\sup\left\{L\left(\boldsymbol{\theta}\middle|\mathbf{X},H_0\right)\right\}=L_2$ and $\sup\left\{L\left(\boldsymbol{\theta}\middle|\mathbf{X},H_0\cup H_1\right)\right\}=\sup\left\{L_1,L_2,L_3\right\}$, where L_1, L_2 and L_3 are the maximum likelihood values for the overload retardation model, the overload stationary model, and the overload acceleration model, respectively. In particular, L_1, L_2 and L_3 are computed with the model crack length $a\left(N_k\right)$ being calculated following the approximate function $g_2\left(x;p,q\right)$ in (7), the conventional Paris law equation, and the approximate function $\overline{g}_2\left(x;p,q\right)$ in (10), respectively.

The test statistic D, under the large sample assumption, can be approximated by a chi-square distribution with degrees of freedom df_2-df_1, where df_1 and df_2 are the number of free parameters in the null hypothesis and the full model, respectively. The null hypothesis H_0 is rejected if $D>\chi^2_{df_2-df_1}(\alpha)$, where α is the specified test significance level and $\chi^2_{df_2-df_1}(\alpha)$ is the upper α quantile of the chi-square distribution with degrees of freedom df_2-df_1. In our problem, $df_1=3$ and $df_2=7$.

2.6 Application to Reliability Estimation

Overload retardation can remarkably influence product reliability. However, little of the existing reliability estimation research takes the overload retardation effect into consideration. In this research, we develop a reliability estimation method that considers such effect as an application of the proposed physical – statistical model.

For consistence with the research in literature, the crack failure is defined to occur when the crack length reaches a pre-specified threshold limit a_c, and the failure time T is the first

crossing time calculated as follows.

$$T = \min\left\{N : a(N) \geq a_c\right\} \tag{15}$$

In this research, we focus on the case of a single overload added to the regular fatigue loads for each sample unit, while the occurring times of overloads for different sample units are different and can be treated as being randomly distributed. The exponential distribution is chosen as the distribution of overload occurring times although other types of distributions can be applied in a similar way.

The developed reliability estimation method consists of two stages. In Stage 1, by applying the proposed physical – statistical model, the model parameters that characterize material overload retardation properties can be estimated given a set of observed crack propagation paths, obtained either from historical data or through designed experiments. The model parameters are estimated using the developed parameter estimation method in Section 2.4. Whether the tested material has an overload retardation or overload acceleration effect can be further tested using the methods developed in Section 2.5. In Stage 2, the estimated model parameters are further used to estimate the Cumulative Distribution Function (CDF) of failure times of the product units, each subject to a single overload at a different occurring time. Denote the CDF of time-to-failure as $F(t;\boldsymbol{\theta}) = \Pr(T < t),\ t \geq 0$. The analytical form of $F(t;\boldsymbol{\theta})$ is difficult to obtain due to the complexity of the physical – statistical model. Hence, we calculate the empirical CDF through a simulation method as listed in the following Algorithm 2.1.

Algorithm 2.1: The calculation of CDF of time-to-failure.

1. Denote the m observed crack propagation paths with different overload occurring

times by $\mathbf{X}_1,...,\mathbf{X}_m$. Assume that $\mathbf{X}_1,...,\mathbf{X}_m$ share the same model parameters $\boldsymbol{\theta}_p = \{k_1, \Delta k_{2,1}, \Delta k_{3,1}, b_1, d, \sigma\}$, and the occurring time points of the overloads in the physical domain, denoted as $\boldsymbol{\theta}_l = \{l_1, l_2, ..., l_m\}$, are different. The model parameters $\boldsymbol{\theta}_M = \{\boldsymbol{\theta}_p, \boldsymbol{\theta}_l\}$ can be estimated by maximizing the likelihood function, i.e., $\widehat{\boldsymbol{\theta}_M} = \arg\max_{\boldsymbol{\theta}_M} L(\boldsymbol{\theta}_M \mid \mathbf{X}_1,...,\mathbf{X}_m)$, where $L(\boldsymbol{\theta}_M \mid \mathbf{X}_1,...,\mathbf{X}_m)$ is defined as

$$L(\boldsymbol{\theta}_M \mid \mathbf{X}_1,...,\mathbf{X}_m) = \prod_{i=1}^{m} L_i(\boldsymbol{\theta}_i \mid \mathbf{X}_i) \tag{16}$$

In (16), $\boldsymbol{\theta}_i = \{\boldsymbol{\theta}_p, l_i\}$; $L_i(\boldsymbol{\theta}_i \mid \mathbf{X}_i)$ is the likelihood function for the ith observed path and can be calculated by methods developed in Section 2.4.

2. Simulate an occurring time t_0 of the overload in the time domain from a specified random distribution. In this research, the exponential distribution is chosen.
3. Transform the overload occurring time t_0 in the time domain to the logarithm of the range of stress intensity factor in the physical domain, denoted as l_0, based on the conventional Paris law as overload retardation does not take effect before l_0.
4. Based on the estimated model parameters $\widehat{\boldsymbol{\theta}_p}$ and the overload occurring time l_0, obtain the complete physical domain curve and calculate the corresponding degradation path in the time domain by numerically solving Equation (2).
5. Based on the calculated degradation path, compute the failure time T using (15).
6. Repeat steps 2 to 5 for M_1 times to obtain the failure times T_i, $i = 1, 2, ..., M_1$, where M_1 is chosen large enough to provide sufficient precision. The empirical estimate of $F(t;\boldsymbol{\theta})$ can then be obtained as $F(t;\hat{\boldsymbol{\theta}}) = M_1^{-1} \sum_{i=1}^{M_1} I_{i,N}$, where $I_{i,N}$ equals 1 if $T_i \le t$ and 0 otherwise.

We also compute the 95% pointwise confidence intervals of the empirical CDF. Thus, for

any time t^*, the probability that the confidence interval at t^* covers the true value $F\left(t^*;\boldsymbol{\theta}\right)$ is 0.95. There are two major challenges for the interval estimation. First, the theoretical distribution of our model parameter estimators is unknown and difficult to derive. Second, under most situations the sample size of the crack propagation paths is insufficient for straightforward statistical inference as conducting experiments is generally expensive and time consuming. To overcome these challenges, we develop the following Algorithm 2.2 by applying a bootstrap method.

Algorithm 2.2: The bootstrap method for interval estimation of model parameters.

1. Generate M_2 iterations of bootstrap samples [64] from the sample that consists of m observed crack propagation paths.
2. For each bootstrap sample, calculate an empirical CDF of time-to-failure denoted as $F_j\left(t;\hat{\boldsymbol{\theta}}\right)$ for $j=1,2,...,M_2$, following Algorithm 2.1.
3. Based on the aforementioned M_2 CDFs, the 95% pointwise confidence intervals can be obtained as their 95% pointwise quantiles. Specifically, denote $\mathbf{F}\left(t;\hat{\boldsymbol{\theta}}\right)=\left(F_1\left(t;\hat{\boldsymbol{\theta}}\right),F_2\left(t;\hat{\boldsymbol{\theta}}\right),...,F_{M_2}\left(t;\hat{\boldsymbol{\theta}}\right)\right)^T$. The upper bound $F_{0.975}\left(t;\hat{\boldsymbol{\theta}}\right)$ and lower bound $F_{0.025}\left(t;\hat{\boldsymbol{\theta}}\right)$ are calculated as the 0.975 and 0.025 quantiles of $\mathbf{F}\left(t;\hat{\boldsymbol{\theta}}\right)$, respectively.

2.7 Case Study

We designed and conducted an experiment to verify and illustrate the proposed methods. In the experiment, crack propagation paths were obtained by testing specimens that are subjected to compact tension (CT) fatigue loads [65] mixed with a single overload. The testing machine is the Instron 8801 fatigue testing system as illustrated in Figure 2.5 (left). All the

tested specimens were made according to the American Society for Testing and Materials (ASTM) E399 standard as illustrated in Figure 2.5 (right). As the tested specimens have regular shapes, the range of stress intensity factor, i.e., ΔK in (7), was calculated by the following polynomial equation [65].

$$\Delta K = \frac{\Delta P(2+\zeta)}{H\sqrt{W}(1-\zeta)^{3/2}}(0.886+4.64\zeta-13.32\zeta^2+14.72\zeta^3-5.6\zeta^4) \qquad (17)$$

where ΔP is the amplitude of the applied cyclic loading; W is the specimen width; ζ is the real time ratio of the crack length and the specimen width (i.e., a/W); and H is the specimen thickness.

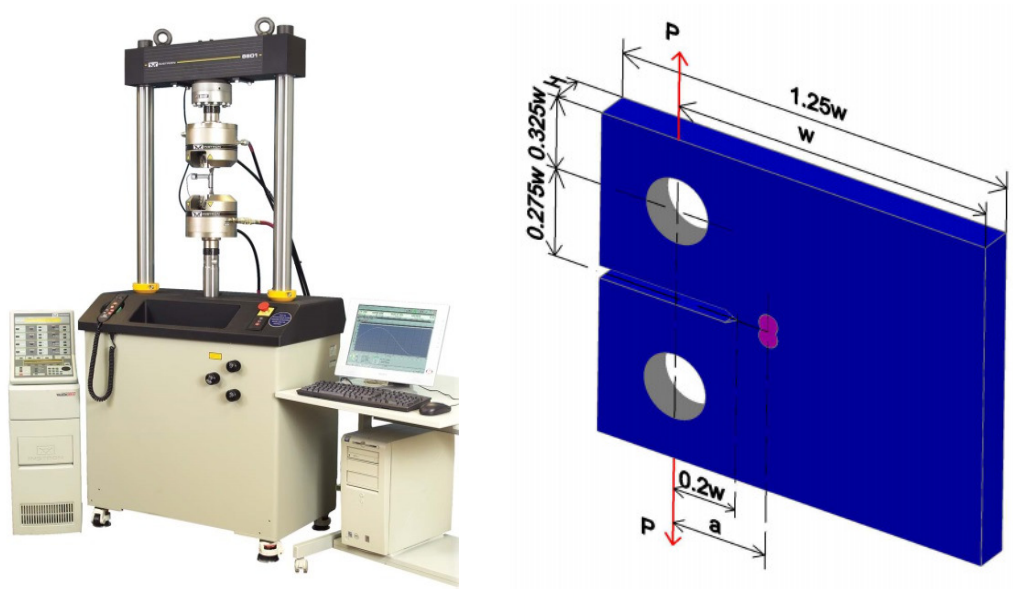

Figure 2.5: Instron 8801 testing system (left) and the compact tension specimen (right)

In the experiment, five specimens made of 304 stainless steel were tested. A video was recorded to monitor the crack propagation process for each tested specimen. By analyzing the recorded videos, five crack propagation paths were obtained.

2.7.1 Parameter Estimation

The model parameters were estimated based on the five observed crack propagation paths

by maximizing the likelihood function (11). The standard errors of the estimated parameters were computed following (12). Table 2.1 below lists the estimated model parameters and the corresponding standard errors.

Table 2.1: Estimated model parameters and standard errors in case study

Parameters	k_1	$\Delta k_{2,1}$	$\Delta k_{3,1}$	b_1	d	σ
Estimated value	1.921	-20.982	8.539	-15.085	1.013	0.028
Standard error	0.0016	2.043	0.431	0.007	0.023	0.004
Parameters	l_1	l_2	l_3	l_4	l_5	-
Estimated value	3.496	3.391	3.462	3.447	3.516	-
Standard error	0.003	0.004	0.002	0.003	0.003	-

The crack propagation process in the time domain can be calculated by substituting the estimated parameters $\hat{\boldsymbol{\theta}}_M$ into (2) and then numerically solving (2). We randomly selected a calculated model crack propagation path presented by the solid curve in Figure 2.6 to compare with the corresponding experimental path. From Figure 2.6, it can be seen that the crack propagation curve fits the experimental path well.

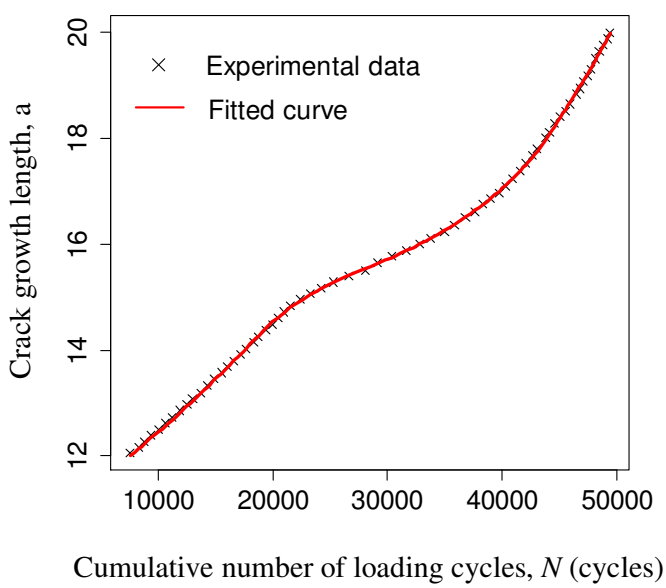

Figure 2.6: The observed crack propagation path vs. the model crack propagation path

2.7.2 Overload Property Testing

We applied the developed likelihood ratio test to determine whether the overload retardation/acceleration takes effect for the tested material. The test static D was calculated as 407.28 by using (14). As D follows a chi-square distribution with degrees of freedom equaling 4, the corresponding p-value is calculated and satisfies $p \ll 0.01$. Thus, the null hypothesis H_0 is rejected at a selected test significance level $\alpha = 0.05$. As a result, we conclude that for the 304 stainless steel, the crack propagation does not follow the conventional Paris law. Moreover, considering that $\widehat{\Delta k_{2,1}} = -20.98 < 0$, the steel has an overload retardation effect. The test result is summarized in Table 2.2.

Table 2.2: Result of overload retardation property testing

Parameter	D	$\Delta k_{3,1}$	*p value*
Estimated value	407.28	-20.98	<< 0.01
Conclusion	H_0 is rejected: there is an overload retardation effect		

2.7.3 Reliability Estimation

To apply the developed reliability estimation approach, the threshold limit of crack failure was specified as $a_c = 18$ mm. We assumed that the occurring time of an overload follows an exponential distribution with probability density function $f_T(t) = \lambda e^{-\lambda t}, (t > 0)$, where λ is a distribution parameter and indicates the arrival rate of the overload. Based on the five experimentally collected crack propagation paths, Algorithm 2.1 was implemented to estimate the time-to-failure CDF, and Algorithm 2.2 was applied to estimate the 95% pointwise confidence intervals (PCIs) of the CDF.

Two overload arrival rates were selected, i.e., $\lambda_1 = 0.5 \times 10^{-4}$ and $\lambda_2 = 2 \times 10^{-4}$. For each

arrival rate, the number of iterations for Algorithm 2.1 was set as $M_1 = 10000$ and the number of bootstrap iterations for Algorithm 2.2 was set as $M_2 = 10000$. The simulation results are illustrated in Figure 2.7, in which the solid curves illustrate the estimated time-to-failure CDF, and the dash curves illustrate the 95% PCIs.

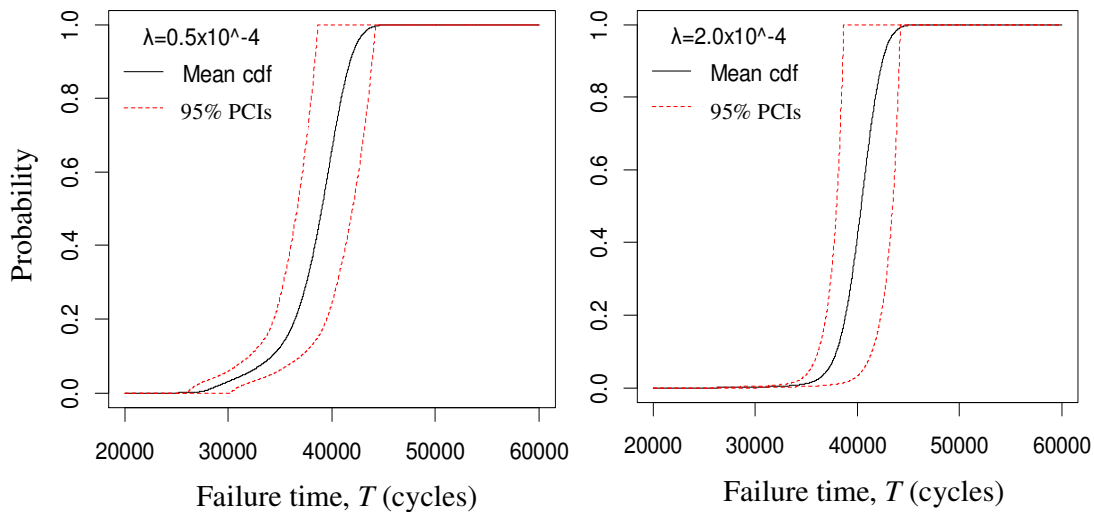

Figure 2.7: The estimated failure time CDF and the 95% pointwise confidence intervals

From Figure 2.7, it can be seen that the mean life corresponding to λ_1 is shorter than that corresponding to λ_2. This result can be explained as follows. For a smaller overload arrival rate λ_1, the corresponding specimen is expected to experience a longer time period (in which the crack growth rate increases following the conventional Paris law) before the overload occurs so that the crack growth rate can reach a higher value. When the overload occurs, it causes a formation of a special plasticity zone at the crack tip which retards the crack propagation process. A higher crack growth rate makes the crack propagation take less time to penetrate the special plasticity area, after which the overload retardation effect disappears. Hence, the expected lifetime due to the overload retardation effect is shorter and thus it results in a shorter mean life.

2.8 Summary

Overload retardation has a significant impact on crack propagation process and in turn affects reliability estimation of products with crack-caused failure modes. In this chapter, we propose a physical – statistical model to quantitatively model the overload retardation effect. In the physical domain, we build up a modified Paris law model to characterize the physical mechanism of overload retardation. In the time domain, we model the random errors. The developed physical – statistical model can also describe the overload acceleration and the overload stationary effects with minor changes. Based on the proposed model, a maximum likelihood method is developed to estimate the model parameters. In addition, a likelihood ratio test is developed to determine whether a tested material has an overload retardation or overload acceleration effect. As an application example, the proposed model is applied to reliability estimation of products with a single overload arriving in a random time point. The developed methods are illustrated and verified through designed experiments.

In this chapter, we focus on modeling the material retardation effect of a single overload. The proposed model can serve as a foundation for future research to model the complex interaction effects of multiple overloads. Moreover, in this chapter we set the overload ratio (the amplitude ratio of the overload to the cyclic loading) as a constant. In the future, it will be interesting to study how the overload retardation/acceleration effect changes over different overload ratios. More research will be conducted to study the overload effect for different types of materials under various experimental conditions. In addition, the proposed model can be further enhanced by considering sample to sample variations, which is another interesting future research topic.

The methodologies proposed in this chapter has been published in journal article [66].

CHAPTER 3. RELIABILITY ANALYSIS BY CONSIDERING STEEL LOCAL-SCALE DYNAMIC DEFORMATION

3.1 Overview

Material deformation is one of the major causes of material failures. In a dynamic deformation process, local deformation, defined as the displacement of various local points on a material, essentially determines the failure. Most existing studies on material reliability are conducted based on either the failure time or the degradation data. They do not consider the dynamic local deformation of materials and often are not efficient to model the failure mechanism. In this chapter, we develop reliability analysis by utilizing information contained in the dynamic local deformation of advanced high strength steel in a tensile process. Specifically, a new multivariate general path model is proposed to describe the deformation process. A two-stage method is developed to estimate the model parameters and overcome the computational complexity. Based on the proposed model, reliability analyses are conducted for various cases of material deformation paths. A simulation study is implemented to verify and validate the developed methods. Physical experiments using advanced high strength steel are designed and conducted to demonstrate the proposed model.

3.2 Introduction

Most material failures, such as crack failure, fatigue failure and fracture failure, are originally caused by material deformation which often is a dynamic process, e.g., see Song and Sih [67], Mughrabi, *et al.* [68] and Clayton [69]. During the deformation process, the local points on the material often dynamically move to new locations. For example, consider a plate subject to horizontal tension as illustrated in Figure 3.1, in which the arrows indicate the direction of loading force. From time T_1 through T_2 to T_3, the plate is elongated until a crack

failure occurs, and three local points A, B, and C, respectively, move through locations A', B' and C' to locations A'', B'' and C''. The deformation (e.g., the displacement) of these local points is referred to as local deformation in this chapter. In contrast, we also define another term, global deformation, for later use as the overall material deformation such as the overall elongation of the plate, which is a resultant and average effect of the local deformation.

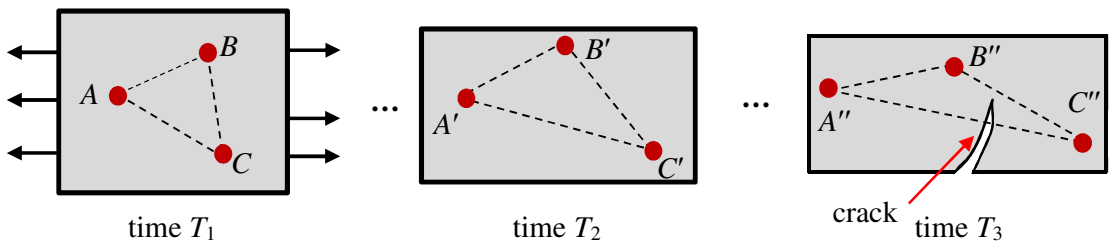

Figure 3.1: Plate deformation over time

Local deformation can reveal the failure mechanism/characteristic of a material. For example, consider the plate in Figure 3.1. As points A, B, and C have experienced different magnitudes of force, their absolute local deformation levels (e.g., absolute displacements) are different. An important failure characteristic of the plate is that the relative deformation of the local points, rather than the absolute deformation, is the determinant of the crack failure. It can be seen that when the relative displacement between points A and C reaches some threshold level, a crack forms between these two points. In contrast, if the absolute deformations of points A and C are large while their relative deformation is zero (such as in a plate translation process), the plate would not fail. Such failure characteristic cannot be revealed by the global material deformation, while it can be captured if the local deformation is considered. As a result, it is necessary to incorporate the dynamic local deformation information into material reliability evaluation.

In the materials science literature, local material deformation has been widely studied with specific focuses on its physical behaviors, mechanical properties and experimental designs. For example, Hashimoto, *et al.* [21] studied the impact of impulsive pressure on the local deformation and buckling of cylindrical tubes. Kolednik and Unterweger [70] studied the effect of the ductility of metal matrix composites on material local deformation behavior and damage evolution. Kolednik [22] discussed experimental procedures to study local material deformation and fracture properties. However, these studies do not quantitatively model the local material deformation and failure; thus, they cannot be directly applied to material reliability analysis. Furthermore, some other researchers developed simulation-based methods to study the local deformation. For instance, Springmann and Kuna [23] developed numerical methods to simulate material ductile damage considering its local deformation. Müller, *et al.* [71] and Kim [72] developed finite element methods to simulate material local deformation behaviors. However, all the aforementioned studies focus on analyzing the local deformation and failure using deterministic models, while in most real situations the deformation behaviors are stochastic, and material failures also exhibit randomness and uncertainty. Therefore, the aforementioned studies are not efficient enough to be directly applied to material reliability analysis.

In the reliability engineering literature, material failures have been widely studied based on collected lifetime or degradation information. For the lifetime based models, researchers utilize the lifetime data collected in designed experiments or from real-world systems to study material/product failures. For example, Zhao and Elsayed [3] developed a lifetime prediction method utilizing lifetime data in accelerated life testing. Hong, *et al.* [2] developed a remaining

life prediction method using lifetime data that are left truncated and right censored. Hong and Meeker [6] utilized lifetime data along with dynamic covariate information for field-failure predictions. Yang, *et al.* [73] conducted reliability analysis using lifetime data collected from repairable systems. Recently, Si, *et al.* [74] developed failure predictions of advanced high strength steel by jointly using the lifetime and microstructure image data of the steel. For more lifetime based reliability analysis, one can refer to Si and Yang [10], Zhang and Yang [5], Si and Yang [12], and Si, *et al.* [75], etc. In terms of the degradation based reliability analysis, rather than using the final failure time data, researchers utilize the degradation level vs. the time data that often provide richer reliability information. For example, Lu and Meeker [7] estimated time-to-failure distributions using a general path model to fit the degradation data. Pan and Balakrishnan [14] conducted reliability analysis using a gamma process to model the degradation data. Hong, *et al.* [76] predicted failures by utilizing degradation data with dynamic covariate information based on a linear random effects model. Xu, *et al.* [77] further developed a nonlinear random effects model for failure predictions by using degradation data with dynamic covariates. For more degradation based reliability analysis, see Kharoufeh and Cox [78], Lawless and Crowder [36], Si, *et al.* [66], Wang [79], etc. However, none of the existing studies incorporates the material local deformation into reliability analysis.

In this chapter, we conduct reliability analysis by utilizing dynamic material local deformation data in a tensile process. Specifically, we designed physical experiments using advanced high strength steel to monitor the complex spatio-temporal deformation processes of multiple material samples. For each sample, an image stream (consisting of around 1000 images) was obtained, recording the deformation level over time across a dense grid of points

on the plate surface. As a result, the data volume is large. Moreover, the image streams for every steel plate were collected with a high speed/rate in a real-time manner. In every second, around 30 high-resolution images of deformation were obtained and stored. Thus, the problem we study falls into the "big data" context. For some "big data" related reliability analyses, one can refer to Meeker and Hong [80]. In our experiment, one limitation of the current Digital Image Correlation (DIC) software is that it cannot automatically output the deformation levels at all the grid of points on the images. In this chapter, we manually collected the deformation paths corresponding to a set of selected points for each material sample from the image stream. Although limited deformation data is used in this chapter, the proposed multivariate general path model is general and can handle situations when more points are considered and when a higher image acquisition rate is used.

Figure 3.2 illustrates three typical deformation paths (1-3) that respectively correspond to local points A – C in Figure 3.1. To describe the collected multiple deformation paths, we propose a new multivariate general path model. The model generalizes the univariate general path model [7] that focuses on studying a single path. We further develop a two-stage method to estimate the model parameters. Moreover, as the relative deformation rather than the absolute deformation of the local points is the determinant of the material failure, the traditional failure criterion that assumes a failure occurs when the material degradation level (e.g., the absolute deformation level) reaches a specified threshold value cannot be directly used. To capture the failure mechanism/characteristic, a new variance-based failure criterion is applied. Next, by applying the new failure criterion, reliability analyses are developed for various types of deformation paths.

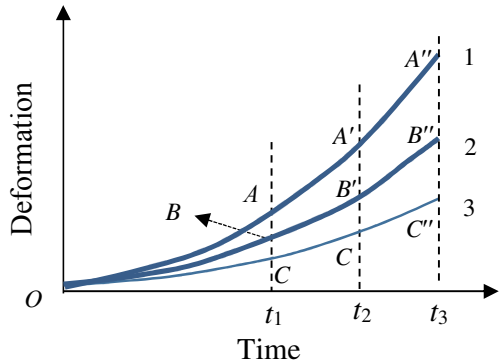

Figure 3.2: Deformation over time paths of one plate sample

The remainder of this chapter is organized as follows. In Section 3.3, the multivariate general path model and a two-stage model parameter estimation method are proposed. In Section 3.4, the variance-based failure criterion is presented. In Section 3.5, reliability analyses for different types of deformation paths are developed. In Section 3.6, a simulation study is implemented to verify the developed methods. In Section 3.7, physical experiments are conducted to demonstrate the proposed model. In Section 3.8, the chapter is concluded, and future work is discussed.

3.3 Statistical Model

In general, a local deformation process involves two stages. In Stage 1, the deformation is elastic for a short period of time. In Stage 2, the deformation process becomes nonlinear, plastic and complex [81]. Accurate deterministic/analytical physics equations are not available to uniquely determine the spatio-temporal deformation process. To overcome the difficulty, we propose a statistical model called multivariate general path model for the dynamic material local deformation in Section 3.3.1. Following the model, we develop a two-stage model parameter estimation method in Section 3.3.2.

3.3.1 Multivariate General Path Model

Consider N material samples that are subject to deformation loading. For each sample, p deformation level vs. the time paths that correspond to p local points on the sample are collected. Denote the deformation level of the jth path for the ith sample at time t_k by y_{ijk}. We propose the following multivariate (p-variate) general path model to describe the collected deformation paths:

$$\begin{cases} y_{ijk} = x_{ijk} + \varepsilon_{ijk} = \eta\left(t_k; \boldsymbol{\psi}, \boldsymbol{\varphi}_{ij}\right) + \varepsilon_{ijk} \\ \boldsymbol{\Phi}_i = \left(\boldsymbol{\varphi}_{i1}{}^{\mathrm{T}}, \boldsymbol{\varphi}_{i2}{}^{\mathrm{T}}, \ldots, \boldsymbol{\varphi}_{ip}{}^{\mathrm{T}}\right)^{\mathrm{T}} \sim N\left(\boldsymbol{\mu}_{\boldsymbol{\Phi}}, \boldsymbol{\Sigma}_{\boldsymbol{\Phi}}\right) \\ \varepsilon_{ijk} \sim N\left(0, \sigma^2\right) \end{cases} \tag{18}$$

where x_{ijk} denotes the true deformation level for i = 1, 2,…, N, j = 1, 2, …, p and k = 1, 2, …, m_{ij}; m_{ij} denotes the number of observations in the jth deformation path of the ith sample; $\eta\left(t; \boldsymbol{\psi}, \boldsymbol{\varphi}_{ij}\right)$ is a path function that depends on a fixed-effect parameter vector $\boldsymbol{\psi}$ shared by all the material samples and a random-effect parameter vector $\boldsymbol{\varphi}_{ij}$ for the jth deformation path of the ith sample; and ε_{ijk} is the random normal error with a mean of zero and a variance of σ^2.

In model (18), $\boldsymbol{\Phi}_i$ is assumed to be multivariate normal to capture the statistical dependency among the p deformation paths in a material sample. An alternative way to model the statistical dependency is to assume that some transformation of $\boldsymbol{\Phi}_i$, denoted as $T\left(\boldsymbol{\Phi}_i\right)$, follows a multivariate normal distribution if some prior or physical knowledge is available. In this chapter, we focus on the case when $\boldsymbol{\Phi}_i$ is multivariate normal, the basis on which some closed-form reliability functions can be obtained, which is discussed in Section 3.5.

The proposed multivariate general path model is a generalization of the univariate general path model developed by Lu and Meeker [7], which handles cases when a single degradation

path (e.g., the deformation path) per sample is observed. In our problem, multiple deformation paths for each sample are observed, among which statistical dependencies can exist. Therefore, the univariate general path model cannot be applied to the individual paths separately, and a multivariate general path model is required for modeling those multiple deformation paths while considering their statistical dependencies.

3.3.2 Two-stage Model Parameter Estimation

In the proposed multivariate general path model (18), the set of model parameters is $\Theta = \{\boldsymbol{\mu}_{\Phi}, \boldsymbol{\Sigma}_{\Phi}, \boldsymbol{\psi}, \sigma\}$. We develop a two-stage method to estimate Θ given the deformation path observations.

The proposed model involves both fixed-effect parameters and random-effect parameters. One popular parameter estimation method for such type of models is based on the use of expectation maximization (EM) algorithm, which is a type of MLE method. However, directly applying the EM algorithm for the proposed model is subject to two challenges. First, Θ in practice can be high dimensional when the number of deformation paths observed from a material sample, i.e., p, is large. Applying the EM approach involves maximizing the likelihood function, which is a high-dimensional integration with respect to the random-effect parameters and is difficult to calculate. Second, the deformation path in model (18) can be nonlinear and complex when the deformation mechanism is complex. Thus, directly applying the EM algorithm to estimate the model parameters is computationally intensive and algebraically intractable [7, 82]. To overcome these challenges, we develop a two-stage parameter estimation method that can significantly simplify the parameter estimation for the multivariate general path model. The simulation studies in Section 3.6 show that this two-stage method performs

well in terms of parameter estimation accuracy.

The two-stage method consists of two stages. In Stage 1, the deformation paths of each sample are fitted to a specified path function using the method of least squares, and the parameters are estimated as $\hat{\boldsymbol{\psi}}_i, \hat{\boldsymbol{\Phi}}_i$, and $\hat{\sigma}_i^2$ for i = 1, 2, …, N. The least squares method is applied because it has the asymptotic properties listed in Appendix 3, although other curve fitting methods such as the MLE method could also be used. In Stage 2, we construct the model parameter estimators, denoted by $\hat{\boldsymbol{\psi}}$, $\hat{\boldsymbol{\mu}}_{\boldsymbol{\Phi}}$, $\hat{\boldsymbol{\Sigma}}_{\boldsymbol{\Phi}}$ and $\hat{\sigma}^2$, based on the results from Stage 1. The details of the method are summarized in Algorithm 3.1 as follows.

Algorithm 3.1: The two-stage parameter estimation method.

Stage 1. For each sample, fit a path function using the method of least squares:

for i in 1:N,

$$\left(\hat{\boldsymbol{\psi}}_i, \hat{\boldsymbol{\Phi}}_i\right) = \arg\min_{\boldsymbol{\psi}, \boldsymbol{\Phi}_i} \sum_{j=1}^{p} \sum_{k=1}^{m_{ij}} \left\{ y_{ijk} - \eta\left(t_k; \boldsymbol{\psi}, \boldsymbol{\varphi}_{ij}\right) \right\}^2 \tag{19}$$

$$\hat{\sigma}_i^2 = \left\{ \sum_{j=1}^{p} \sum_{k=1}^{m_{ij}} \left\{ y_{ijk} - \eta\left(t_k; \hat{\boldsymbol{\psi}}_i, \hat{\boldsymbol{\varphi}}_{ij}\right) \right\}^2 \right\} \Big/ \left(m_i - d\right) \tag{20}$$

where $m_i = \sum_{j=1}^{p} m_{ij}$; and d is the dimension of $\left(\boldsymbol{\psi}, \boldsymbol{\Phi}_i\right)$.

Stage 2. Estimate the model parameters using Equations (21) - (23):

$$\hat{\boldsymbol{\psi}} = \frac{1}{N} \sum_{i=1}^{N} \hat{\boldsymbol{\psi}}_i; \ \hat{\boldsymbol{\mu}}_{\boldsymbol{\Phi}} = \frac{1}{N} \sum_{i=1}^{N} \hat{\boldsymbol{\Phi}}_i \tag{21}$$

$$\hat{\boldsymbol{\Sigma}}_{\boldsymbol{\Phi}} = \frac{1}{N-1} \sum_{i=1}^{N} \left(\hat{\boldsymbol{\Phi}}_i - \hat{\boldsymbol{\mu}}_{\boldsymbol{\Phi}}\right)\left(\hat{\boldsymbol{\Phi}}_i - \hat{\boldsymbol{\mu}}_{\boldsymbol{\Phi}}\right)^{\mathrm{T}} - \frac{1}{N} \sum_{i=1}^{N} \mathrm{var}_{\varepsilon}\left(\hat{\boldsymbol{\Phi}}_i\right) \tag{22}$$

where $\mathrm{var}_{\varepsilon}\left(\hat{\boldsymbol{\Phi}}_i\right)$ denotes the covariance matrix of $\hat{\boldsymbol{\Phi}}_i$ caused by the random errors and is calculated as the $p_{\boldsymbol{\Phi}} \times p_{\boldsymbol{\Phi}}$ lower-right submatrix of

$$\hat{\sigma}^2\left[\dot{\boldsymbol{\eta}}^{\mathrm{T}}\left(\mathbf{t}_i;\hat{\boldsymbol{\psi}},\hat{\boldsymbol{\Phi}}_i\right)\dot{\boldsymbol{\eta}}\left(\mathbf{t}_i;\hat{\boldsymbol{\psi}},\hat{\boldsymbol{\Phi}}_i\right)\right]^{-1}$$, where $p_{\boldsymbol{\Phi}}$ denotes the dimension of $\boldsymbol{\Phi}$;

$$\boldsymbol{\eta}\left(\mathbf{t}_i;\boldsymbol{\psi},\boldsymbol{\Phi}_i\right)=\left(\eta\left(t_{i11};\boldsymbol{\psi},\boldsymbol{\Phi}_i\right),\ldots,\eta\left(t_{ijk};\boldsymbol{\psi},\boldsymbol{\Phi}_i\right),\ldots,\eta\left(t_{ipm_{ip}};\boldsymbol{\psi},\boldsymbol{\Phi}_i\right)\right)^{\mathrm{T}};$$

and $$\dot{\boldsymbol{\eta}}\left(\mathbf{t}_i;\boldsymbol{\psi},\boldsymbol{\Phi}_i\right)=\partial\boldsymbol{\eta}\left(\mathbf{t}_i;\boldsymbol{\alpha},\boldsymbol{\beta}\right)\Big/\partial\left(\boldsymbol{\alpha}^{\mathrm{T}},\boldsymbol{\beta}^{\mathrm{T}}\right)\Big|_{(\boldsymbol{\alpha},\boldsymbol{\beta})=(\boldsymbol{\psi},\boldsymbol{\Phi}_i)}.$$

$$\hat{\sigma}^2=\left(\sum_{i=1}^{N}\sigma_i^2\right)\Big/N \tag{23}$$

Notice that in Equation (22) of computing the covariance matrix $\hat{\boldsymbol{\Sigma}}_{\boldsymbol{\Phi}}$, we observe that the variation caused by the measurement errors in Stage 1 has been subtracted/eliminated. The detailed derivation of Equation (22) is listed in Appendix 3. Moreover, in Algorithm 3.1 the fixed-effect parameter vector $\boldsymbol{\psi}$ in some situations can be represented in the form of $\boldsymbol{\psi}=\left(\boldsymbol{\Lambda}_1^{\mathrm{T}},\boldsymbol{\Lambda}_2^{\mathrm{T}},\ldots,\boldsymbol{\Lambda}_p^{\mathrm{T}}\right)^{\mathrm{T}}$, where $\boldsymbol{\Lambda}_j$ denotes the fixed-effect parameter vector for the jth path in a sample, and $\boldsymbol{\Lambda}_1,\boldsymbol{\Lambda}_2,\ldots,\boldsymbol{\Lambda}_p$ are independent. Two examples are the multivariate power-law path and multivariate exponential path situations, which will later be shown in Section 3.5.2. In these cases, Equation (19) in Stage 1 can be further simplified. Specifically, for sample i let $\boldsymbol{\psi}_i=\left(\boldsymbol{\Lambda}_{i1}^{\mathrm{T}},\boldsymbol{\Lambda}_{i2}^{\mathrm{T}},\ldots,\boldsymbol{\Lambda}_{ip}^{\mathrm{T}}\right)^{\mathrm{T}}$, then parameters $\boldsymbol{\Lambda}_{ij}$ and $\boldsymbol{\varphi}_{ij}$ can be obtained by fitting each observed deformation path individually to a specified path function using the method of least squares, i.e., $\left(\hat{\boldsymbol{\Lambda}}_{ij},\hat{\boldsymbol{\varphi}}_{ij}\right)=\arg\min_{\boldsymbol{\Lambda}_{ij},\boldsymbol{\varphi}_{ij}}\sum_{k=1}^{m_{ij}}\left\{y_{ijk}-\eta\left(t_k;\boldsymbol{\Lambda}_{ij},\boldsymbol{\varphi}_{ij}\right)\right\}^2$ for $j=1,2,\ldots,p$. Some asymptotic properties of the two-stage method are listed in Appendix 3, which are similar to the results in Lu and Meeker [7].

Algorithm 3.1 provides a method for the point estimation of Θ. We further develop a parametric bootstrap method to obtain the interval estimation of Θ in the following Algorithm 3.2.

Algorithm 3.2: The interval estimation of model parameters using parametric bootstrap.

Step 1. Simulate M iterations of deformation data set based on the estimated parameters $\widehat{\Theta}$.

Step 2. For i in 1:M,

estimate the model parameters based on the ith data set using Algorithm 3.1,

denoted as $\widehat{\Theta}_i$;

Step 3. The $100(1-\alpha)\%$ confidence interval of ϑ ($\vartheta \in \Theta$) is estimated as $\left(\hat{\vartheta}_{\alpha/2}, \hat{\vartheta}_{1-\alpha/2}\right)$,

where $\hat{\vartheta}_{\nu}$ is the ν quantile of $\left\{\hat{\vartheta}_1, \hat{\vartheta}_2 ..., \hat{\vartheta}_M\right\}$, and α is the significance level.

3.4 Variance-based Failure Criterion

An important failure characteristic associated with the deformation process illustrated in Figures 3.1 and 3.2 is that the relative deformation rather than the absolute deformation of the local points, is the determinant of the material failure. Therefore, assuming that the failure occurs when the material degradation level reaches a specified threshold value, a failure criterion [83] widely used in the reliability engineering field, cannot be directly applied to our problem as it cannot capture the failure mechanism/characteristic. In this chapter, to account for the failure mechanism we use the variance of local points' deformation levels as a measure of the "relative deformation." That is, we assume the material fails when the variance of local points' deformation levels rather than the absolute deformation level reaches a threshold value. This criterion is justified by a real world deformation data set that we collected by using a designed experiment as illustrated in Figure 3.3. Figure 3.3 (left) represents the Instron 8801 testing machine that we used to conduct a steel deformation experiment, and Figure 3.3 (right) illustrates 40 deformation paths collected from one steel sample. It is observed that as the time increases, the variance among the deformation paths increases until the sample fails. The

detailed description of the experiment is discussed in Section 3.7.

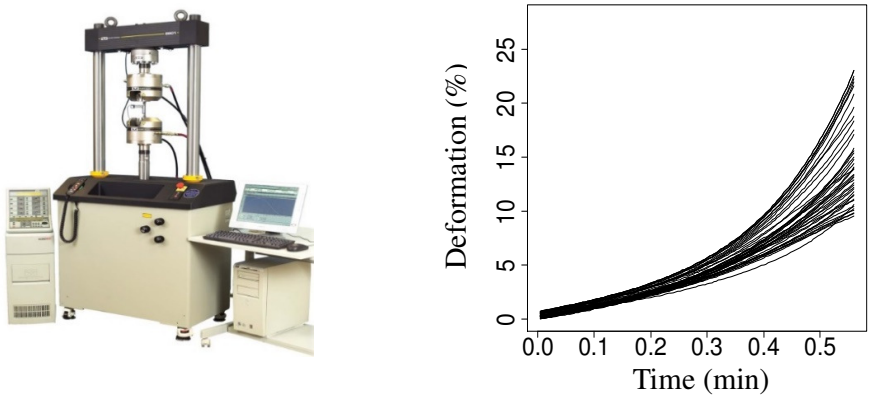

Figure 3.3: Instron 8801 testing system (left) and deformation paths of a sample

The sample variance among p deformation paths at time t can be calculated as

$$S_t = \left(\mathbf{X}_t - \boldsymbol{\upsilon}_t\right)^{\mathrm{T}} \left(\mathbf{X}_t - \boldsymbol{\upsilon}_t\right) \big/ \left(p-1\right) \tag{24}$$

where $\mathbf{X}_t = \left(X_{1t}, X_{2t}, ..., X_{pt}\right)^{\mathrm{T}}$ is the vector of true deformation levels of p local points for a sample at time t; $\boldsymbol{\upsilon}_t$ is a p-dimensional column vector with all elements equaling $\upsilon_t = \frac{1}{p}\sum_{i=1}^{p} X_{it}$.

Thus, the failure occurs when the real-time variance S_t among the deformation paths reaches a threshold value s_{th}. By choosing the variance as a measure of "relative deformation", the closed-form reliability functions for several typical deformation paths can be obtained as illustrated in Section 3.5.

3.5 Reliability Analysis

Reliability analyses are conducted based on the multivariate general path model. In Sections 3.5.1 and 3.5.2, we consider the linear and two typical nonlinear deformation path cases, whose closed-form reliability functions are derived. In Section 3.5.3, we develop a simulation method to compute the reliability function when the deformation paths are general.

3.5.1 Multivariate Linear Path Model

In some special situations, deformation paths of materials can exhibit linearity or approximate linearity under appropriate loading conditions, e.g., when materials undergo the elastic deformation stage [84]. In some other situations, by applying transformations of the deformation data such as the logarithmic transformation, the transformed deformation paths can also be approximately linear. When deformation paths or transformed deformation paths are (approximately) linear, consider a *p*-variate linear path model as a special case of model (18):

$$\begin{cases} \mathbf{Y}_t = \mathbf{X}_t + \boldsymbol{\varepsilon}_t = t\mathbf{a} + \mathbf{b} + \boldsymbol{\varepsilon}_t \\ \begin{pmatrix} \mathbf{a} \\ \mathbf{b} \end{pmatrix} \sim N\left(\begin{pmatrix} \boldsymbol{\mu}_{\mathbf{a}} \\ \boldsymbol{\mu}_{\mathbf{b}} \end{pmatrix}, \begin{pmatrix} \boldsymbol{\Sigma}_{\mathbf{a}} & \boldsymbol{\Sigma}_{\mathbf{ab}} \\ \boldsymbol{\Sigma}_{\mathbf{ba}} & \boldsymbol{\Sigma}_{\mathbf{b}} \end{pmatrix} \right) \\ \boldsymbol{\varepsilon}_t \sim N\left(\mathbf{0}, \boldsymbol{\Sigma}_{\boldsymbol{\varepsilon}}\right); \boldsymbol{\Sigma}_{\boldsymbol{\varepsilon}} \sim \sigma^2 \mathbf{I}_{p\times p} \end{cases} \tag{25}$$

where $\mathbf{Y}_t$ and $\mathbf{X}_t$ denote the observed and true deformation level vector at time *t*, respectively; $\mathbf{a} = \left(a_1, a_2 ..., a_p\right)^{\mathrm{T}}$ is the slope vector; $\mathbf{b} = \left(b_1, b_2 ..., b_p\right)^{\mathrm{T}}$ is the intercept vector; $\boldsymbol{\mu}_{\mathbf{a}} = \left(\mu_{a1}, \mu_{a2}, ..., \mu_{ap}\right)^{\mathrm{T}}$ and $\boldsymbol{\mu}_{\mathbf{b}} = \left(\mu_{b1}, \mu_{b2}, ..., \mu_{bp}\right)^{\mathrm{T}}$ are the mean vectors for $\mathbf{a}$ and $\mathbf{b}$, respectively; $\boldsymbol{\Sigma}_{\mathbf{a}}$ and $\boldsymbol{\Sigma}_{\mathbf{b}}$ are the covariance matrices for $\mathbf{a}$ and $\mathbf{b}$, respectively; $\boldsymbol{\Sigma}_{\mathbf{ab}} = \boldsymbol{\Sigma}_{\mathbf{ba}}{}^{\mathrm{T}}$ is the cross-covariance matrix between $\mathbf{a}$ and $\mathbf{b}$; $\boldsymbol{\varepsilon}_t = \left(\varepsilon_{1t}, \varepsilon_{2t}, ..., \varepsilon_{pt}\right)^{\mathrm{T}}$ is the vector of random measurement errors at time *t*, and $\mathbf{I}_{p\times p}$ is the $p \times p$ dimensional identity matrix.

Based on the multivariate linear path model (25), the real-time variance S_t as defined in (24) conditional on time *t* is a random variable as X_{it} for *i* = 1, 2, …, *p*, are all random variables. We show that S_t can be represented as a linear combination of independent and noncentral chi-squared random variables in Proposition 3. The detailed proof of Proposition 3

is listed in Appendix 4.

Proposition 3. The real-time variance S_t can be represented as a linear combination of independent and noncentral chi-squared random variables, each with one degree of freedom (DOF), i.e.,

$$S_t = \frac{1}{p-1}\sum_{i=1}^{p}\lambda_{it}\Omega_{it};\ \Omega_{it} \sim \chi_1^2\left(c_{it}^2\right) \tag{26}$$

where $\lambda_{1t} \geq \lambda_{2t} \geq ... \geq \lambda_{pt}$ are the eigenvalues of $\mathbf{\Sigma}_t = \mathbf{L}\left[t^2\mathbf{\Sigma_a} + \mathbf{\Sigma_b} + t\left(\mathbf{\Sigma_{ab}} + \mathbf{\Sigma_{ba}}\right)\right]\mathbf{L}^{\mathrm{T}}$; $\mathbf{L} = \mathbf{I}_{p\times p} - \mathbf{1}_{p\times p}/p$; Ω_{it} is a non-central chi-squared random variable with DOF = 1 and a non-centrality parameter of c_{it}^2; $\mathbf{c}_t = \left(c_{1t},...,c_{pt}\right)^{\mathrm{T}} = \mathbf{Q}^{\mathrm{T}}\mathbf{\Sigma}_t^{-1/2}\boldsymbol{\mu}_t$; $\mathbf{Q}$ is an orthogonal matrix such that $\mathbf{Q}^{\mathrm{T}}\mathbf{\Sigma}_t\mathbf{Q} = \mathrm{diag}\left(\lambda_{1t},\lambda_{2t},...,\lambda_{pt}\right)$; $\boldsymbol{\mu}_t = \mathbf{L}\left(t\boldsymbol{\mu}_{\mathbf{a}} + \boldsymbol{\mu}_{\mathbf{b}}\right)$; and $\mathbf{1}_{p\times p}$ is a $p\times p$ dimensional matrix with all entries equaling 1.

Based on the real-time variance representation in Proposition 3, the reliability function can be derived given a failure threshold value of variance. The exact reliability function is not achievable due to the model complexity. We derive an approximate reliability function in Proposition 4. The detailed proof of Proposition 4 is listed in Appendix 5.

Proposition 4. When the threshold variance of failure is specified as s_{th}, the reliability function can be approximated by

$$R\left(t;s_{th},\Theta\right) = \frac{s_{th}^{\ p/2}e^{-s_{th}/(2\beta)}}{(2\beta)^{p/2+1}\Gamma\left(p/2+1\right)} \times \sum_{i=0}^{M}\frac{i!m_i}{\left(p/2+1\right)_i}L_i^{(p/2)}\left(\frac{\left(p+2\right)s_{th}}{4\beta\mu_0}\right) \tag{27}$$

where $L_i^{(\alpha)}\left(x\right) = \sum_{m=0}^{i}\frac{\left(-1\right)^m}{m!}\binom{i+\alpha}{i-m}x^m$ for $\alpha > 0$ is the ith generalized Laguerre polynomial; $\left(l\right)_0 = 1$; $\left(l\right)_i = l\left(l+1\right)\cdots\left(l+i-1\right)$; $m_i = \frac{1}{i}\sum_{j=0}^{i-1}m_j d_{i-j}, i \geq 1$; $q = p/2+1$;

$$m_0 = \frac{2(q\beta)^q}{q-\mu_0} \times \exp\left\{-\frac{1}{2}\sum_{i=1}^{p} \frac{c_{it}^2 \lambda_{it}(q-\mu_0)}{(p-1)\beta\mu_0 + \lambda_{it}(q-\mu_0)}\right\} \times \prod_{i=1}^{p}\left(\beta\mu_0 + \frac{\lambda_{it}}{p-1}(q-\mu_0)\right)^{-1/2} \quad ;$$

$$d_j = -\frac{j\beta q}{2\mu_0(p-1)^p}\sum_{i=1}^{p} c_{it}^2 \lambda_{it}\left(\beta - \frac{\lambda_{it}}{p-1}\right)^{j-1}\left(\frac{\mu_0(p-1)}{(p-1)\beta\mu_0 + \lambda_{it}(q-\mu_0)}\right)^{j+1} + \left(\frac{-\mu_0}{q-\mu_0}\right)^j +$$

$\frac{1}{2}\sum_{i=1}^{p}\left(\frac{\mu_0(\beta(p-1)-\lambda_{it})}{(p-1)\beta\mu_0 + \lambda_{it}(q-\mu_0)}\right)^j$, $j \geq 1$; M is the number of items used for the approximation; μ_0 and β are ancillary parameters that satisfy $0 < \mu_0 < q/2$ and $\beta > 0$. For more details on the effect of μ_0 and β, one can refer to the article by Martínez and Blázquez [85].

Proposition 4 provides an approximation for the reliability function. To quantify the approximation accuracy, we derive the error bound in Proposition 5. The detailed proof of Proposition 5 is listed in Appendix 6.

Proposition 5. The approximation error $e(t; s_{th}, \Theta) = \left|R(t; s_{th}, \Theta) - \widetilde{R}(t; s_{th}, \Theta)\right|$, where $\widetilde{R}(t; s_{th}, \Theta)$ denotes the true reliability function evaluated at time t under failure threshold s_{th}, can be bounded as

$$\begin{aligned} e(t; s_{th}, \Theta) \leq & \frac{q e^{-s_{th}/(2\beta)}}{|q-\mu_0|\Gamma(q)} \times \left(\frac{q s_{th}}{2\beta\mu_0}\right)^{p/2} \times \prod_{i=1}^{p}\left|1 + \frac{\lambda_{it}}{\beta(p-1)}(q/\mu_0 - 1)\right|^{-1/2} \times \\ & \exp\left\{-\frac{1}{4}\sum_{i=1}^{p}\frac{c_{it}^2(\lambda_{it}/\beta)(q/\mu_0-1)}{p-1+(\lambda_{it}/\beta)(q/\mu_0-1)}\right\} \times \exp\left\{\frac{\mu_0\sum_{i=1}^{p} c_{it}^2}{2q\varepsilon} + \frac{(p+2)s_{th}}{8\beta\mu_0}\right\} \times \sum_{k=M+1}^{+\infty} b_k \end{aligned} \tag{28}$$

where $b_k = \varepsilon^k\left(1+\frac{p}{k}\right)^k\left(1+\frac{k}{p}\right)^q$; $\varepsilon = \max(\xi_1, \xi_2)$; $\xi_1 = \left|\frac{\mu_0}{(p/2+1)-\mu_0}\right|$; $\xi_2 = \max_i\left\{\left|\frac{1-\alpha_i/\beta}{1+(\alpha_i/\beta)((p/2+1)/\mu_0 - 1)}\right|\right\}$; and $\alpha_i = \lambda_{it}/(p-1)$. For $\mu_0 < q/2$, Equation (28) is absolutely convergent since $\varepsilon \in (0,1)$.

Propositions 3 – 5 summarize the reliability analysis when the deformation paths are statistically dependent. In some special situations, the deformation dependency among the local

points can be ignored, e.g., when the relative distances among the local points are large. This is due to the fact that the deformation dependency often decreases as the relative distances among those local points increase. When the relative distances are large enough, the deformation dependency is small and ignorable, i.e., the p deformation paths can be treated as being statistically independent. In these situations, the representation of the real-time variance S_t in Proposition 3 can be simplified and is summarized in Corollary 1. The detailed proof of Corollary 1 is listed in the Appendix 7.

Corollary 1. When the p deformation paths are statistically independent, by assuming $(a_i, b_i)^{\mathrm{T}} \sim N\left((\mu_a, \mu_b)^{\mathrm{T}}, \mathbf{\Sigma}\right)$ and $\mathbf{\Sigma} = \begin{pmatrix} \Sigma_{11} & \Sigma_{12} \\ \Sigma_{21} & \Sigma_{22} \end{pmatrix}$, the real-time variance S_t^* can be represented as the product of a time-dependent factor and a non-central chi-squared random variable with p degrees of freedom as follows:

$$S_t^* = \frac{\sigma_t^2}{p-1}\Omega_t^*;\ \Omega_t^* \sim \chi_p^2\left(p\mu_t^2/\sigma_t^2\right) \tag{29}$$

where $\sigma_t^2/(p-1)$ is a time-dependent factor; $\sigma_t^2 = t^2\Sigma_{11} + \Sigma_{22} + 2t\Sigma_{12}$; Ω_t^* is a non-central chi-squared random variable with DOF = p and a non-centrality parameter of $\lambda = p\,\mu_t^2/\sigma_t^2$; and $\mu_t = \mu_a t + \mu_b$.

Furthermore, when the p deformation paths are statistically independent as assumed in Corollary 1, the exact and closed-form reliability function is achievable and derived in Corollary 2. The detailed proof of Corollary 2 is listed in Appendix 8.

Corollary 2. When the p deformation paths are statistically independent, the exact and closed-form reliability function is

$$R^*(t; s_{th}, \Theta) = 1 - Q_{p/2}\left(\sqrt{p}\,\mu_t/\sigma_t, \sqrt{(p-1)\,s_{th}}/\sigma_t\right) \tag{30}$$

where $Q_m(a,b) = \exp\left(-\left(a^2+b^2\right)/2\right)\sum_{k=1-m}^{+\infty}(a/b)^k I_k(ab)$ is the Marcum Q-function; and $I_\alpha(x) = \sum_{m=0}^{+\infty}(x/2)^{2m+1}\Big/\left(m!\Gamma(m+\alpha+1)\right)$ is the modified Bessel function.

3.5.2 Special Nonlinear Multivariate Path Models

Under many situations, the deformation paths are nonlinear due to nonlinear material deformation properties and complex loading conditions, e.g., see Ogi and Takeda [86] and Wu, *et al.* [87]. To account for the nonlinear deformation, we consider two typical cases of nonlinear deformation paths, i.e., the multivariate power law path and the multivariate exponential path. Closed-form reliability functions for these two nonlinear cases are derived. Notice that the power law and exponential paths can be transformed to linear paths so that Section 3.5.1 can apply. In this chapter, we consider them separately because both the power law and exponential models are widely used in various applications, e.g., see Wang and Chu [88] and Alam and Mahapatra [89].

3.5.2.1 Multivariate Power Law Path Model

When the p deformation paths follow the power law, the deformation model can be represented as follows:

$$\begin{cases} \mathbf{Y}_t = \mathbf{X}_t + \boldsymbol{\varepsilon}_t = \mathbf{H}_t\mathbf{a} + \mathbf{b} + \boldsymbol{\varepsilon}_t \\ \mathbf{H}_t = \operatorname{diag}\left(t^{\rho_1}, t^{\rho_2}, ..., t^{\rho_p}\right) \end{cases} \tag{31}$$

where $\rho_1, \rho_2, ..., \rho_p$ are fixed-effect power parameters that capture the nonlinear trend of the deformation paths, which are included in the fixed-effect parameter vector $\boldsymbol{\psi}$. The modeling of coefficient vector $\left(\mathbf{a}^{\mathrm{T}}, \mathbf{b}^{\mathrm{T}}\right)^{\mathrm{T}}$ and random error vector $\boldsymbol{\varepsilon}_t$ is kept the same with that in the multivariate linear path model (25). The model parameters can be estimated using Algorithm 3.1 given the deformation observations.

In model (31), we show that the levels of true deformation paths at time *t*, i.e., $\mathbf{X}_t$, can be written as a linear transformation of $\left(\mathbf{a}^{\mathrm{T}},\mathbf{b}^{\mathrm{T}}\right)^{\mathrm{T}}$. As $\left(\mathbf{a}^{\mathrm{T}},\mathbf{b}^{\mathrm{T}}\right)^{\mathrm{T}}$ is assumed to be multivariate normal, $\mathbf{X}_t$ also follows a multivariate normal distribution. That is,

$$\begin{aligned}\mathbf{X}_t &= \mathbf{H}_t\mathbf{a}+\mathbf{b} = \begin{pmatrix}\mathbf{H}_t & \mathbf{I}_{p\times p}\end{pmatrix}\begin{pmatrix}\mathbf{a}\\ \mathbf{b}\end{pmatrix}\\ &\sim N\left(\begin{pmatrix}\mathbf{H}_t & \mathbf{I}_{p\times p}\end{pmatrix}\begin{pmatrix}\boldsymbol{\mu}_{\mathbf{a}}\\ \boldsymbol{\mu}_{\mathbf{b}}\end{pmatrix},\begin{pmatrix}\mathbf{H}_t & \mathbf{I}_{p\times p}\end{pmatrix}\begin{pmatrix}\boldsymbol{\Sigma}_{\mathbf{a}} & \boldsymbol{\Sigma}_{\mathbf{ab}}\\ \boldsymbol{\Sigma}_{\mathbf{ba}} & \boldsymbol{\Sigma}_{\mathbf{b}}\end{pmatrix}\begin{pmatrix}\mathbf{H}_t^{\mathrm{T}}\\ \mathbf{I}_{p\times p}\end{pmatrix}\right)\end{aligned} \tag{32}$$

Based on (32), we further obtain $\mathbf{Z}_t = \mathbf{X}_t - \boldsymbol{\upsilon}_t = \mathbf{L}\mathbf{X}_t \sim N\left(\boldsymbol{\mu}_t^*,\boldsymbol{\Sigma}_t^*\right)$, where

$$\begin{cases}\boldsymbol{\mu}_t^* = \mathbf{L}\begin{pmatrix}\mathbf{H}_t & \mathbf{I}_{p\times p}\end{pmatrix}\begin{pmatrix}\boldsymbol{\mu}_{\mathbf{a}}\\ \boldsymbol{\mu}_{\mathbf{b}}\end{pmatrix}\\ \boldsymbol{\Sigma}_t^* = \mathbf{L}\begin{pmatrix}\mathbf{H}_t & \mathbf{I}_{p\times p}\end{pmatrix}\begin{pmatrix}\boldsymbol{\Sigma}_{\mathbf{a}} & \boldsymbol{\Sigma}_{\mathbf{ab}}\\ \boldsymbol{\Sigma}_{\mathbf{ba}} & \boldsymbol{\Sigma}_{\mathbf{b}}\end{pmatrix}\begin{pmatrix}\mathbf{H}_t^{\mathrm{T}}\\ \mathbf{I}_{p\times p}\end{pmatrix}\mathbf{L}^{\mathrm{T}}\end{cases} \tag{33}$$

Using $\boldsymbol{\mu}_t^*$ and $\boldsymbol{\Sigma}_t^*$ in Equation (33) to replace $\boldsymbol{\mu}_t$ and $\boldsymbol{\Sigma}_t$ in Equation (26), respectively, all the results in Propositions 3 – 5 and Corollaries 1 - 2 hold for the multivariate power law path case. That is, the representation of real-time variance under the variance definition (24), the approximate reliability function under the specified failure threshold s_{th}, and the corresponding approximation error bound are calculated. When the deformation paths are statistically independent, the real-time variance representation and the closed-form reliability function are obtained.

3.5.2.2 Multivariate Exponential Path Model

Another typical nonlinear deformation path model we consider is the multivariate exponential path model. For this model, we only need to replace $\mathbf{H}_t$ in model (31) by the following $\mathbf{H}_t^*$:

$$\mathbf{H}_t^* = \mathrm{diag}\left(e^{\eta_1 t}, e^{\eta_2 t},\ldots,e^{\eta_p t}\right) \tag{34}$$

where $\eta_1, \eta_2, ..., \eta_p$ are the fixed-effect coefficients of the exponential paths, which are included in the fixed-effect parameter vector $\boldsymbol{\psi}$. Algorithm 3.1 can then be applied to estimate the model parameters.

Similar results regarding reliability analyses using this multivariate exponential path model compared to those of the multivariate power law path model can be obtained, while only a slight change needs to be made, i.e., replace $\mathbf{H}_t$ in Equation (33) with $\mathbf{H}_t^*$ in (34).

3.5.3 Multivariate General Path Model

In some other situations, the deformation paths can be more complex than those following a linear law, a power law or an exponential law, e.g., when the material property and deformation mechanism are complicated. When the deformation paths are general, under most situations the analytical or closed-form reliability function is not available. To handle these situations, we develop a simulation procedure to compute the reliability function $R(t; s_{th}, \Theta)$ as summarized in Algorithm 3.3.

Algorithm 3.3: Calculation of reliability function for the multivariate general path model.

Step 1. Estimate the model parameters as $\hat{\boldsymbol{\mu}}_{\boldsymbol{\Phi}}, \hat{\boldsymbol{\Sigma}}_{\boldsymbol{\Phi}}, \hat{\boldsymbol{\psi}}$ and $\hat{\sigma}^2$ using the two-stage parameter estimation method (see Section 3.3.2);

Step 2. Generate N random realizations of random-effect parameters $\boldsymbol{\Phi}_i$ from $N\left(\hat{\boldsymbol{\mu}}_{\boldsymbol{\Phi}}, \hat{\boldsymbol{\Sigma}}_{\boldsymbol{\Phi}}\right)$, and thereafter simulate $N \times p$ deformation paths;

Step 3. For sample i in 1: N, compute the real-time variance among the deformation paths;

Step 4. Based on the specified variance threshold s_{th} of failure, compute the corresponding failure time t_i for i in 1: N;

Step 5: Estimate the reliability function as the proportion of survived samples by time t,

i.e., $R\left(t;s_{th},\widehat{\Theta}\right)=\left(\text{number of } t_i>t\right)/N$.

In addition to the point estimation of $R\left(t;s_{th},\Theta\right)$, we further develop a parametric bootstrap method to obtain the interval estimation of $R\left(t;s_{th},\Theta\right)$ in Algorithm 3.4.

Algorithm 3.4: The interval estimation of $R\left(t;s_{th},\Theta\right)$.

Step 1. Simulate M iterations of deformation data set based on the estimated parameters $\widehat{\Theta}$.

Step 2. For i in 1:M,

<u>Step 2.1</u>: estimate the model parameters based on the ith data set using Algorithm 3.1, denoted as $\widehat{\Theta}_i$;

<u>Step 2.2</u>: estimate the reliability function based on $\widehat{\Theta}_i$ using Algorithm 3.3, denoted as $R\left(t;s_{th},\widehat{\Theta}_i\right)$.

Step 3. The $100\left(1-\alpha\right)\%$ pointwise confidence interval of $R\left(t;s_{th},\Theta\right)$ is estimated as $\left(R_{\alpha/2}\left(t;s_{th},\widehat{\Theta}\right),R_{1-\alpha/2}\left(t;s_{th},\widehat{\Theta}\right)\right)$, where $R_{\nu}\left(t;s_{th},\widehat{\Theta}\right)$ is the ν quantile of $\left\{R\left(t;s_{th},\widehat{\Theta}_1\right),R\left(t;s_{th},\widehat{\Theta}_2\right)...,R\left(t;s_{th},\widehat{\Theta}_M\right)\right\}$.

3.6 Simulation Study

To verify the developed two-stage model parameter estimation method, a simulation study is implemented. Specifically, we first simulate a deformation path data set based on specified model parameters. Next, we re-estimate the model parameters by using the two-stage parameter estimation method, whose values are compared to the specified parameters to assess the performance of the developed method.

We first consider a single iteration of data simulation. The multivariate power-law path

model (31) is chosen, while other models can be selected using a similar procedure. For simplicity purposes, the dimension of the deformation paths is chosen as p = 3. For each deformation path, the time points for the deformation level observation are set as $t_k = k/20$ for k = 1, …, 20. The sample size is chosen as N = 500. The model parameters are set as follows:

$$\begin{cases} \boldsymbol{\theta} = \left(\boldsymbol{\mu}_{\mathbf{a}}{}^{\mathrm{T}}, \boldsymbol{\mu}_{\mathbf{b}}{}^{\mathrm{T}}\right)^{\mathrm{T}} = (10, 20, 30, 3, 5, 7)^{\mathrm{T}} \\ (\rho_1, \rho_2, \rho_3) = (1.0, 1.5, 2.0);\ \sigma^2 = 0.2 \\ \boldsymbol{\Sigma}_{\boldsymbol{\theta}} = \begin{bmatrix} 2 & 0.5 & 0.5 & 0.5 & 0.5 & 0.5 \\ & 4 & 0.5 & 0.5 & 0.5 & 0.5 \\ & & 6 & 0.5 & 0.5 & 0.5 \\ & & & 0.6 & 0.5 & 0.5 \\ & SYM & & & 1.0 & 0.5 \\ & & & & & 1.4 \end{bmatrix} \end{cases}$$

where "SYM" indicates that $\boldsymbol{\Sigma}_{\boldsymbol{\theta}}$ is symmetric.

Based on the specified model parameters, deformation paths for all the samples are simulated. Figure 3.4 illustrates the simulated paths of ten randomly chosen samples in one realization of simulation. The variates 1 – 3 represent the three dimensions of the deformation paths for each sample.

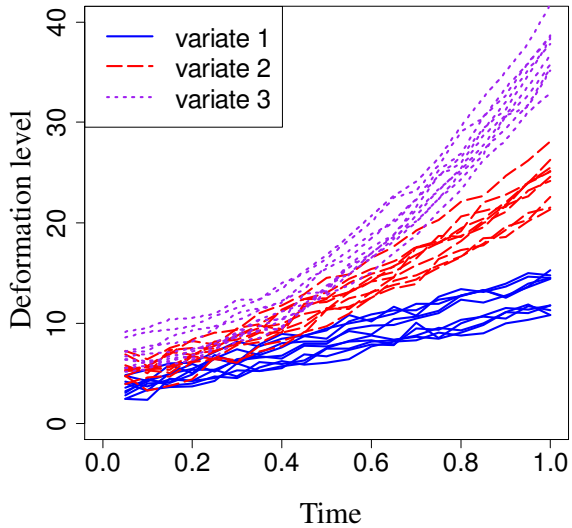

Figure 3.4: Simulated deformation paths of ten samples

The two-stage parameter estimation method, i.e., Algorithm 3.1, is then applied to the simulated deformation paths to estimate the model parameters. The estimated parameters are:

$$\begin{cases} \hat{\boldsymbol{\theta}} = (9.91, 20.02, 29.94, 2.93, 4.99, 6.94)^{\mathrm{T}} \\ (\hat{\rho}_1, \hat{\rho}_2, \hat{\rho}_3) = (1.005, 1.506, 2.003);\ \hat{\sigma}^2 = 0.202 \\ \hat{\boldsymbol{\Sigma}}_{\boldsymbol{\theta}} = \begin{bmatrix} 1.92 & 0.56 & 0.44 & 0.53 & 0.51 & 0.50 \\ & 3.96 & 0.48 & 0.54 & 0.45 & 0.49 \\ & & 6.24 & 0.46 & 0.44 & 0.40 \\ & & & 0.66 & 0.54 & 0.49 \\ & SYM & & & 1.05 & 0.46 \\ & & & & & 1.38 \end{bmatrix} \end{cases}$$

It is observed that the estimated parameters are close to the true parameters, indicating that the two-stage parameter estimation method performs well. Furthermore, based on Algorithm 3.2 the 95% confidence intervals (CIs) for the model parameters are computed by setting the number of iterations as M=1000. The lower and upper bounds (denoted as LBs and UBs, respectively) are listed as follows:

$$\text{LBs:}\begin{cases}\hat{\boldsymbol{\theta}}_{0.025}=\left(9.84,19.85,29.74,2.80,4.89,6.83\right)^{\mathrm{T}}\\ \hat{\boldsymbol{\rho}}_{0.025}=\left(0.997,1.497,1.998\right);\ \hat{\sigma}^{2}_{0.025}=0.198\\ \hat{\boldsymbol{\Sigma}}_{\boldsymbol{\theta},0.025}=\begin{bmatrix}1.86 & 0.31 & 0.13 & 0.23 & 0.36 & 0.34\\ & 3.58 & 0.03 & 0.37 & 0.19 & 0.29\\ & & 5.60 & 0.24 & 0.21 & 0.10\\ & & & 0.58 & 0.45 & 0.38\\ & SYM & & & 0.91 & 0.33\\ & & & & & 1.26\end{bmatrix}\end{cases}$$

$$\text{UBs:}\begin{cases}\hat{\boldsymbol{\theta}}_{0.975}=\left(10.09,20.20,30.17,3.04,5.07,7.04\right)^{\mathrm{T}}\\ \hat{\boldsymbol{\rho}}_{0.975}=\left(1.019,1.513,2.008\right);\ \hat{\sigma}^{2}_{0.975}=0.209\\ \hat{\boldsymbol{\Sigma}}_{\boldsymbol{\theta},0.975}=\begin{bmatrix}2.39 & 0.83 & 0.74 & 0.57 & 0.66 & 0.66\\ & 4.58 & 0.94 & 0.70 & 0.58 & 0.71\\ & & 7.15 & 0.66 & 0.65 & 0.62\\ & & & 1.02 & 0.65 & 0.61\\ & SYM & & & 1.28 & 0.57\\ & & & & & 1.64\end{bmatrix}\end{cases}$$

Next, to quantitatively assess the accuracy of parameter estimation, we repeat the aforementioned simulation process for K=1000 times and compute the Root Mean Square Errors (RMSEs) of the estimators. That is, for $\vartheta\in\Theta$, $\mathrm{RMSE}\left(\hat{\vartheta}\right)=\sqrt{\sum_{k=1}^{K}\left(\hat{\vartheta}_k-\vartheta\right)^2\Big/K}$, where $\hat{\vartheta}_k$ is the estimated value of ϑ in the kth iteration, and ϑ is the true value. The results are summarized in the following 3.1, where $\boldsymbol{\mu}_{\mathbf{a}}=\left(\mu_1,\mu_2,\mu_3\right)^{\mathrm{T}}$ and $\boldsymbol{\mu}_{\mathbf{b}}=\left(\mu_4,\mu_5,\mu_6\right)^{\mathrm{T}}$. It is observed that the RMSEs are generally small under the current sample size.

Table 3.1: RMSEs of parameter estimators

Parameter $\hat{\vartheta}$	$\hat{\rho}_1$	$\hat{\rho}_2$	$\hat{\rho}_3$	$\hat{\sigma}^2$	$\hat{\mu}_1$	$\hat{\mu}_2$	$\hat{\mu}_3$
RMSE($\hat{\vartheta}$)	0.006	0.003	0.003	0.002	0.078	0.093	0.110
Parameter $\hat{\vartheta}$	$\hat{\mu}_4$	$\hat{\mu}_5$	$\hat{\mu}_6$	$\hat{\Sigma}_{11}$	$\hat{\Sigma}_{12}$	$\hat{\Sigma}_{13}$	$\hat{\Sigma}_{14}$
RMSE($\hat{\vartheta}$)	0.058	0.048	0.055	0.225	0.136	0.161	0.194

Parameter $\hat{\vartheta}$	$\hat{\Sigma}_{15}$	$\hat{\Sigma}_{16}$	$\hat{\Sigma}_{22}$	$\hat{\Sigma}_{23}$	$\hat{\Sigma}_{24}$	$\hat{\Sigma}_{25}$	$\hat{\Sigma}_{26}$
RMSE($\hat{\vartheta}$)	0.073	0.082	0.267	0.225	0.087	0.117	0.115
Parameter $\hat{\vartheta}$	$\hat{\Sigma}_{33}$	$\hat{\Sigma}_{34}$	$\hat{\Sigma}_{35}$	$\hat{\Sigma}_{36}$	$\hat{\Sigma}_{44}$	$\hat{\Sigma}_{45}$	$\hat{\Sigma}_{46}$
RMSE($\hat{\vartheta}$)	0.395	0.101	0.113	0.139	0.251	0.048	0.054
Parameter $\hat{\vartheta}$	$\hat{\Sigma}_{55}$	$\hat{\Sigma}_{56}$	$\hat{\Sigma}_{66}$	-	-	-	-
RMSE($\hat{\vartheta}$)	0.114	0.061	0.108	-	-	-	-

Moreover, to assess the accuracy of reliability function estimate $R\left(t;s_{th},\widehat{\Theta}\right)$, the Root Mean Integrated Squared Error (RMISE) of $R\left(t;s_{th},\widehat{\Theta}\right)$ is calculated using $\text{RMISE}\left(R\left(t;s_{th},\widehat{\Theta}\right)\right)=\sqrt{\sum_{i=1}^{K}\int_{0}^{\infty}\left(R\left(t;s_{th},\widehat{\Theta}_i\right)-R\left(t;s_{th},\Theta\right)\right)^2 dt\Big/K}$. We set K=1000 and choose two failure threshold values as 15 and 30. The corresponding RMISEs are calculated as 0.0091 and 0.0074, respectively, which are small numbers and indicate that the performance of reliability function estimation is satisfactory.

3.7 Case Study

The proposed model is applied to studying the failure of dual phase (DP) advanced high strength steel, which has been receiving increasing application in the automotive industry, due to their excellent properties such as the extremely high strength and the good formability [90, 91].

In the case study, we conducted physical experiments on four as-received DP 980 steel specimens with a thickness of 1mm. The specimens were all made according to the tensile testing standard of metallic materials [92]. For each specimen, a standard tensile test experiment was conducted by using the Instron 8801 testing system as illustrated in Figure 3.3 (left). Specifically, each specimen was firmly clamped at its two ends and then stretched uniaxially with a constant speed until it fractured, using the same loading condition. The dynamic failure process of each sample was monitored by a DIC device, which is based on a

two-camera system. The DIC device can dynamically track the motion/deformation of a grid of points/pixels on the specimen surface [93]. The resolution of DIC device in our experiment is around 40×40 pixels/mm^2. At each fixed time point, an image of the deformation distribution on the specimen surface can be obtained. As the measurement was dynamic, approximately 1000 deformation distribution images in a time sequence were obtained for each specimen. From the image stream, 40 deformation paths corresponding to 40 randomly chosen local points around the crack area on the specimen surface were collected. Figure 3.3 (right) illustrates the deformation paths collected from a randomly selected steel specimen. It can be clearly observed that as the time increases, the variance among deformation paths increases until the specimen fails, which is consistent with the developed variance-based failure criterion.

The proposed model is applied to analyzing the collected experimental data. Specifically, as the deformation level in Figure 3.3 (right) increases nonlinearly over time, we choose the multivariate power law path model to study the deformation paths. Moreover, considering that the local points from which the deformation paths are collected are randomly chosen and are relatively far from each other on the steel specimen, we assume that the statistical dependency among the deformation paths can be ignored. Specifically, it is assumed in model (31) that $(a_i, b_i, \rho_i)^{\mathrm{T}} \sim N(\boldsymbol{\mu}, \boldsymbol{\Sigma})$. Next, the model parameters of the experimental deformation paths are estimated based on Algorithm 3.1, and the results are summarized as

$$\hat{\boldsymbol{\mu}} = (47.76, 1.18, 2.08)^{\mathrm{T}}; \quad \hat{\sigma} = 0.200$$

$$\hat{\boldsymbol{\Sigma}} = \begin{pmatrix} 467.20 & 7.27 & 6.71 \\ 7.27 & 0.13 & 0.10 \\ 6.71 & 0.10 & 0.11 \end{pmatrix}$$

Notice the unit of degradation is percentage, i.e., 1%. The Mean Squared Error (MSE) of using the power-law model for fitting the deformation paths is computed as 0.04. This small number

indicates that the power-law model fits each individual deformation path satisfactorily. Furthermore, the 95% CIs for the model parameters are computed using Algorithm 3.2 and listed as follows:

$$\begin{cases} \mathrm{CI}(\boldsymbol{\mu}) = \left[\mathrm{CI}(a), \mathrm{CI}(b), \mathrm{CI}(\rho)\right] = \left[(42.86, 55.16), (1.09, 1.31), (2.00, 2.19)\right] \\ \mathrm{CI}(\sigma) = (0.197, 0.201) \\ \mathrm{CI}(\boldsymbol{\Sigma}) = \begin{pmatrix} \mathrm{CI}(\boldsymbol{\Sigma}_{11}) & \mathrm{CI}(\boldsymbol{\Sigma}_{12}) & \mathrm{CI}(\boldsymbol{\Sigma}_{13}) \\ & \mathrm{CI}(\boldsymbol{\Sigma}_{22}) & \mathrm{CI}(\boldsymbol{\Sigma}_{23}) \\ SYM & & \mathrm{CI}(\boldsymbol{\Sigma}_{33}) \end{pmatrix} = \begin{pmatrix} (262.3, 606.7) & (3.92, 9.71) & (3.71, 8.95) \\ & (0.077, 0.18) & (0.057, 0.15) \\ SYM & & (0.062, 0.15) \end{pmatrix} \end{cases}$$

Based on the estimated parameters, given the threshold variance of failure the reliability function of the DP steel can be computed. Specifically, two threshold variances are chosen as $s_{th1} = 5$ and $s_{th2} = 15$. The corresponding two reliability functions are computed based on Algorithm 3.3 and are illustrated in Figure 3.5 (a) and (b), respectively. It can be seen that a higher failure threshold value generally results in a higher reliability value. Furthermore, the 95% point-wise confidence intervals (PCIs) for the two reliability functions are calculated utilizing Algorithm 3.4 and illustrated by the dash curves in Figure 3.5.

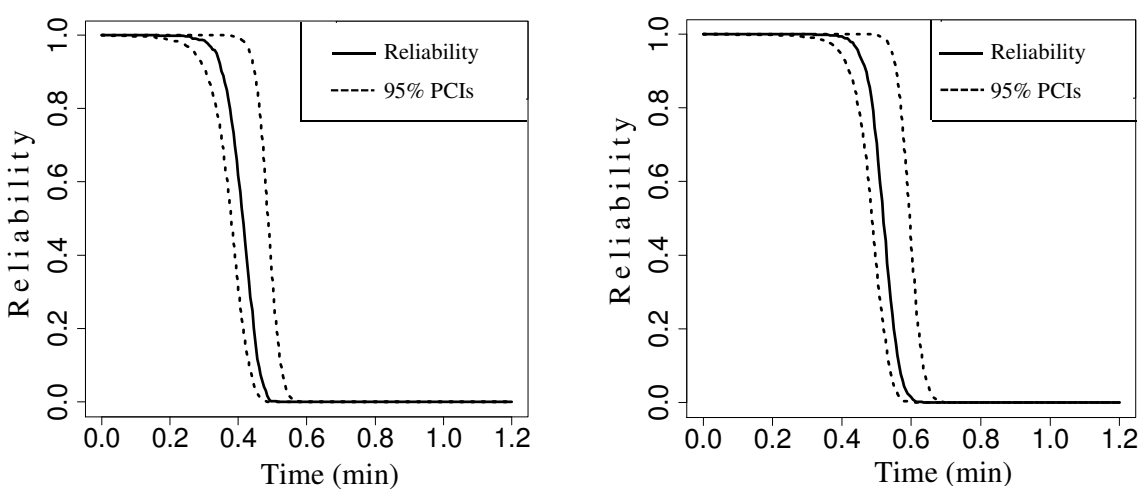

(a) $s_{th} = 5$ (b) $s_{th} = 15$

Figure 3.5: Reliability functions for two failure thresholds and the corresponding 95% PCIs

3.8 Summary

Material failure is strongly affected by the local deformation, which often is a dynamic process. Traditional reliability analyses have ignored the local deformation information and thus are not efficient to model material failure mechanisms. In this chapter, we conduct reliability analysis by utilizing the dynamic local deformation information of steel in a tensile process. Specifically, as multiple deformation paths for each sample are observed over time, we propose a new multivariate general path model that generalizes the existing univariate general path model to describe these deformation paths. To estimate the model parameters, a two-stage method that can overcome the computational complexity is developed. The proposed model not only is flexible to model the deformation data but also can be applied to many other degradation problems, in which multiple degradation curves for each sample are collected. For example, simultaneous propagation of multiple cracks can happen for some materials under a tension condition [94], based on which multiple crack growth paths for each material sample can be obtained. Another example is that multiple performance characteristics of a smart electricity meter can be recorded over time [95], which can be treated as multiple degradation paths.

To account for the failure mechanism in material local deformation, we use a new variance-based failure criterion. Reliability analyses are conducted by applying the failure criterion on the developed multivariate general path model. In particular, we derive closed-form reliability functions for the multivariate linear path, the multivariate power law path, and the multivariate exponential path situations. When the deformation paths are general, we develop a simulation-based algorithm to compute the reliability function. The developed methods are verified and

illustrated by simulation studies and a designed case study.

In this chapter, deformation paths of several local points on material samples are utilized to conduct material reliability analysis due to the limitation of the current experimental technique. In the future, an interesting research topic would be to improve the experimental technique and obtain the dynamic deformation information of all the grid of points on those material samples. In that case, the complex structure of spatio-temporal correlation among the points may not be ignorable, and more sophisticated methods need to be developed for the modeling. Furthermore, the variance-based failure criterion is used to capture the material failure mechanism in this chapter. In the future, another interesting research topic would be to refine the criterion to capture the failure mechanism more precisely, e.g., we may consider the variation of failure threshold values among different material samples.

The methodologies proposed in this chapter has been published in journal article [96].

CHAPTER 4. RELIABILITY ANALYSIS BY CONSIDERING STEEL MICROSTRUCTURE INFORMATION

4.1 Overview

Material microstructure has been well known to strongly influence material macroscopic properties such as strength, hardness, toughness, and wear resistance, which in turn affect material service lifetime. In the reliability literature, most existing research conducts reliability analysis either based on lifetime data or degradation data. None of these studies takes material microstructure image information into consideration. In this chapter, considering material microstructure's strong effect on material reliability, we conduct reliability analysis of advanced high strength steel by utilizing material microstructure image information. Specifically, the material lifetime distribution, which is assumed to belong to a log-location-scale family, is predicted by utilizing material microstructure images. For the prediction, we propose a novel statistical model named distribution-based functional linear model, in which the microstructure effect on both the location and scale parameters of lifetime distribution is formulated. The proposed model generalizes the existing functional linear regression model. A maximum penalized likelihood method is developed to estimate model parameters. A simulation study is conducted to illustrate the developed methods. Physical experiments on advanced high strength steel are also designed and conducted to demonstrate the proposed model. The results show that the proposed model predicts material lifetime much more precisely than existing models that ignore material microstructure image information.

4.2 Introduction

Material microstructure refers to a small scale structure of a material, defined as the structure of a prepared material surface as revealed by a microscope using a magnification no

less than 25× [97]. Figure 4.1 (left) illustrates a type of dual-phase (DP) advanced high strength steel that has been recently applied in automotive industry. Figure 4.1 (right) shows a microstructure image of the DP steel with a real size of 100×100 um, in which the black and white areas represent two different phases, termed as the martensite phase and the ferrite phase, respectively.

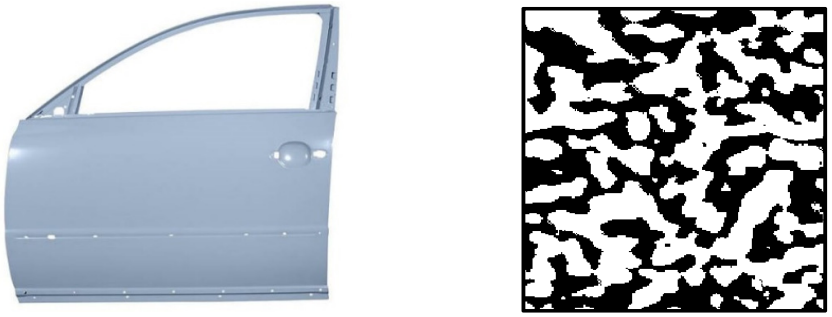

Figure 4.1: High strength dual-phase steel (left) and its microstructure image (right)

In the materials science field, material microstructure is well known to strongly influence material macroscopic properties such as strength, ductility, hardness, toughness, and wear resistance [24, 25]. These macroscopic properties, in turn, strongly influence material service lifetime: often a material with higher strength has a longer service lifetime [98].

In the reliability engineering field, material reliability analysis such as material life/failure prediction has received increasing attention as it quantifies the quality and reliability of a material (or a product made of that material). In literature, lifetime data based models and degradation data based models have been widely developed to study and predict material reliability/failure. For the lifetime data based models, parametric distributions such as the Weibull, Lognormal, and Gamma are usually used to model collected failure time data. For example, Mukhopadhyay [99] conducted reliability analysis based on masked series system

lifetime data by choosing the Lognormal as the lifetime distribution. Hong, *et al.* [2] developed a remaining life prediction based on left truncated and right censored lifetime data by choosing the Weibull and Lognormal as lifetime distributions. For more studies on lifetime data based reliability analysis, one can refer to Lawless [11]. In terms of degradation data based reliability models, general path models and stochastic process models have been developed to describe the degradation data. For example, Lu and Meeker [7] developed a general path based reliability model, in which the model parameters are assumed to follow a multivariate normal distribution. Lawless and Crowder [36] conducted reliability analysis by formulating the degradation data using a gamma process model. Ye, *et al.* [13] conducted reliability analysis by formulating the degradation data using a Wiener process model. For more research on degradation data based reliability analysis, refer to a review paper by Gorjian, *et al.* [50]. Although significant progress has been made in the reliability research, none of the existing studies takes material microstructure image information into consideration.

As material microstructure strongly impacts material service lifetime, incorporating the microstructure image information into reliability analysis will improve the performance of failure prediction, compared to failure predictions using conventional reliability models that ignore the microstructure information. This will be illustrated by a real world case study (see section 4.6). To incorporate material microstructure image information into reliability analysis, one challenge is that the microstructure topology is very complex and highly dimensional, which makes it difficult to quantitatively describe the microstructure. Moreover, no quantitative physical knowledge/equation is available to formulate the relationship between the material reliability/failure and material microstructure.

In this chapter, we propose a novel statistical model named distribution-based functional linear model (DFLM) for reliability analysis by utilizing material microstructure image information. The proposed DFLM is a generalization of an existing functional linear regression model [100]. Based on the DFLM, the material lifetime distribution that is assumed to belong to a log-location-scale family is predicted given material microstructure images. Specifically, provided with a microstructure image, we first compute its two-point correlation function that can preserve statistical properties of the image to a certain level. Next, based on the DFLM using the two-point correlation function as model input, the corresponding material lifetime distribution is calculated.

The remainder of this chapter is organized as follows. In Section 4.3, the DFLM is proposed. In Section 4.4, a maximum penalized likelihood estimation method is developed for model parameter estimation. In Section 4.5, a simulation study is implemented to assess the performance of the developed methods. In Section 4.6, physical experiments are designed and conducted to demonstrate the proposed model. Finally, in Section 4.7 the chapter is concluded, and areas of future work are discussed.

4.3 Statistical Model

We predict material lifetime distribution by utilizing material microstructure images using a two-step framework, as illustrated in Figure 4.2. In Step 1, as the microstructure image illustrated in Figure 4.2 (a) involves high dimension and complex topology which make quantitative analyses of the microstructure image difficult, we compute its two-point correlation function [101] that preserves statistical properties of the microstructure up to the second order, denoted as $X(r)$ as illustrated in Figure 4.2 (b). In Step 2, based on the computed

$X(r)$, a DFLM is proposed to predict material lifetime distribution as illustrated in Figure 4.2 (c). In the following Section 4.3.1 we introduce the two-point correlation function, and in Section 4.3.2 we present the DFLM.

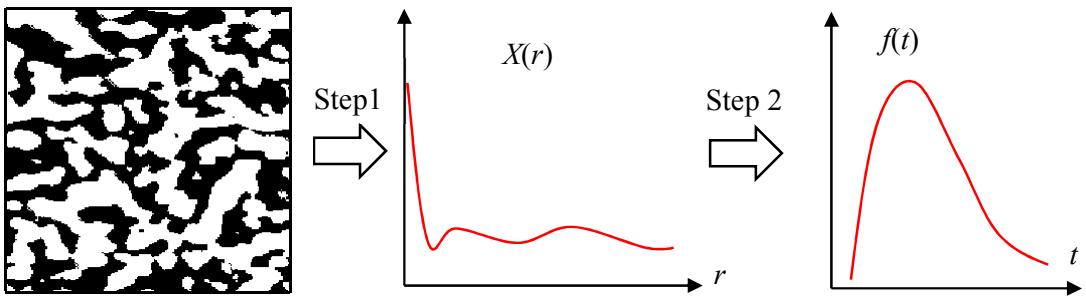

(a) A microstructure image (b) Two-point correlation function (c) Lifetime distribution

Figure 4.2: The framework of lifetime prediction using material microstructure image

4.3.1 The Two-point Correlation Function

The two-point correlation function has been shown as an efficient statistical tool to characterize statistical properties of a dual-phase random medium (such as the DP steel microstructure, which is assumed to be stationary and homogeneous across a steel sample), and has been widely applied in materials science [102, 103]. It characterizes the spatial statistics of random media up to the second order. Specifically, the first and second order spatial statistics refer to volume fraction and distribution auto-covariance of the phases, respectively.

To define the two-point correlation function, consider a square microstructure image of a dual-phase material, which is discretized into $d \times d$ pixels. Let S_{ij} ($S_{ij} \in \{1,2\}$) denote the value of the pixel at coordinate (i, j) on the image, where 1 and 2 represent the black and white phases, respectively, and $i, j \in \{1,...,d\}$. S_{ij} is determined through a preliminary process that converts the original grayscale microstructure images to binary microstructure images following the research in the literature (e.g., see Wong and Sahoo [104] and Russ and

Woods [105]). During the process, a threshold value of gray level can be set. For the pixel at coordinate (*i, j*), if its gray level (0-255) is less than the threshold value, S_{ij} is set to 1 (black phase), otherwise S_{ij} is set to 2 (white phase). The two-point correlation function of phase p ($p \in \{1, 2\}$) for isotropic materials, is defined to be the probability that two randomly selected pixels of relative distance *r* are both in phase p as follows [101]:

$$X^{(p)}(r) = \Pr\left(S_{i_1 j_1} = p, S_{i_2 j_2} = p\right) \tag{35}$$

where (i_1, j_1) and (i_2, j_2) are the coordinates of two points on an image with a relative distance *r*, i.e., $\sqrt{(i_1 - i_2)^2 + (j_1 - j_2)^2} = r$.

Equation (35) defines the two-point correlation function for phase *p*. For dual-phase materials, the two-point correlation function of either phase can be derived from that of the other phase [101]. Specifically, given $X^{(1)}(r)$ for phase 1, $X^{(2)}(r)$ for phase 2 can be uniquely determined as

$$X^{(2)}(r) = X^{(1)}(r) - 2\phi_1 + 1 \tag{36}$$

where ϕ_1 is the volume fraction of phase 1.

It can be seen from Equation (36) that using either $X^{(1)}(r)$ or $X^{(2)}(r)$ is sufficient to describe the material microstructure. In this research, for illustration purposes $X^{(1)}(r)$ is used. We suppress the superscript in the notation of $X^{(1)}(r)$ and simply refer to it as $X(r)$, which is calculated as [101]:

$$X(r) = \frac{\sum_{(m,n)\in P}\left[\sum_{i=1}^{d}\sum_{j=1}^{d} S_{ij} S_{(i+m)(j+n)}\right]}{ld^2} \tag{37}$$

where $P = \left\{(m,n) \middle| m^2 + n^2 \le r^2, r \le [d/2]\right\}$ and *l* is the number of elements in set *P*.

4.3.2 A Novel Distribution-based Functional Linear Model

We propose a DFLM to predict material lifetime distribution, with the two-point correlation function $X(r)$ being the model input.

The type of material lifetime distribution needs to be specified. A widely used family of lifetime distributions is the log-location-scale family [3, 106], which has the following form of CDF [107]:

$$F_Y(y;\mu,\sigma) = \Pr(Y \le y) = \Phi\left(\frac{y-\mu}{\sigma}\right) \tag{38}$$

where $Y = \log(T)$; T denotes the lifetime; $-\infty < \mu < +\infty$ is a location parameter; $\sigma > 0$ is a scale parameter; and Φ is the CDF of Y when $\mu = 0$ and $\sigma = 1$. Specifically, in this research we focus on using the log-normal distribution to model lifetime T, as widely assumed in the literature [3, 106], i.e., $\Phi(z) = \int_{-\infty}^{z} 1/\sqrt{2\pi} \times \exp\left(-\omega^2/2\right) d\omega$. Another reason for choosing the log-normal distribution is that under such an assumption, the modeling object Y follows a normal distribution which has tremendous other real world applications.

The material lifetime distribution depends on the material microstructure. To formulate the dependency, we assume that in Equation (38) both the location and scale parameters are adjusted by the material two-point correlation function $X(r)$ as follows:

$$\begin{cases} g_1(\mu) = g_1(\mu_b) + \psi_1(X(r)) \\ g_2(\sigma) = g_2(\sigma_b) + \psi_2(X(r)) \end{cases} \tag{39}$$

where $g_j(x)$ for j = 1 and 2 are monotonic link functions. Specifically, $g_1(x) = x$ as an identity link function is chosen for simplicity purposes, which is widely used for normal response data in the literature [108]; $g_2(x) = \log(x)$ is chosen to ensure that the scale parameter σ is nonnegative; μ_b and σ_b are the baseline location and scale parameters

for all the material samples, respectively; and $\psi_1(\bullet)$ and $\psi_2(\bullet)$ formulate the effect of material microstructure on material lifetime distribution, which in turn accounts for the sample to sample variation of lifetime as microstructures are different for different material samples.

In this chapter, to model the microstructure effect, we specify $\psi_1(\bullet)$ and $\psi_2(\bullet)$ using a functional linear regression (FLR) [100], i.e.,

$$\begin{aligned}\psi_j(X(r)) &= \int_0^1 \left(X(r) - E\left[X(r)\right]\right)\beta_j(r)\,dr \\ &= \int_0^1 X_c(r)\beta_j(r)\,dr;\ j = 1,2\end{aligned} \tag{40}$$

where the $\beta_j(r)$ for j = 1 and 2 are two unknown functional coefficients; the support of $X(r)$ is normalized into a unit interval $[0,1]$ without loss of generality; and $X(r)$ is centered as $X_c(r) = X(r) - E\left[X(r)\right]$, which is to ensure the identifiability of parameters μ_b and σ_b in Equation (39).

The proposed DFLM (as represented by Equations (5) and (6)) incorporates microstructure effects on both the location and scale parameters of the lifetime distribution. Specifically, when we let $\beta_2(r) = 0$ for $r \in [0,1]$, the proposed DFLM degenerates into the FLR model [100]. In most FLR literature, a regression between a functional predictor (such as the two-point correlation function $X(r)$ in our case) and a scalar response is studied, e.g., see Cai and Hall [109], Yuan and Cai [110], and Wu, *et al.* [111]. However, all these existing studies only consider the relationship between the location parameter of the response variable and the functional predictor, while the scale parameter is assumed to be constant. In the real world, the scale parameter can also depend on the functional predictor so that the FLR may not be efficient to model the microstructure effect on material lifetime. Furthermore, when both $\beta_1(r) = 0$ and $\beta_2(r) = 0$ for $r \in [0,1]$, the proposed DFLM degenerates into a conventional reliability

model that ignores the microstructure image information, i.e, a model that fits the failure time data with two distribution parameters, μ_b and σ_b.

In Equation (40), both $X_c(r)$ and $\beta_j(r)$ for j = 1 and 2 are functions with infinite dimensions. To represent them more efficiently, a set of orthogonal basis functions $b_i(r)$ is chosen for i = 1, 2, … that satisfy $\int_0^1 b_m(t)b_n(t)dt = \delta_{mn}$, where $\delta_{mn} = 1$ if $m = n$, and $\delta_{mn} = 0$ if $m \neq n$. Based on the selected basis functions, $X_c(r)$ and $\beta_j(r)$ are represented as the weighted sum of $b_i(r)$ as follows:

$$\begin{cases} \beta_j(r) = \sum_{i=1}^{+\infty} \eta_{ij} b_i(r);\ j = 1,2 \\ X_c(r) = \sum_{i=1}^{+\infty} \rho_i b_i(r) \end{cases} \tag{41}$$

where η_{ij} and ρ_i are coefficients and can be calculated as $\eta_{ij} = \int_0^1 \beta_j(r) b_i(r) dr$ and $\rho_i = \int_0^1 X_c(r) b_i(r) dr$, respectively; $\sum_{i=1}^{+\infty} \eta_{ij}^2 < +\infty$ for j = 1, 2; and $\sum_{i=1}^{+\infty} \eta_{ij}^2 < +\infty$. Notice that the same basis functions are chosen to decompose $\beta_j(r)$ and $X_c(r)$ for simplicity of exposition although this is not a necessary condition.

Based on Equation (41), the microstructure effect $\psi_j(X(r))$ in Equation (40) can be further derived as

$$\psi_j(X(r)) = \int_0^1 X_c(r)\beta_j(r)dr = \sum_{i=1}^{+\infty} \eta_{ij}\rho_i;\ j = 1,2 \tag{42}$$

In Equation (42), the number of summation items is infinite and thus makes the model complicated. To overcome this challenge, we use a truncated version of Equation (42) by choosing its first q items. That is,

$$\psi_j(X(r)) = \sum_{i=1}^{q} \eta_{ij}\rho_i;\ j = 1,2 \tag{43}$$

The truncation in Equation (43) will result in a truncation of lifetime parameters μ and σ in Equation (39). Specifically, μ and σ will be truncated as $\mu = g_1^{-1}\left(g_1(\mu_b) + \sum_{i=1}^{q}\eta_{i1}\rho_i\right)$ and $\sigma = g_2^{-1}\left(g_2(\sigma_b) + \sum_{i=1}^{q}\eta_{i2}\rho_i\right)$. We show that the truncation errors can be bounded in the following Theorem 1. The detailed proof of Theorem 1 is listed in Appendix 9.

Theorem 1: The truncation errors for the lifetime parameters can be bounded as

$$\begin{cases} \mathbf{E}\left[\left(\mathbf{E}\left(\mu^* \middle| L\right) - \mu^*\right)^2\right] \le 4c_1 \sum_{i=q+1}^{+\infty}\eta_{i1}^2 \sum_{i=q+1}^{+\infty}\delta_i^2 \\ \mathbf{E}\left[\left(\mathbf{E}\left(\sigma^* \middle| U\right) - \sigma^*\right)^2\right] \le 4c_2 \sum_{i=q+1}^{+\infty}\eta_{i2}^2 \sum_{i=q+1}^{+\infty}\delta_i^2 \end{cases} \tag{44}$$

where $\mu^* = g_1^{-1}\left(g_1(\mu_b) + \sum_{i=1}^{+\infty}\eta_{i1}\rho_i\right)$ and $\sigma^* = g_2^{-1}\left(g_2(\sigma_b) + \sum_{i=1}^{+\infty}\eta_{i2}\rho_i\right)$ denote the true location and scale parameters without truncation, respectively; $L = g_1(\mu_b) + \sum_{i=1}^{q}\eta_{i1}\rho_i$ and $U = g_2(\sigma_b) + \sum_{i=1}^{q}\eta_{i2}\rho_i$ are the truncation effects; c_i for i = 1 and 2 are bounds that satisfy $\left|h_i'(\bullet)\right|^2 \le c_i$; $h_i(\bullet) = g_i^{-1}(\bullet)$; and $\delta_i^2 = E\left[\rho_i^2\right]$, which satisfies $\sum_{i=1}^{+\infty}\delta_i^2 = \int_0^1 E\left[X_c^{\,2}(t)\right]dt \le 1$. In Theorem 1, the truncation errors will vanish asymptotically as $q \to +\infty$, which is a commonly used assumption in statistical literature [112].

4.4 Model Parameter Estimation

Based on Equations (39) and (43), the model parameters are $\boldsymbol{\theta} = \left(\boldsymbol{\eta}_1^{\mathrm{T}}, \mu_b, \boldsymbol{\eta}_2^{\mathrm{T}}, \sigma_b\right)^{\mathrm{T}}$, where $\boldsymbol{\eta}_j^{\mathrm{T}} = \left(\eta_{1j}, \eta_{2j}, \ldots, \eta_{qj}\right)^{\mathrm{T}}$ for j = 1 and 2. We develop a maximum penalized likelihood estimation (MPLE) method to estimate $\boldsymbol{\theta}$.

Suppose the failure times and microstructure images of N material samples are collected.

For the ith sample, denote the failure time as t_i and the corresponding two-point correlation function computed based on the microstructure image as $X_i(r); r \in [0,1]$ for i = 1, 2, …, N. Let $\mathbf{t} = (t_1, t_2, ..., t_N)^{\mathrm{T}}$ and $\mathbf{y} = (y_1, y_2, ..., y_N)^{\mathrm{T}} = \log(\mathbf{t})$. The log-likelihood function given $\mathbf{y}$ is as follows:

$$l(\boldsymbol{\theta}|\mathbf{y}) = \sum_{i=1}^{N} \log\left[f_Y(y_i; \mu_i, \sigma_i) \right] \tag{45}$$

where $\mu_i = g_1^{-1}\left(\psi_1\left(X_i(r)\right) + g_1(\mu_b)\right)$; $\sigma_i = g_2^{-1}\left(\psi_2\left(X_i(r)\right) + g_2(\sigma_b)\right)$; $g_j^{-1}(x)$ denotes the inverse function of $g_j(x)$ for j = 1, 2; and $\psi_j\left(X_i(r)\right)$ is calculated through Equation (40), in which $E\left[X(r)\right] = \frac{1}{N}\sum_{i=1}^{N} X_i(r)$.

In Equation (45), as the log-normal distribution is chosen to model the lifetime T, $Y = \log(T)$ follows a normal distribution with the following Probability Density Function (PDF) conditioning on the ith material microstructure image:

$$f_Y(y; \mu_i, \sigma_i) = \frac{1}{\sigma_i \sqrt{2\pi}} \exp\left(-\frac{(y - \mu_i)^2}{2\sigma_i^2} \right) \tag{46}$$

where μ_i and σ_i denote the mean and standard deviation of Y for the ith sample, respectively.

By inserting Equation (46) into Equation (45), the log-likelihood function can be further derived as follows:

$$\begin{aligned} l(\boldsymbol{\theta}|\mathbf{y}) &= \sum_{i=1}^{N} \log\left[f_Y(y_i; \mu_i, \sigma_i) \right] \\ &= -\frac{N}{2}\log(2\pi) - \sum_{i=1}^{N} \log(\sigma_i) - \sum_{i=1}^{N} \frac{(y_i - \mu_i)^2}{2\sigma_i^2} \end{aligned} \tag{47}$$

To estimate the model parameters $\boldsymbol{\theta}$, the MLE method aims at maximizing $l(\boldsymbol{\theta}|\mathbf{y})$ with respect to $\boldsymbol{\theta}$. However, as the number of parameters can be large when $\boldsymbol{\eta}_1^{\mathrm{T}}$ and $\boldsymbol{\eta}_2^{\mathrm{T}}$ are high dimensional (i.e., when the number of selected basis functions is large if a high accuracy

is required), directly applying the MLE method is intractable and can cause an overfitting problem [113]. To overcome the challenge, we develop an MPLE approach [114]. Specifically, rather than maximizing the log-likelihood function $l(\boldsymbol{\theta}|\mathbf{y})$, we maximize a penalized log-likelihood function $l_p(\boldsymbol{\theta}|\mathbf{y})$ defined as follows:

$$l_p(\boldsymbol{\theta}|\mathbf{y}) = l(\boldsymbol{\theta}|\mathbf{y}) - \sum_{j=1}^{2} \lambda_j \int_0^1 \beta_j''(r)^2 \, dr \tag{48}$$

where $\sum_{j=1}^{2} \lambda_j \int_0^1 \beta_j''(r)^2 \, dr$ is a penalty term.

In Equation (48), the penalty term measures the wiggliness of model component functions (i.e., the $\beta_j(r)$ in the DFLM), serving to penalize models with overly complicated component functions [113]. The smoothing parameters $\lambda_j's$ control the tradeoff between the "faithfulness" (or the fitting) to the data, as represented by the log-likelihood function $l(\boldsymbol{\theta}|\mathbf{y})$, and the "smoothness" of the solution, as represented by the penalty term [113, 115]. Specifically, when λ_j is large, the penalty term is dominant and the model parameter estimate will be smoother but less accurate; when λ_j is small, the main contribution to $l_p(\boldsymbol{\theta}|\mathbf{y})$ is the log-likelihood $l(\boldsymbol{\theta}|\mathbf{y})$ and the model parameter estimate will track the data more closely (i.e., more accurate) but will be more irregular. In this chapter, we select the penalty term as the squared norm of the second derivative of smooth functions, which has been widely used in the literature [100, 116-118].

Equation (48) involves a selection of smoothing parameters $\Lambda = \{\lambda_1, \lambda_2\}$. In this chapter, a criterion called Validation Generalized Deviance (VGD)[119] is applied to choose Λ. Specifically, the data set is first randomly separated into two sets, i.e., a training set $D_T = \{(X_i(r), t_i); i \in S_T\}$ and a validation set $D_V = \{(X_i(r), t_i); i \in S_V\}$, where S_T and S_V

are two disjoint sets that satisfy $S_T \cup S_V = \{1,2,...,N\}$. Next, Λ are chosen by minimizing the VGD as follows:

$$\widehat{\Lambda} = \arg\min_{\Lambda \in \mathbb{R}^2} \left\{ VGD\left(\Lambda \middle| D_V ; D_T\right) \right\} = \arg\min_{\Lambda \in \mathbb{R}^2} \left\{ -2l\left(\hat{\boldsymbol{\theta}}\left(D_T, \Lambda\right) \middle| D_V\right) \right\} \tag{49}$$

where $\hat{\boldsymbol{\theta}}(D_T, \Lambda)$ is the estimated model parameters using the training set D_T conditional on Λ by maximizing Equation (48); and $l\left(\hat{\boldsymbol{\theta}}\left(D_T, \Lambda\right) \middle| D_V\right)$ is the log-likelihood value for the validation set D_V based on $\hat{\boldsymbol{\theta}}(D_T, \Lambda)$.

Based on the estimated $\widehat{\Lambda}$, by maximizing the penalized log-likelihood function $l_p(\boldsymbol{\theta}|\mathbf{y})$ in Equation (48) with respect to $\boldsymbol{\theta}$, the model parameters can be estimated as

$$\hat{\boldsymbol{\theta}} = \arg\max_{\boldsymbol{\theta} \in \mathbb{R}} l_p\left(\boldsymbol{\theta} \middle| \mathbf{y}\right) \tag{50}$$

For the maximization in (50), the following Theorem 2 is derived to obtain the parameter estimates. The detailed proof of Theorem 2 is listed in Appendix 10.

Theorem 2: the model parameters $\boldsymbol{\theta} = \left[\boldsymbol{\eta}_1^{\mathrm{T}}, \mu_b, \boldsymbol{\eta}_2^{\mathrm{T}}, \sigma_b\right]^{\mathrm{T}}$ can be obtained from $\boldsymbol{\theta}^* = \left[\boldsymbol{\eta}_1^{\mathrm{T}}, \mu_b, \boldsymbol{\eta}_2^{\mathrm{T}}, \sigma_b^*\right]^{\mathrm{T}}$ in which $\sigma_b^* = \log(\sigma_b)$, and $\boldsymbol{\theta}^*$ solves the following equation:

$$\mathbf{C}_1\left(\left(\mathbf{y} - \mathbf{C}_1^{\mathrm{T}}\boldsymbol{\theta}^*\right) \circ \exp\left[\circ\left(-2\mathbf{C}_2^{\mathrm{T}}\boldsymbol{\theta}^*\right)\right]\right) + \mathbf{C}_2\left(\left(\mathbf{y} - \mathbf{C}_1^{\mathrm{T}}\boldsymbol{\theta}^*\right)^{\circ 2} \exp\left[\circ\left(-2\mathbf{C}_2^{\mathrm{T}}\boldsymbol{\theta}^*\right)\right] - \mathbf{1}\right) - 2\boldsymbol{\Omega}\boldsymbol{\theta}^* = \mathbf{0}_{(2q+2)\times 1} \tag{51}$$

where "$\circ$" is the Hadamard operator [120]. Specifically, the Hadamard product $\mathbf{W} = \mathbf{U} \circ \mathbf{V}$ is defined as: $w_{ij} = u_{ij} \times v_{ij}$, where w_{ij}, u_{ij} and v_{ij} are the $(i, j)^{th}$ entries of **W**, **U**, and **V**, respectively. The Hadmard power is defined as: $\mathbf{U}^{\circ k}$ has the $(i, j)^{th}$ entry of u_{ij}^k, and $m^{\circ \mathbf{U}}$ has the $(i, j)^{th}$ entry of $m^{u_{ij}}$, where k and m are two real numbers. Moreover, in Equation (51), $\mathbf{C}_j = \left[\mathbf{c}_{1j}, \mathbf{c}_{2j}, ..., \mathbf{c}_{Nj}\right]$ for $j = 1$ and 2; $\mathbf{c}_{i1}^{\mathrm{T}} = \left[\boldsymbol{\rho}_i^{\mathrm{T}}, 1, \mathbf{0}_{q\times 1}^{\mathrm{T}}, 0\right]$; $\mathbf{c}_{i2}^{\mathrm{T}} = \left[\mathbf{0}_{q\times 1}^{\mathrm{T}}, 0, \boldsymbol{\rho}_i^{\mathrm{T}}, 1\right]$;

$\boldsymbol{\rho}_i = \left(\rho_{i1}, \rho_{i2}, ..., \rho_{iq}\right)^{\mathrm{T}}$ is the coefficient vector for sample i ; $\boldsymbol{\Omega} = \begin{bmatrix} \lambda_1\boldsymbol{\omega} & \mathbf{0}_{q\times1} & \mathbf{0}_{q\times q} & \mathbf{0}_{q\times1} \\ \mathbf{0}_{1\times q} & \mathbf{0}_{1\times1} & \mathbf{0}_{1\times q} & \mathbf{0}_{1\times1} \\ \mathbf{0}_{q\times q} & \mathbf{0}_{q\times1} & \lambda_2\boldsymbol{\omega} & \mathbf{0}_{q\times1} \\ \mathbf{0}_{1\times q} & \mathbf{0}_{1\times1} & \mathbf{0}_{1\times q} & \mathbf{0}_{1\times1} \end{bmatrix}$ is a $(2q+2)\times(2q+2)$ dimensional matrix; and $\mathbf{0}_{i\times j}$ is a $i\times j$ dimensional zero matrix.

Furthermore, we develop a pair-wise bootstrap method to compute the standard errors of the model parameter estimate $\hat{\boldsymbol{\theta}} = \left(\widehat{\boldsymbol{\eta}_1}^{\mathrm{T}}, \widehat{\mu_b}, \widehat{\boldsymbol{\eta}_2}^{\mathrm{T}}, \widehat{\sigma_b}\right)^{\mathrm{T}}$ and smoothing parameter estimate $\widehat{\Lambda} = \left\{\widehat{\lambda_1}, \widehat{\lambda_2}\right\}$. The detailed steps of the pair-wise bootstrap method are listed in Algorithm 4.1.

Algorithm 4.1: Standard error calculation of model parameters.

1. Denote set $X_r = \left\{X_1(r), X_2(r), ..., X_N(r)\right\}$ as the sample of N two-point correlation functions. Based on X_r and the failure time vector $\mathbf{y}$, estimate the model parameters as $\hat{\boldsymbol{\theta}} = \left(\widehat{\boldsymbol{\eta}_1}^{\mathrm{T}}, \widehat{\mu_b}, \widehat{\boldsymbol{\eta}_2}^{\mathrm{T}}, \widehat{\sigma_b}\right)^{\mathrm{T}}$ and the smoothing parameters as $\widehat{\Lambda} = \left\{\widehat{\lambda_1}, \widehat{\lambda_2}\right\}$.
2. For i in 1:M, where M is the number of bootstrap samples,

   Step 2.1: based on X_r and $\hat{\boldsymbol{\theta}}$, simulate the ith failure time vector

   $\mathbf{y}_i = \left(y_{i1}, y_{i2}, ..., y_{iN}\right)^{\mathrm{T}}$ (log-scale), where y_{ij} is sampled from a normal distribution with the mean and standard deviation being calculated using Equations (39) and (43).

   Step 2.2: based on $\left\{X_r, \mathbf{y}_i\right\}$, estimate the model parameters and smoothing parameters for the ith bootstrap sample, denoted as $\widehat{\boldsymbol{\theta}_i}$ and $\widehat{\Lambda_i} = \left\{\widehat{\lambda_{1i}}, \widehat{\lambda_{2i}}\right\}$, respectively.
3. Estimate the standard errors:

   The standard errors of the model parameter estimates are calculated as the square

roots of $diag\left(\hat{\boldsymbol{\Sigma}}\right)$, where $\hat{\boldsymbol{\Sigma}}=\frac{1}{M-1}\sum_{i=1}^{M}\left(\hat{\boldsymbol{\theta}}_i-\bar{\boldsymbol{\theta}}\right)\left(\hat{\boldsymbol{\theta}}_i-\bar{\boldsymbol{\theta}}\right)^{\mathrm{T}}$ and $\bar{\boldsymbol{\theta}}=\frac{1}{M}\sum_{i=1}^{M}\hat{\boldsymbol{\theta}}_i$. The standard errors of $\hat{\lambda}_1$ and $\hat{\lambda}_2$ are calculated as the standard errors of $\left\{\widehat{\lambda_{11}},\widehat{\lambda_{12}},...,\widehat{\lambda_{1M}}\right\}$ and $\left\{\widehat{\lambda_{21}},\widehat{\lambda_{22}},...,\widehat{\lambda_{2M}}\right\}$, respectively.

4.5 Simulation Study

A simulation study is implemented to verify the developed MPLE method, and errors of the model parameter estimates are investigated.

We first simulate a set of material microstructure images and lifetimes based on specified model parameters. Specifically, the sample size is chosen as $N=200$. The material microstructure images are generated following methods by Jiao, *et al.* [121] given material two-point correlation functions. For details on the microstructure simulation, see Jiao, *et al.* [121]. Subsequently, to simulate failure times based on the simulated microstructure images, the baseline parameters μ_b and σ_b are specified as 0 and 1, respectively. The two functional coefficients are specified as $\beta_1(r)=5\left(\sin(2r)+\cos(4r)+\cos(6r)\right)$ and $\beta_2(r)=2\left(\sin(3r)+\cos(5r)+\cos(7r)\right)$. The support $[0,1]$ of distance r is discretized using 100 points with equal spaces, i.e., $0=r_1<r_2,...,<r_{100}=1$. The simulated $\beta_1(r)$ and $\beta_2(r)$ are illustrated in Figure 4.3.

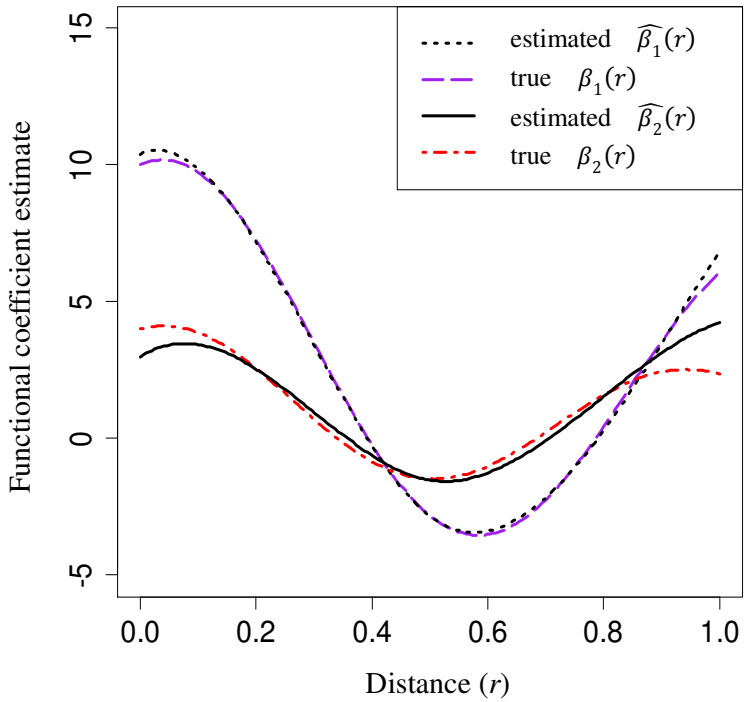

Figure 4.3: Estimated vs. true functional coefficients

Based on the simulated data set, the developed MPLE method is applied to estimating the model parameters, whose values are further compared to the true parameters to assess the performance of the MPLE. Specifically, we choose the orthogonal cubic spline functions as basis functions, and the number of basis functions is set as $q=5$ while a larger q can increase the accuracy if necessary. Based on the MPLE method, the model parameters are estimated by solving Equation (51). Specifically, we repeated the process for M = 5000 times, the average smoothing parameter estimates are calculated as $\hat{\lambda}_1 = 7.42\times10^{-4}$ and $\hat{\lambda}_2 = 3.76\times10^{-6}$ based on Equation (49). The average baseline location and scale parameter estimates are $\widehat{\mu_b} = 0.0006$ and $\widehat{\sigma_b} = 0.972$, respectively, which are close to the true values. The average estimates of the basis function coefficients are $\widehat{\boldsymbol{\eta}_1} = (4.33, 0.87, -1.94, 1.39, 1.43)^{\mathrm{T}}$ and $\widehat{\boldsymbol{\eta}_2} = (1.68, 0.078, -0.46, 1.19, 0.52)^{\mathrm{T}}$. Based on $\widehat{\boldsymbol{\eta}_1}$ and $\widehat{\boldsymbol{\eta}_2}$, the functional coefficient estimates calculated as $\widehat{\beta_1}(r) = \mathbf{b}^{\mathrm{T}}(r)\widehat{\boldsymbol{\eta}_1}$ and $\widehat{\beta_2}(r) = \mathbf{b}^{\mathrm{T}}(r)\widehat{\boldsymbol{\eta}_2}$, are illustrated in Figure 4.3.

It can be seen that the estimated functional coefficients are also close to the true functional coefficients. We also computed the standard errors of the parameter estimates based on Algorithm 4.1 as $sd\left(\widehat{\mu_b}\right)=0.028$, $sd\left(\widehat{\sigma_b}\right)=0.031$, $sd\left(\widehat{\boldsymbol{\eta}_1}\right)=\left(0.75,0.34,0.25,0.27,0.79\right)^{\mathrm{T}}$, and $sd\left(\widehat{\boldsymbol{\eta}_2}\right)=\left(3.72,1.71,1.23,1.37,3.92\right)^{\mathrm{T}}$. Moreover, the standard errors of the smoothing parameter estimates are $sd\left(\widehat{\lambda_1}\right)=2.7\times10^{-3}$ and $sd\left(\widehat{\lambda_2}\right)=3.3\times10^{-4}$. A summary of the model parameter estimates and the corresponding standard error estimates is listed in Table 4.1.

Table 4.1: Estimated model parameters and standard errors for a simulated data set

Model parameters	μ_b	η_{11}	η_{21}	η_{31}	η_{41}	η_{51}
Estimated value	0.0006	4.33	0.87	-1.94	1.39	1.43
Standard error	0.028	0.75	0.34	0.25	0.27	0.79
Model parameters	σ_b	η_{12}	η_{22}	η_{32}	η_{42}	η_{52}
Estimated value	0.972	1.68	0.078	-0.46	1.19	0.52
Standard error	0.031	3.72	1.71	1.23	1.37	3.92

To quantitatively assess the errors of the parameter estimation, we define the estimation errors as follows. For the baseline location and scale parameters, the error is defined as the Absolute Error (AE) between the true values and the mean estimates (denoted as $\widehat{\mu_b}$ and $\widehat{\sigma_b}$), i.e., $AE\left(\widehat{\mu_b}\right)=\left|\mu_b-\widehat{\mu_b}\right|$ and $AE\left(\widehat{\sigma_b}\right)=\left|\sigma_b-\widehat{\sigma_b}\right|$. For the two functional coefficients, the error is defined as the Integrated Absolute Error (IAE) between the true coefficients and the mean estimates (denoted as $\widehat{\beta_1}(r)$ and $\widehat{\beta_2}(r)$), i.e.,

$$\mathrm{IAE}\left(\widehat{\beta_i}(r)\right)=\int_0^1\left|\beta_i(r)-\widehat{\beta_i}(r)\right|dr\ ;\ i=1,2 \tag{52}$$

Based on the developed MPLE method, the parameter estimation errors, respectively denoted as $AE\left(\widehat{\mu_b}\right)$, $AE\left(\widehat{\sigma_b}\right)$, $\mathrm{IAE}\left(\widehat{\beta_1}(r)\right)$ and $\mathrm{IAE}\left(\widehat{\beta_2}(r)\right)$, for different sample sizes are computed and illustrated in Figure 4.4. It can be seen that the errors decrease to small levels as the sample size increases.

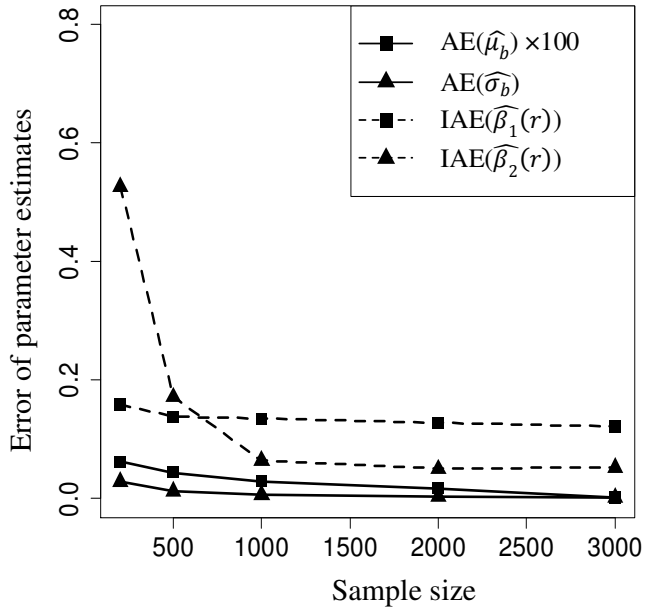

Figure 4.4: Error of parameter estimates vs. sample size

Furthermore, we investigate the effect of number of basis functions, i.e., q, on lifetime prediction. Specifically, we plot the relationship between the predicted lifetime distribution parameters (mean and standard deviation) and parameter q for a randomly chosen sample, as illustrated in Figure 4.5. It can be seen that as q increases from 5 to 10, the predicted mean and standard deviation of the lifetime almost do not vary and are very close to the true mean and standard deviation, respectively. This indicates that in our case choosing $q = 5$ is sufficient in lifetime prediction. A reason is that the true functional coefficients as specified is relatively smooth and can be well represented with 5 basis functions.

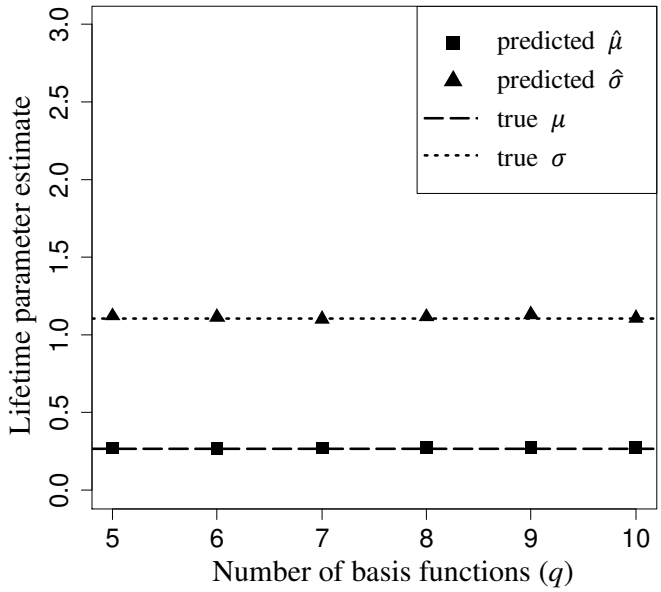

Figure 4.5: Lifetime parameter estimates vs. number of basis functions

4.6 Case Study

The proposed model is applied to studying the lifetime distribution of DP high strength steels based on their microstructure images. This family of steels is one type of advanced high strength steel developed in recent years that contains a hard martensitic phase and a ductile ferritic phase. They have been increasingly used in the automotive industry due to their excellent properties such as extremely high strength and good formability.

In the case study, we designed and conducted physical experiments on 26 material samples made from four different types of DP steels, termed as DP 780, DP 980, DP 980-GI and DP 980-CR. Each steel sample (a squared sheet of size 100 mm ×100 mm at an as-received sheet thickness of 1mm) was firmly clamped by a set of dies, and the center area of the sample was stretched axi-symmetrically by a hemispherical punch of 20 mm in diameter until the fracture occurs. Figure 4.6 shows the mechanical testing system (Instron 8801) and a failed sample of DP 980 steel that cracked, along with a microstructure image of as-received DP 980 steel. The failure process of the sample was recorded by a DIC system, which is capable of tracing surface

displacement and strain field over time. The material's fracture strain can be obtained as the DIC-measured maximum strain before failure and is used to develop material's failure criterion. Some earlier works of this technique can be seen in [122] and [123]. In this study, we treat the "maximum strain" as the "lifetime" of the materials. Next, in the image acquisition experiment the microstructure images of the steel samples were obtained by using a microscope with a 1000 × magnification after the steel samples had been prepared through sample sectioning, grinding, polishing and chemical etching. An obtained microstructure image is illustrated in Figure 4.6 (right). Based on the designed experiment, 26 lifetimes of the DP steel samples and the corresponding 26 microstructure images were collected.

Figure 4.6: Instron 8801 testing machine (left), a failed DP steel sample (middle) and a microstructure image (right)

Before applying the proposed model, a one-sample Kolmogorov-Smirnov test is performed to test the lognormal assumption of the collected lifetimes. Specifically, the null hypothesis in the test is: the 26 lifetimes are drawn from the reference distribution, i.e., the fitted log-normal with location and scale parameters being -0.874 and 0.173, respectively. The p-value of the Kolmogorov-Smirnov test is 0.353, which is greater than 0.05. Therefore, there is no sufficient evidence to reject the null hypothesis at a significance level of 0.05, and in this case study the log-normal is used as the lifetime distribution of the dual-phase advanced high strength steel.

Next, we apply the proposed model to analyze the experimental data set. Based on the MPLE method, the smoothing parameters are estimated as $\hat{\lambda}_1 = 1.04\times10^{-6}$ and $\hat{\lambda}_2 = 2.10\times10^{-6}$ using Equation (49). By solving Equation (51) the baseline location and scale parameters are, respectively, estimated as $\widehat{\mu_b} = -0.87$ and $\widehat{\sigma_b} = 0.12$. The basis function coefficients are estimated as $\widehat{\boldsymbol{\eta}_1} = (2.49, -10.31, 0.52, 11.23, 7.41)^{\mathrm{T}}$ and $\widehat{\boldsymbol{\eta}_2} = (-8.77, 3.42, 5.01, 4.30, 6.52)^{\mathrm{T}}$. Based on $\widehat{\boldsymbol{\eta}_1}$ and $\widehat{\boldsymbol{\eta}_2}$, the estimated functional coefficients $\hat{\beta}_1(r) = \mathbf{b}^{\mathrm{T}}(r)\hat{\boldsymbol{\eta}}_1$ and $\hat{\beta}_2(r) = \mathbf{b}^{\mathrm{T}}(r)\hat{\boldsymbol{\eta}}_2$ are calculated and illustrated in Figure 4.7. Furthermore, the standard errors of the parameter estimates are calculated based on Algorithm 4.1 as $sd\left(\hat{\lambda}_1\right) = 3.9\times10^{-4}$, $sd\left(\hat{\lambda}_2\right) = 5.4\times10^{-5}$, $sd\left(\widehat{\mu_b}\right) = 0.06$, $sd\left(\widehat{\sigma_b}\right) = 0.02$, $sd\left(\widehat{\boldsymbol{\eta}_1}\right) = (0.73, 3.21, 0.21, 2.20, 2.61)^{\mathrm{T}}$, $sd\left(\widehat{\boldsymbol{\eta}_2}\right) = (3.54, 1.28, 1.87, 1.76, 2.52)^{\mathrm{T}}$. A summary of the model parameter estimates and the corresponding standard error estimates is listed in Table 4.2.

Table 4.2: Estimated model parameters and standard errors for the experimental data set

Model parameters	μ_b	η_{11}	η_{21}	η_{31}	η_{41}	η_{51}
Estimated value	-0.87	2.49	-10.31	0.52	11.23	7.41
Standard error	0.06	0.73	3.21	0.21	2.20	2.61
Model parameters	σ_b	η_{12}	η_{22}	η_{32}	η_{42}	η_{52}
Estimated value	0.12	-8.77	3.42	5.01	4.30	6.52
Standard error	0.02	3.54	1.28	1.87	1.76	2.52

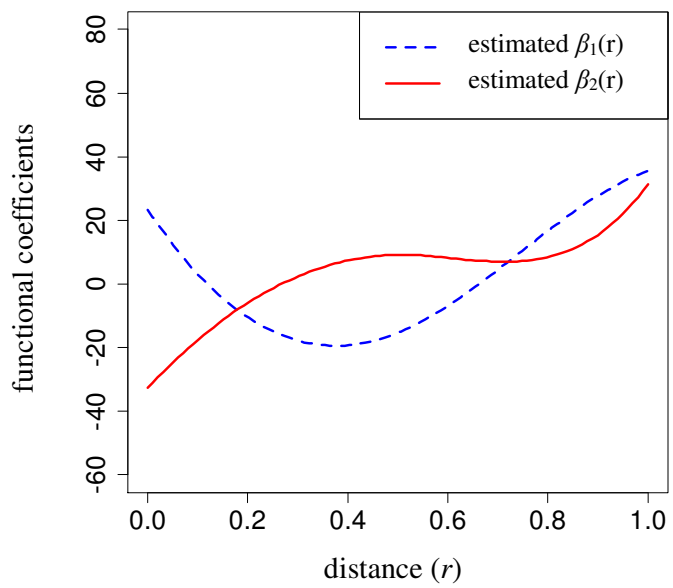

Figure 4.7: Estimated functional coefficients

Based on the estimated $\hat{\mu}_b$, $\hat{\sigma}_b$, $\hat{\beta}_1(r)$ and $\hat{\beta}_2(r)$, the material lifetime distribution can be predicted given material microstructure images following Equations (39) and (40). For example, given the microstructure image of a DP steel sample shown in Figure 4.6 (right) the predicted lifetime distribution using the proposed model is computed and illustrated by the solid curve in Figure 4.8, which is a log-normal distribution with location and scale parameters of -1.097 and 0.102, respectively.

For comparison purposes, we also predict the lifetime distribution of the DP steel sample using a classic model that ignores the microstructure image information. The dash curve in Figure 4.8 illustrates the predicted lifetime distribution of the classic model that fits a lognormal distribution to the failure time data. The location and scale parameters are -0.874 and 0.173, respectively. The vertical line illustrates the true failure time of the steel sample, which is 0.326. It can be seen that the predicted lifetime distribution is tighter and more accurate than that of the classical model, and thus performs better in failure prediction.

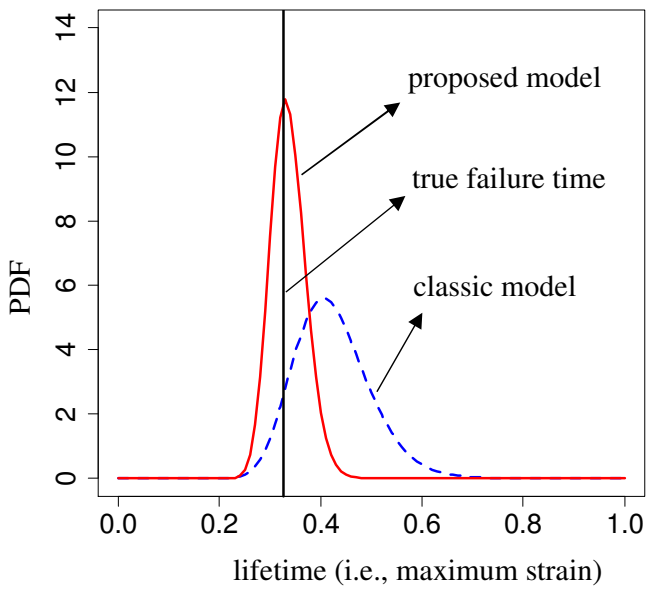

Figure 4.8: Lifetime distribution prediction for a DP steel sample

4.7 Summary

Material microstructures strongly affect material failure and reliability. In the literature, little research quantitatively conducts reliability analysis by utilizing the material microstructure image information. In this chapter, we propose a novel distribution-based functional linear model to conduct reliability analysis of dual-phase steel by utilizing its microstructure images. Specifically, the steel's lifetime distribution is predicted based on its microstructure images, in which both the location and scale parameters of the distribution are adjusted by the steel's two-point correlation function that captures the statistical properties of the microstructure.

The proposed model is a generalization of the conventional functional linear regression model that treats the scale parameter as a constant. In the proposed model, both the location and scale parameters of a scalar response are adjusted by a functional predictor. Thus, the conventional parameter estimation method for functional linear regression such as the

penalized least squares method cannot be directly applied. To overcome the challenge, we develop a maximum penalized likelihood estimation method. A simulation study is implemented to verify the developed methods. Physical experiments are designed and conducted to illustrate the proposed model.

In this chapter, we directly link the microstructure image information to the lifetime of dual-phase steel. In the future, it would be interesting to link the microstructure information to material macroscopic properties, which often affect the failure of materials. Moreover, the functional linear regression is applied to modeling the dependency structure between the two-point correlation function and the lifetime distribution parameters. In the future, to apply functional nonlinear regression is an interesting research topic. Moreover, another appealing research topic would be to incorporate the three-dimensional material microstructure information into reliability analysis rather than using the two-dimensional microstructure images.

The methodologies proposed in this chapter has been published in journal article [74].

CHAPTER 5. GENERAL CONCLUSIONS

Material physical properties strongly affect material degradation behavior and failure. Without considering those properties, material reliability analysis utilizing existing methodologies may be inaccurate and is sometimes significantly biased. In this dissertation, we focus on incorporating three material properties of various scales into steel reliability analysis, i.e., a macro-scale steel overload retardation property, a local-scale steel dynamic deformation property and a micro-scale steel microstructure property. Although steel is utilized as the type of material in this dissertation, the proposed methodologies may also be applicable to other materials.

In CHAPTER 2, we propose reliability analysis by incorporating the macro-scale overload retardation property. Specifically, a physical – statistical model is developed to quantitatively describe the overload retardation effect. The model is build up based on a modification of the existing Paris law used in the physical domain to delineate the physical mechanism of overload retardation. Random measurement errors are considered in the time domain. Based on the proposed model, reliability analysis is developed by defining a criterion that failure occurs when the crack length reaches a certain threshold level. A maximum likelihood method is developed to estimate the model parameters given observed crack propagation paths. A likelihood ratio hypothesis test is developed to determine whether a material has an overload retardation effect. The developed methodologies are verified and demonstrated through designed physical experiments. The methods are also applicable to overload acceleration and overload stationary situations, while only minor changes need to be made.

In CHAPTER 3, we conduct reliability analysis by utilizing the local-scale dynamic

material deformation information in a tensile process. Specifically, a new multivariate general path model is proposed to quantitatively describe the multiple deformation paths collected across a grid of local points on each material sample. The model generalizes the existing univariate general path model that considers a single path per sample. A two-stage method is developed to estimate the model parameters while overcoming the computational complexities. A new variance-based failure criterion is used to account for the failure mechanism. Based on the proposed model and the new failure criterion, reliability analyses are developed for various types of deformation paths. In particular, closed-form reliability functions are derived when the multiple deformation paths follow a multivariate linear law, a multivariate power law, or a multivariate exponential law. When the deformation paths are more general, a simulation-based algorithm to compute the reliability function is developed. The aforementioned methods are illustrated using both simulation studies and designed physical experiments on advanced high strength steel.

In CHAPTER 4, we develop reliability analysis by considering material microstructure image information using a two-stage framework. In Stage 1, the two-point correlation functions of material microstructure images are calculated to extract statistical information of the images up to the second order. In Stage 2, a novel distribution-based functional linear model is proposed to predict the lifetime distribution of materials based on the two-point correlation functions. In the model, both the location and scale parameters of the lifetime distribution are adjusted by the two-point correlation functions. The proposed distribution-based functional linear model is a generalization of the conventional functional linear regression model that treats the scale parameter as a constant. A maximum penalized likelihood estimation method is

developed to estimate the model parameters, which can overcome the overfitting issue. A simulation study is implemented to verify the developed methods. Physical experiments on advanced high strength steel are designed and conducted to demonstrate the proposed model. Results reveal that a significant improvement is achieved on the accuracy of lifetime prediction by utilizing steel microstructure image information.

APPENDIX 1. Proof of Proposition 1

For any $x_0 \in \mathbb{R}$, let $m_1 = k_2 x_0 + b_2$ and $m_2 = k_3 x_0 + b_3$. For $m_1,\ m_2 \in \mathbb{R}$, the following identity holds [124].

$$\max\{m_1, m_2\} = \lim_{p\to\infty} \delta^* \left\{ \left(\frac{M^* + m_1}{\delta^*} \right)^p + \left(\frac{M^* + m_2}{\delta^*} \right)^p \right\}^{\frac{1}{p}} - M^* \tag{53}$$

where $M^* = M(x_0)$ is a large positive number and keeps $M^* + m_i$ positive for $i = 1, 2$; $\delta^* = \delta(x_0)$.

A similar identity of (53) with respect to $\min\{m_1, m_2\}$ can be constructed based on the following relationship.

$$\min\{m_1, m_2\} = -\max\{-m_1, -m_2\} \tag{54}$$

Let $m_3 = k_1 x_0 + b_1 \in \mathbb{R}^1$. Based on (53) and (54), we obtain the following identity.

$$\min\{\max\{m_1, m_2\}, m_3\} = \lim_{q\to\infty} -\omega^* \left\{ \left(\frac{B^* - \max\{m_1, m_2\}}{\omega^*} \right)^q + \left(\frac{B^* - m_3}{\omega^*} \right)^q \right\}^{\frac{1}{q}} + B^* \tag{55}$$

where $\max\{m_1, m_2\}$ is shown in (53); $B^* = B(x_0)$ keeps $B^* - m_i$ positive for $i = 1, 2, 3$; and $\omega^* = \omega(x_0)$ is used to ensure $0 \le \frac{B^* - \max\{m_1, m_2\}}{\omega^*} \le 1$ and $0 \le \frac{B^* - m_3}{\omega^*} \le 1$.

Equation (55) is equivalent to $g_1(x_0) = \lim_{p,q\to+\infty} g_2(x_0; p, q)$. So, we conclude that for $x \in \mathbb{R}$ the following identity holds.

$$g_1(x) = \lim_{p,q\to+\infty} g_2(x; p, q) \tag{56}$$

Proposition 1 is proved.

APPENDIX 2. Proof of Proposition 2

When finite values of p and q are selected (p>1 and q>1) for applying Proposition 1, based on Equations (53) and (55) the point-wise approximation error is as follows.

$$\xi = -\omega^* \left\{ \left(\frac{B^* - \lambda}{\omega^*} \right)^q + \left(\frac{B^* - m_3}{\omega^*} \right)^q \right\}^{\frac{1}{q}} + B^* - \min\left\{ \max\left\{ m_1, m_2 \right\}, m_3 \right\} \tag{57}$$

where $\lambda = \delta^* \left\{ \left(\frac{M^* + m_1}{\delta^*} \right)^p + \left(\frac{M^* + m_2}{\delta^*} \right)^p \right\}^{\frac{1}{p}} - M^*$, and λ satisfies the following inequalites.

$$\begin{cases} \lambda > \delta^* \left\{ \left(\frac{M^* + m_1}{\delta^*} \right)^p + 0^p \right\}^{\frac{1}{p}} - M^* = m_1 \\ \lambda > \delta^* \left\{ 0^p + \left(\frac{M^* + m_2}{\delta^*} \right)^p \right\}^{\frac{1}{p}} - M^* = m_2 \end{cases} \tag{58}$$

To derive the bounds for ξ, we first define two variables denoted as ξ_1 and ξ_2. Then, the bounds of ξ_1 and ξ_2 are calculated in Lemma 1 and Lemma 2. Finally, the bounds for ξ are derived based on the bounds of ξ_1 and ξ_2.

Lemma 1. Define $\xi_1 = \lambda - \max\left\{ m_1, m_2 \right\}$, the upper and lower bounds of ξ_1 are

$$0 < \xi_1 \le \frac{c_1}{p} \tag{59}$$

where $c_1 = 2\log 2 \times \left(M^* + \max\left\{ m_1, m_2 \right\} \right)$ is a positive constant.

Proof of Lemma 1. From equation (58), it can be seen that $\lambda > \max\left\{ m_1, m_2 \right\}$. Hence, $\xi_1 > 0$. Furthermore, ξ_1 can be written as:

$$\xi_1 = \delta^* \left\{ \left(\frac{M^* + m_1}{\delta^*} \right)^p + \left(\frac{M^* + m_2}{\delta^*} \right)^p \right\}^{\frac{1}{p}} - \delta^* \max\left\{ \frac{M^* + m_1}{\delta^*}, \frac{M^* + m_2}{\delta^*} \right\} \tag{60}$$

To derive the bounds for ξ_1, we start with defining a function $\varphi(x)=\log(x), x\in\mathbb{R}^+$. $\varphi(x)$ satisfies the following inequality.

$$x_2 - x_1 < \frac{\varphi(x_2)-\varphi(x_1)}{\varphi'(x_2)} \tag{61}$$

where x_1 and x_2 are two real numbers satisfying $0<x_1<x_2$. In (61), let $x_1=\delta^*\max\left\{\frac{M^*+m_1}{\delta^*},\frac{M^*+m_2}{\delta^*}\right\}$ and $x_2=\lambda=\delta^*\left\{\left(\frac{M^*+m_1}{\delta^*}\right)^p+\left(\frac{M^*+m_2}{\delta^*}\right)^p\right\}^{\frac{1}{p}}$, the following inequality is obtained.

$$\begin{aligned}\xi_1 &< x_2\left\{\frac{1}{p}\log\left\{\left(\frac{M^*+m_1}{\delta^*}\right)^p+\left(\frac{M^*+m_2}{\delta^*}\right)^p\right\}-\log\left\{\max\left\{\frac{M^*+m_1}{\delta^*},\frac{M^*+m_2}{\delta^*}\right\}\right\}\right\}\\ &< \frac{x_2}{p}\log\frac{\left(\frac{M^*+m_1}{\delta^*}\right)^p+\left(\frac{M^*+m_2}{\delta^*}\right)^p}{\left\{\max\left\{\frac{M^*+m_1}{\delta^*},\frac{M^*+m_2}{\delta^*}\right\}\right\}^p}\le\frac{x_2}{p}\log 2.\end{aligned} \tag{62}$$

where x_2 satisfies $x_2\le\delta^*\left\{2\times\left(\frac{M^*+\max\{m_1,m_2\}}{\delta^*}\right)^p\right\}^{\frac{1}{p}}=2^{\frac{1}{p}}\left(M^*+\max\{m_1,m_2\}\right)$.

Considering p>1, we have $2^{\frac{1}{p}}<2$, and thus we get $x_2<2\left(M^*+\max\{m_1,m_2\}\right)$. By inserting this inequality into (62), we obtain the upper and lower bounds of ξ_1 in (59).

Lemma 2. Define

$$\xi_2=-\omega^*\left\{\left(\frac{B^*-\lambda}{\omega^*}\right)^q+\left(\frac{B^*-m_3}{\omega^*}\right)^q\right\}^{\frac{1}{q}}+B^*-\min\{\lambda,m_3\} \tag{63}$$

The upper and lower bounds of ξ_2 are

$$-\frac{c_2}{q}\le\xi_2<0 \tag{64}$$

Proof of Lemma 2. In (63), considering

$\min\{\lambda, m_3\} = -\max\{-\lambda, -m_3\} = -\omega^* \max\left\{\frac{B^* - \lambda}{\omega^*}, \frac{B^* - m_3}{\omega^*}\right\} + B^*$, ξ_2 can be further written as:

$$\xi_2 = -\left\{\omega^* \left\{\left(\frac{B^* - \lambda}{\omega^*}\right)^q + \left(\frac{B^* - m_3}{\omega^*}\right)^q\right\}^{\frac{1}{q}} - \omega^* \max\left\{\frac{B^* - \lambda}{\omega^*}, \frac{B^* - m_3}{\omega^*}\right\}\right\} \tag{65}$$

The bounds for ξ_2 can be obtained due to the symmetry between Equations (65) and (60), i.e., $-\frac{c_2^*}{q} \le \xi_2 < 0$, where $c_2^* = 2\log 2 \times \left(B^* + \max\{-\lambda, -m_3\}\right)$. Considering $\lambda > \max\{m_1, m_2\}$, we get $c_2^* \le 2\log 2 \times \left(B^* + \max\{-\max(m_1, m_2), -m_3\}\right) = c_2$, and c_2 is a positive constant. Therefore, the bounds for ξ_2 is obatained in (64).

Based on Lemma 1 and Lemma 2, the bounds for ξ is derived as follows.

Considering $\xi_1 > 0$, the following inequality holds.

$$\min\{\max\{m_1, m_2\}, m_3\} \le \min\{\max\{m_1, m_2\} + \xi_1, m_3\} \le \min\{\max\{m_1, m_2\} + \xi_1, m_3 + \xi_1\}.$$

Based on the aformationed inequality, it can be seen that:

$$\begin{aligned} &\min\{\max\{m_1, m_2\} + \xi_1, m_3\} - \min\{\max\{m_1, m_2\}, m_3\} \\ &\le \min\{\max\{m_1, m_2\} + \xi_1, m_3 + \xi_1\} - \min\{\max\{m_1, m_2\}, m_3\} = \xi_1 \end{aligned} \tag{66}$$

By substituting $\max\{m_1, m_2\} + \xi_1 = \lambda$ into (66), the following inequality is obtained.

$$0 \le \min\{\lambda, m_3\} - \min\{\max\{m_1, m_2\}, m_3\} \le \xi_1 \tag{67}$$

Then, by inserting (63) into (67) we obtain:

$$0 \le -\omega^* \left\{\left(\frac{B^* - \lambda}{\omega^*}\right)^q + \left(\frac{B^* - m_3}{\omega^*}\right)^q\right\}^{\frac{1}{q}} + B^* - \xi_2 - \min\{\max\{m_1, m_2\}, m_3\} \le \xi_1$$

Considering the definition of ξ in (57), the aforementioned inequality is equivalent to

$\xi_2 \le \xi \le \xi_1 + \xi_2$. Next, based on (59) and (64) the upper and lower bounds for ξ is obtained as follows.

$$-\frac{c_2}{q} \le \xi \le \frac{c_1}{p} - \frac{c_2}{q} \tag{68}$$

Finally, considering the definition of variabes $m_1, m_2, m_3, M^*, \delta^*, B^*, \omega^*$ in Proposition 1, the upper and lower bounds of approximation error for any given $x \in \mathbb{R}$ are as follows.

$$-\frac{c_2(x)}{q} \le \xi(x) \le \frac{c_1(x)}{p} - \frac{c_2(x)}{q} \tag{69}$$

where $c_1(x) = 2\log 2 \times \left(M^*(x) + \max\{k_2 x + b_2, k_3 x + b_3\}\right)$ and

$c_2(x) = 2\log 2 \times \left(B^*(x) + \max\{-\max\{k_2 x + b_2, k_3 x + b_3\}, -k_1 x - b_1\}\right)$.

Proposition 2 is proved.

APPENDIX 3. Asymptotic Analysis of the Two-stage Parameter Estimation Method

Statistical and asymptotic properties of the two-stage procedure in Algorithm 3.1 are provided, which are similar to the results in Lu and Meeker [7]. Specifically, under mild conditions [7, 125] $\widehat{\boldsymbol{\psi}}_i$, $\widehat{\boldsymbol{\Phi}}_i$ and $\hat{\sigma}_i$ are consistent, and $\left(\widehat{\boldsymbol{\psi}}_i, \widehat{\boldsymbol{\Phi}}_i\right)$ and $\hat{\sigma}_i$ are asymptotically independent. For large m_i, the following asymptotic result holds conditional on $\boldsymbol{\Phi}_i = \boldsymbol{\Phi}_i^*$:

$$\begin{pmatrix} \widehat{\boldsymbol{\psi}}_i \\ \widehat{\boldsymbol{\Phi}}_i \end{pmatrix} \sim MVN\left(\begin{pmatrix} \boldsymbol{\psi} \\ \boldsymbol{\Phi}_i^* \end{pmatrix}, \sigma^2\left[\dot{\boldsymbol{\eta}}^{\mathrm{T}}\left(\mathbf{t}_i;\boldsymbol{\psi},\boldsymbol{\Phi}_i^*\right)\dot{\boldsymbol{\eta}}\left(\mathbf{t}_i;\boldsymbol{\psi},\boldsymbol{\Phi}_i^*\right)\right]^{-1}\right) \tag{70}$$

Based on (70), the unconditional asymptotic expectation and covariance matrix of $\widehat{\boldsymbol{\Phi}}_i$ are

$$E_{\boldsymbol{\Phi}}\left(\widehat{\boldsymbol{\Phi}}_i\right) = E_{\boldsymbol{\Phi}}\left[E_{\varepsilon}\left(\widehat{\boldsymbol{\Phi}}_i \middle| \boldsymbol{\Phi}_i\right)\right] = E_{\boldsymbol{\Phi}}\left[\boldsymbol{\Phi}_i\right] = \boldsymbol{\mu}_{\boldsymbol{\Phi}} \tag{71}$$

and

$$\begin{aligned} \mathrm{Var}_{\boldsymbol{\Phi}}\left(\widehat{\boldsymbol{\Phi}}_i\right) &= \mathrm{Var}_{\boldsymbol{\Phi}}\left[E_{\varepsilon}\left(\widehat{\boldsymbol{\Phi}}_i \middle| \boldsymbol{\Phi}_i\right)\right] + E_{\boldsymbol{\Phi}}\left[\mathrm{Var}_{\varepsilon}\left(\widehat{\boldsymbol{\Phi}}_i \middle| \boldsymbol{\Phi}_i\right)\right] \\ &= \mathrm{Var}_{\boldsymbol{\Phi}}\left[\boldsymbol{\Phi}_i\right] + E_{\boldsymbol{\Phi}}\left[\mathrm{Var}_{\varepsilon}\left(\widehat{\boldsymbol{\Phi}}_i \middle| \boldsymbol{\Phi}_i\right)\right] = \boldsymbol{\Sigma}_{\boldsymbol{\Phi}} + \boldsymbol{\Sigma}_{\widehat{\boldsymbol{\Phi}}} \end{aligned} \tag{72}$$

where $\boldsymbol{\Sigma}_{\widehat{\boldsymbol{\Phi}}} = E_{\boldsymbol{\Phi}}\left[\mathrm{Var}_{\varepsilon}\left(\widehat{\boldsymbol{\Phi}}_i \middle| \boldsymbol{\Phi}_i\right)\right]$ is the asymptotic variability due to measurement errors on deformation paths of the ith sample.

Moreover, for the fixed-effect parameter estimator $\widehat{\boldsymbol{\psi}}_i$, the following asymptotic result holds:

$$E_{\boldsymbol{\Phi}}\left(\widehat{\boldsymbol{\psi}}_i\right) = E_{\boldsymbol{\Phi}}\left[E_{\varepsilon}\left(\widehat{\boldsymbol{\psi}}_i \middle| \boldsymbol{\Phi}_i\right)\right] = E_{\boldsymbol{\Phi}}\left[\boldsymbol{\psi}\right] = \boldsymbol{\psi} \tag{73}$$

Based on (71) − (73), we have the following asymptotic result for large m_i:

$$\boldsymbol{\Sigma}_{\boldsymbol{\Phi}} = E_{\boldsymbol{\Phi}}\left[\frac{1}{N-1}\sum_{i=1}^{N}\left(\widehat{\boldsymbol{\Phi}}_i - \hat{\boldsymbol{\mu}}_{\boldsymbol{\Phi}}\right)\left(\widehat{\boldsymbol{\Phi}}_i - \hat{\boldsymbol{\mu}}_{\boldsymbol{\Phi}}\right)^{\mathrm{T}}\right] - \boldsymbol{\Sigma}_{\widehat{\boldsymbol{\Phi}}} \tag{74}$$

As $\boldsymbol{\Sigma}_{\widehat{\boldsymbol{\Phi}}}$ in Equation (74) can be estimated as $\hat{\boldsymbol{\Sigma}}_{\widehat{\boldsymbol{\Phi}}} = \frac{1}{N}\sum_{i=1}^{N}\mathrm{var}_{\varepsilon}\left(\widehat{\boldsymbol{\Phi}}_i\right)$, the result in Equation (22) is obtained.

APPENDIX 4. Proof of Proposition 3

Define $\mathbf{Z}_t = \mathbf{X}_t - \boldsymbol{\upsilon}_t$. $\boldsymbol{\upsilon}_t$ can be written as $\boldsymbol{\upsilon}_t = \mathbf{1}_{p\times p}\mathbf{X}_t / p$, where $\mathbf{1}_{p\times p}$ is a $p \times p$ dimensional matrix with all entries equaling 1. Therefore, $\mathbf{Z}_t$ can be shown to be multivariate normal as follows.

$$\mathbf{Z}_t = \mathbf{X}_t - \boldsymbol{\upsilon}_t = \left(\mathbf{I}_{p\times p} - \mathbf{1}_{p\times p}/p\right)\mathbf{X}_t = \mathbf{L}\mathbf{X}_t \sim N\left(\boldsymbol{\mu}_t, \boldsymbol{\Sigma}_t\right) \tag{75}$$

where $\mathbf{L} = \mathbf{I}_{p\times p} - \mathbf{1}_{p\times p}/p$ and $\boldsymbol{\mu}_t = \mathbf{L}\left(t\boldsymbol{\mu}_{\mathbf{a}} + \boldsymbol{\mu}_{\mathbf{b}}\right)$. In (75), as $Cov\left(\mathbf{X}_t\right) = t^2\boldsymbol{\Sigma}_{\mathbf{a}} + \boldsymbol{\Sigma}_{\mathbf{b}} + t\left(\boldsymbol{\Sigma}_{\mathbf{ab}} + \boldsymbol{\Sigma}_{\mathbf{ba}}\right)$, we can obtain $\boldsymbol{\Sigma}_t = \mathbf{L}Cov\left(\mathbf{X}_t\right)\mathbf{L}^{\mathrm{T}} = \mathbf{L}\left[t^2\boldsymbol{\Sigma}_{\mathbf{a}} + \boldsymbol{\Sigma}_{\mathbf{b}} + t\left(\boldsymbol{\Sigma}_{\mathbf{ab}} + \boldsymbol{\Sigma}_{\mathbf{ba}}\right)\right]\mathbf{L}^{\mathrm{T}}$.

Based on (75), define $\mathbf{W}_t = \boldsymbol{\Sigma}_t^{-1/2}\left(\mathbf{Z}_t - \boldsymbol{\mu}_t\right)$ by assuming that $\boldsymbol{\Sigma}_t$ is invertible. $\mathbf{W}_t$ follows a standard multivariate normal distribution, i.e., $E\left(\mathbf{W}_t\right) = \mathbf{0}_p$ and $Cov\left(\mathbf{W}_t\right) = \mathbf{I}_{p\times p}$, where $\mathbf{0}_p$ is a p-dimensional zero vector, and $\mathbf{I}_{p\times p}$ is a $p \times p$ dimensional identity matrix.

Based on the definition of $\mathbf{Z}_t$ and $\mathbf{W}_t$, the real-time variance defined in Equation (24) can be written as $S_t = \mathbf{Z}_t^{\mathrm{T}}\mathbf{Z}_t / (p-1)$. Furthermore, by replacing $\mathbf{Z}_t$ with $\mathbf{W}_t$, S_t can be derived as

$$\begin{aligned} S_t &= \frac{1}{p-1}\left(\boldsymbol{\Sigma}_t^{1/2}\left(\mathbf{W}_t + \boldsymbol{\Sigma}_t^{-1/2}\boldsymbol{\mu}_t\right)\right)^{\mathrm{T}}\boldsymbol{\Sigma}_t^{1/2}\left(\mathbf{W}_t + \boldsymbol{\Sigma}_t^{-1/2}\boldsymbol{\mu}_t\right) \\ &= \frac{1}{p-1}\left(\mathbf{W}_t + \boldsymbol{\Sigma}_t^{-1/2}\boldsymbol{\mu}_t\right)^{\mathrm{T}}\boldsymbol{\Sigma}_t^{1/2}\boldsymbol{\Sigma}_t^{1/2}\left(\mathbf{W}_t + \boldsymbol{\Sigma}_t^{-1/2}\boldsymbol{\mu}_t\right) \\ &= \frac{1}{p-1}\left(\mathbf{W}_t + \boldsymbol{\Sigma}_t^{-1/2}\boldsymbol{\mu}_t\right)^{\mathrm{T}}\boldsymbol{\Sigma}_t\left(\mathbf{W}_t + \boldsymbol{\Sigma}_t^{-1/2}\boldsymbol{\mu}_t\right) \end{aligned} \tag{76}$$

Equation (76) involves the covariance matrix $\boldsymbol{\Sigma}_t$. Based on the spectral decomposition theorem [126], there exists an orthogonal matrix $\mathbf{Q} = \left(\mathbf{q}_1, \mathbf{q}_2, ..., \mathbf{q}_p\right)$ such that for the symmetric $\boldsymbol{\Sigma}_t$ the following result holds:

$$\mathbf{Q}^{\mathrm{T}}\boldsymbol{\Sigma}_t\mathbf{Q} = \boldsymbol{\Lambda}_t = \mathrm{diag}\left(\lambda_{1t}, \lambda_{2t}, ..., \lambda_{pt}\right) \tag{77}$$

where $\mathbf{Q}$ is $p \times p$ dimensional and satisfies $\mathbf{Q}^{\mathrm{T}}\mathbf{Q} = \mathbf{Q}\mathbf{Q}^{\mathrm{T}} = \mathbf{I}_{p\times p}$; $\lambda_{1t} \geq \lambda_{2t} \geq \ldots \geq \lambda_{pt}$ are the eigenvalues of $\mathbf{\Sigma}_t$; and $\mathbf{q}_i$ is the eigenvector corresponding to eigenvalue λ_{it}.

Based on (77), $\mathbf{\Sigma}_t$ can be decomposed as

$$\mathbf{\Sigma}_t = \left(\mathbf{Q}^{\mathrm{T}}\right)^{-1}\left(\mathbf{Q}^{\mathrm{T}}\mathbf{\Sigma}_t\mathbf{Q}\right)\mathbf{Q}^{-1} = \left(\mathbf{Q}^{\mathrm{T}}\right)^{-1}\mathbf{\Lambda}_t\mathbf{Q}^{-1} = \mathbf{Q}\mathbf{\Lambda}_t\mathbf{Q}^{\mathrm{T}} \tag{78}$$

By inserting Equation (78) into Equation (76), S_t can be derived as

$$\begin{aligned} S_t &= \frac{1}{p-1}\left(\mathbf{W}_t + \mathbf{\Sigma}_t^{-1/2}\boldsymbol{\mu}_t\right)^{\mathrm{T}}\mathbf{Q}\mathbf{\Lambda}_t\mathbf{Q}^{\mathrm{T}}\left(\mathbf{W}_t + \mathbf{\Sigma}_t^{-1/2}\boldsymbol{\mu}_t\right) \\ &= \frac{1}{p-1}\left(\mathbf{Q}^{\mathrm{T}}\mathbf{W}_t + \mathbf{Q}^{\mathrm{T}}\mathbf{\Sigma}_t^{-1/2}\boldsymbol{\mu}_t\right)^{\mathrm{T}}\mathbf{\Lambda}_t\left(\mathbf{Q}^{\mathrm{T}}\mathbf{W}_t + \mathbf{Q}^{\mathrm{T}}\mathbf{\Sigma}_t^{-1/2}\boldsymbol{\mu}_t\right) \\ &= \frac{1}{p-1}\left(\mathbf{D}_t + \mathbf{c}_t\right)^{\mathrm{T}}\mathbf{\Lambda}_t\left(\mathbf{D}_t + \mathbf{c}_t\right) \\ &= \frac{1}{p-1}\sum_{i=1}^{p}\lambda_{it}\left(D_{it} + c_{it}\right)^2 \\ &= \frac{1}{p-1}\sum_{i=1}^{p}\lambda_{it}\Omega_{it} \end{aligned} \tag{79}$$

where $\Omega_{it} = \left(D_{it} + c_{it}\right)^2$ is a non-central chi-squared random variable with one degree of freedom, i.e., $\Omega_{it} \sim \chi_1^2\left(c_{it}^2\right)$; c_{it}^2 is the non-centrality parameter; $\mathbf{D}_t = \mathbf{Q}^{\mathrm{T}}\mathbf{W}_t = \left(D_{1t}, D_{2t}, \ldots, D_{pt}\right)^{\mathrm{T}}$ satisfies $E\left(\mathbf{D}_t\right) = \mathbf{0}$ and $Cov\left(\mathbf{D}_t\right) = \mathbf{Q}^{\mathrm{T}}Cov\left(\mathbf{W}_t\right)\mathbf{Q} = \mathbf{Q}^{\mathrm{T}}\mathbf{Q} = \mathbf{I}_{p\times p}$; and $\mathbf{c}_t = \mathbf{Q}^{\mathrm{T}}\mathbf{\Sigma}_t^{-1/2}\boldsymbol{\mu}_t = \left(c_{1t}, c_{2t}, \ldots, c_{pt}\right)^{\mathrm{T}}$.

Proposition 3 is proved.

APPENDIX 5. Proof of Proposition 4

When the threshold variance is specified as s_{th}, the reliability function is

$$R\left(t;s_{th},\Theta\right)=\Pr\left(S_t\le s_{th};\Theta\right)=F_{S_t}\left(s_{th};\Theta\right) \tag{80}$$

Martínez and Blázquez [85] derived the CDF of $Y=\sum_{i=1}^{n}\alpha_i X_i$, where $X_i\sim\chi^2_{v_i}\left(\delta_i\right)$ and α_i for i = 1, 2, …, n are coefficients, as follows:

$$F_Y\left(y\right)=\frac{y^{v/2}e^{-\frac{y}{2\beta}}}{\left(2\beta\right)^{v/2+1}\Gamma\left(v/2+1\right)}\sum_{i=0}^{+\infty}\frac{i!m_i}{\left(v/2+1\right)_i}\times L_i^{(v/2)}\left(\frac{\left(v+2\right)y}{4\beta\mu_0}\right) \tag{81}$$

where $v=\sum_{i=1}^{n}v_i$; $L_i^{(\alpha)}\left(x\right)$ is defined in Equation (27);

$m_0=2\left(\frac{v}{2}+1\right)^{v/2+1}\exp\left\{-\frac{1}{2}\sum_{i=1}^{n}\frac{\delta_i\alpha_i\left(q-\mu_0\right)}{\beta\mu_0+\alpha_i\left(q-\mu_0\right)}\right\}\times\frac{\beta^{v/2+1}}{q-\mu_0}\prod_{i=1}^{n}\left(\beta\mu_0+\alpha_i\left(q-\mu_0\right)\right)^{-v_i/2}$;

$m_k=\frac{1}{k}\sum_{j=0}^{k-1}m_j d_{k-j}, k\ge 1$; $q=v/2+1$; $\mu_0>0$; $\beta>0$; and

$d_j=-\frac{j\beta q}{2\mu_0}\sum_{i=1}^{n}\delta_i\alpha_i\left(\beta-\alpha_i\right)^{j-1}\left(\frac{\mu_0}{\beta\mu_0+\alpha_i\left(q-\mu_0\right)}\right)^{j+1}+\left(\frac{-\mu_0}{q-\mu_0}\right)^{j}+\sum_{i=1}^{n}\frac{v_i}{2}\left(\frac{\mu_0\left(\beta-\alpha_i\right)}{\beta\mu_0+\alpha_i\left(q-\mu_0\right)}\right)^{j}$

for $j\ge 1$.

Based on Equation (80), by truncating Equation (81) using its first M items and inserting $Y=S_t$, $\alpha_i=\lambda_{it}/\left(p-1\right)$, $n=p$, $v_i=1$, $v=\sum_{i=1}^{p}v_i=p$, $x=s_{th}$ and $\delta_i=c_{it}^2$ into Equation (81), the approximate reliability function in Equation (27) is obtained.

Proposition 4 is proved.

APPENDIX 6. Proof of Proposition 5

In Proposition 4, by truncating Equation (81) using its first M items, Martínez and Blázquez [85] derived the bound of the truncation error $\xi(y)$ as

$$\xi(y) \le \frac{y^{v/2} e^{-\frac{y}{2\beta}}}{\Gamma(v/2+1)} \prod_{i=1}^{n} \left| 1 + \frac{\alpha_i}{\beta}(q/\mu_0 - 1) \right|^{-v_i/2} \times \frac{q}{|q-\mu_0|} \times \exp\left(\frac{\mu_0 \delta}{2q\varepsilon} \right) \times$$
$$\exp\left\{ -\frac{1}{4} \sum_{i=1}^{n} \frac{\delta_i (\alpha_i/\beta)(q/\mu_0 - 1)}{1 + (\alpha_i/\beta)(q/\mu_0 - 1)} \right\} \times \left(\frac{q}{2\beta\mu_0} \right)^{v/2} \exp\left(\frac{(v+2)\, y}{8\beta\mu_0} \right) \sum_{k=M+1}^{+\infty} b_k \tag{82}$$

where $b_k = \varepsilon^k \left(\frac{2k+v+2}{2k} \right)^k \left(\frac{2k+v+2}{v+2} \right)^{v/2+1}$; $\varepsilon = \max(\xi_1, \xi_2)$; $\xi_1 = \left| \frac{\mu_0}{(v/2+1) - \mu_0} \right|$; and $\xi_2 = \max_i \left\{ \left| \frac{1 - \alpha_i/\beta}{1 + (\alpha_i/\beta)((v/2+1)/\mu_0 - 1)} \right| \right\}$.

In our problem, the truncation error for the reliability function in Proposition 4 can be written as

$$e(t; s_{th}, \Theta) = \left| R(t; s_{th}, \Theta) - \widetilde{R}(t; s_{th}, \Theta) \right| = \xi(s_{th}) \tag{83}$$

Further, by inserting $Y = S_t$, $\alpha_i = \lambda_{it}/(p-1)$, $n = p$, $v_i = 1$, $v = \sum_{i=1}^{p} v_i = p$, $x = s_{th}$ and $\delta_i = c_{it}^2$ into Equation (83), the truncation error bound in Proposition 5 is obtained.

Proposition 5 is proved.

APPENDIX 7. Proof of Corollary 1

When the p degradation paths are statistically independent, it is assumed that $(a_i, b_i)^{\mathrm{T}} \sim N\left((\mu_a, \mu_b)^{\mathrm{T}}, \mathbf{\Sigma}\right)$ and $\varepsilon_{it} \sim N\left(0, \sigma^2\right)$ for $i = 1, 2, \ldots, p$, where $\mathbf{\Sigma} = \begin{pmatrix} \Sigma_{11} & \Sigma_{12} \\ \Sigma_{21} & \Sigma_{22} \end{pmatrix}$. In Proposition 3, the orthogonal matrix $\mathbf{Q}$ degenerates to $\mathbf{I}_{p\times p}$, and $\lambda_{1t} = \lambda_{2t} = \ldots = \lambda_{pt} = \sigma_t^2$, where $\sigma_t^2 = t^2\Sigma_{11} + \Sigma_{22} + 2t\Sigma_{12}$. Furthermore, in Proposition 3 $c_{it} = \left(\sigma_t^2\right)^{-1/2} \times \mu_t = \mu_t / \sigma_t$, where $\mu_t = \mu_a t + \mu_b$. By inserting the λ_{it}'s and c_{it}'s into Proposition 3, the real-time variance is obtained as

$$S_t^* = \frac{\sigma_t^2}{p-1} \sum_{i=1}^{p} \left(D_{it} + \mu_t / \sigma_t\right)^2 = \frac{\sigma_t^2}{p-1} \Omega_t^* \tag{84}$$

where $\Omega_t^* = \sum_{i=1}^{p} \left(D_{it} + \mu_t / \sigma_t\right)^2 \sim \chi_p^2\left(p\mu_t^2 / \sigma_t^2\right)$.

Corollary 1 is proved.

APPENDIX 8. Proof of Corollary 2

In Corollary 1, let $Z^* = \sum_{i=1}^{p} \left(D_{it} + \mu_t / \sigma_t \right)^2 \sim \chi_p^2 \left(\lambda \right)$, where $\lambda = p\mu_t^2 / \sigma_t^2$. The CDF of Z^* is as follows [127]:

$$F_{Z^*}\left(z^*\right) = 1 - Q_{p/2}\left(\sqrt{\lambda}, \sqrt{z^*}\right) \tag{85}$$

where $Q_M\left(a,b\right)$ is the Marcum Q-function defined in Equation (30).

Based on Equations (29) and (85), the CDF of S_t^* can be derived as follows:

$$\begin{aligned} F_{S_t^*}\left(s_t^*\right) &= \Pr\left(S_t^* < s_t^*\right) = \Pr\left(\frac{\sigma_t^2}{p-1} Z^* < s_t^*\right) = \Pr\left(Z^* < \frac{p-1}{\sigma_t^2} s_t^*\right) \\ &= F_{Z^*}\left(\frac{p-1}{\sigma_t^2} s_t^*\right) = 1 - Q_{p/2}\left(\sqrt{\lambda}, \sqrt{\left(p-1\right) s_t^*} \Big/ \sigma_t\right) \end{aligned} \tag{86}$$

Based on Equation (86), the reliability function can be derived as

$$\begin{aligned} R^*\left(t; s_{th}, \Theta\right) &= \Pr\left(S_t^* \le s_{th}; \Theta\right) = F_{S_t^*}\left(s_{th}\right) \\ &= 1 - Q_{p/2}\left(\sqrt{\lambda}, \sqrt{\left(p-1\right) s_{th}} \Big/ \sigma_t\right) \end{aligned} \tag{87}$$

Corollary 2 is proved.

APPENDIX 9. Proof of Theorem 1

We first derive the truncation error bound for the location parameter μ, while the truncation error bound for the scale parameter σ can be derived in a similar way.

Define $h_i(\bullet) = g_i^{-1}(\bullet)$ as the inverse function of $g_i(\bullet)$, and let $L = g_1(\mu_b) + \sum_{i=1}^{q} \eta_{i1}\rho_i$ and $R = \sum_{i=q+1}^{+\infty} \eta_{i1}\rho_i$. Then, the location parameter of the lifetime distribution can be written as $\mu = h_1\left(g_1(\mu_b) + \sum_{i=1}^{+\infty} \eta_{i1}\rho_i \right) = h_1(L+R)$.

Assume that the conditional distribution of R on L is $F_{R|L}$. Conditional on the first q components, we have

$$\mathbf{E}\left[\mu \middle| L\right] = \mathbf{E}\left[h_1(L+R) \middle| L\right] = \int h_1(L+\omega)\, dF_{R|L}(\omega) \tag{88}$$

The truncation error can be written as

$$\mathbf{E}\left[\left(\mathbf{E}\left(\mu^* \middle| L\right) - \mu^*\right)^2\right] = \mathbf{E}\left[\int \left(h_1(L+R) - h_1(L+\omega)\right) dF_{R|L}(\omega)\right]^2 \tag{89}$$

In Equation (89), we have

$$\begin{aligned}\left[\int \left(h_1(L+R) - h_1(L+\omega)\right) dF_{R|L}(\omega)\right]^2 &\le \int h_1'(\lambda)^2 (R-\omega)^2\, dF_{R|L}(\omega) \\ &\le 2c_1 \int \left(R^2 + \omega^2\right) dF_{R|L}(\omega)\end{aligned} \tag{90}$$

where c_i for i =1, 2 are bounds that satisfy $\left|h_i'(\bullet)\right|^2 \le c_i$, in which $h_i(\bullet) = g_i^{-1}(\bullet)$ is the inverse function of $g_i(\bullet)$.

By inserting (90) into (89), the truncation error for μ^* can be bounded as

$$\begin{aligned}\mathbf{E}\left[\left(\mathbf{E}\left(\mu^* \middle| L\right) - \mu^*\right)^2\right] &\le 2c_1 \mathbf{E}\left[R^2 + \mathbf{E}\left[R^2 \middle| L\right]\right] \\ &= 4c_1 \mathbf{E}\left(R^2\right) \le 4c_1 \sum_{i=q+1}^{+\infty} \eta_{i1}^2 \sum_{i=q+1}^{+\infty} \delta_i^2\end{aligned} \tag{91}$$

where $\delta_i^2 = E\left(\rho_i^2\right)$.

Following procedures similar to those in Equations (88) - (91), the truncation error for σ^* can be bounded as

$$\mathbf{E}\left[\left(\mathbf{E}\left(\sigma^* \middle| U\right) - \sigma^*\right)^2\right] \le 4c_2 \sum_{i=q+1}^{+\infty} \eta_{i2}^2 \sum_{i=q+1}^{+\infty} \delta_i^2 \tag{92}$$

Summarizing Equations (91) and (92), Theorem 1 is proved.

APPENDIX 10. Proof of Theorem 2

Let $\boldsymbol{\theta}^* = \left[\boldsymbol{\eta}_1^{\mathrm{T}}, \mu_b, \boldsymbol{\eta}_2^{\mathrm{T}}, \sigma_b^*\right]^{\mathrm{T}}$, where $\sigma_b^* = \log(\sigma_b)$. The penalized log-likelihood function in Equation (48) depends on μ_i, σ_i, and a penalty term. Before maximizing the penalized log-likelihood function with respect to $\boldsymbol{\theta}^*$, we derive expressions of μ_i, σ_i, and the penalty in terms of $\boldsymbol{\theta}^*$. The results are summarized in the following Lemma 1 and Lemma 2.

Lemma 1: $\begin{cases} \mu_i = \mathbf{c}_{i1}^{\mathrm{T}}\boldsymbol{\theta}^* \\ \sigma_i = \exp\left(\mathbf{c}_{i2}^{\mathrm{T}}\boldsymbol{\theta}^*\right) \end{cases}$, where $\mathbf{c}_{i1} = \left[\boldsymbol{\rho}_i^{\mathrm{T}}, 1, \mathbf{0}_{q\times1}^{\mathrm{T}}, 0\right]^{\mathrm{T}}$ and $\mathbf{c}_{i2} = \left[\mathbf{0}_{q\times1}^{\mathrm{T}}, 0, \boldsymbol{\rho}_i^{\mathrm{T}}, 1\right]^{\mathrm{T}}$.

Proof of Lemma 1:

Based on Equation (39),

$$\begin{cases} \mu_i = g_1^{-1}\left(\psi_1\left(X_i(r)\right) + g_1(\mu_b)\right) = \psi_1\left(X_i(r)\right) + g_1(\mu_b) \\ \sigma_i = g_2^{-1}\left(\psi_2\left(X_i(r)\right) + g_2(\sigma_b)\right) = \exp\left(\psi_2\left(X_i(r)\right) + \sigma_b^*\right) \end{cases} \tag{93}$$

In Equation (93),

$$\begin{aligned} \psi_j\left(X_i(r)\right) &= \int_0^1 \left(\mathbf{b}^{\mathrm{T}}(r)\boldsymbol{\rho}_i\right)^{\mathrm{T}} \mathbf{b}^{\mathrm{T}}(r)\boldsymbol{\eta}_j dr \\ &= \boldsymbol{\rho}_{\mathrm{i}}^{\mathrm{T}}\left(\int_0^1 \mathbf{b}(r)\mathbf{b}^{\mathrm{T}}(r)dr\right)\boldsymbol{\eta}_j = \boldsymbol{\rho}_{\mathrm{i}}^{\mathrm{T}} I_q \boldsymbol{\eta}_j = \boldsymbol{\rho}_{\mathrm{i}}^{\mathrm{T}}\boldsymbol{\eta}_j \end{aligned} \tag{94}$$

where $\mathbf{b}(r) = \left(b_1(r), b_2(r), ..., b_q(r)\right)^{\mathrm{T}}$ and satisfies $\int_0^1 \mathbf{b}(t)\mathbf{b}^{\mathrm{T}}(t) = I_q$; I_q is a $q\times q$ dimensional identity matrix; $\boldsymbol{\eta}_j = \left(\eta_{1j}, \eta_{2j}, ..., \eta_{qj}\right)^{\mathrm{T}}$; and $\boldsymbol{\rho}_i = \left(\rho_{i1}, \rho_{i2}, ..., \rho_{iq}\right)^{\mathrm{T}}$ is the coefficient vector for sample *i* and satisfies $X_{ic}(r) = \mathbf{b}^{\mathrm{T}}(r)\boldsymbol{\rho}_i$, where $X_{ic}(r)$ denotes the ith censored two-point correlation function.

By inserting Equation (94) into Equation (93), Lemma 1 is proved as follows:

$$\begin{cases} \mu_i = \mu_b + \boldsymbol{\rho}_i^{\mathrm{T}}\boldsymbol{\eta}_1 = \left[\boldsymbol{\rho}_i^{\mathrm{T}}, 1\right]\begin{bmatrix}\boldsymbol{\eta}_1 \\ \mu_b\end{bmatrix} = \left[\boldsymbol{\rho}_i^{\mathrm{T}}, 1, \mathbf{0}_{q\times1}^{\mathrm{T}}, 0\right]\left[\boldsymbol{\eta}_1^{\mathrm{T}}, \mu_b, \boldsymbol{\eta}_2^{\mathrm{T}}, \sigma_b^*\right]^{\mathrm{T}} = \mathbf{c}_{i1}^{\mathrm{T}}\boldsymbol{\theta}^* \\ \sigma_i = \exp\left(\sigma_b^* + \boldsymbol{\rho}_i^{\mathrm{T}}\boldsymbol{\eta}_2\right) = \exp\left(\left[\mathbf{0}_{q\times1}^{\mathrm{T}}, 0, \boldsymbol{\rho}_i^{\mathrm{T}}, 1\right]\left[\boldsymbol{\eta}_1^{\mathrm{T}}, \mu_b, \boldsymbol{\eta}_2^{\mathrm{T}}, \sigma_b^*\right]^{\mathrm{T}}\right) = \exp\left(\mathbf{c}_{i2}^{\mathrm{T}}\boldsymbol{\theta}^*\right) \end{cases} \tag{95}$$

Lemma 2: The penalty term $\sum_{j=1}^{2}\lambda_j\boldsymbol{\eta}_j^{\mathrm{T}}\boldsymbol{\omega}\boldsymbol{\eta}_j = \boldsymbol{\theta}^{*\mathrm{T}}\boldsymbol{\Omega}\boldsymbol{\theta}^*$, where $\boldsymbol{\Omega}$ is a matrix defined in Equation

(51).

Proof of Lemma 2:

Let $\boldsymbol{\beta}_i = \beta_i(\mathbf{r})$ be the vector of the evaluations of function $\beta_i(r)$ at the values $\mathbf{r} = (r_1, r_2, \ldots, r_m)$. Let $\mathbf{B}$ be an $m \times q$ matrix containing as its columns the m-vectors of the evaluations of functions $b_i(r)$ for i=1, 2, …, q at $\mathbf{r}$. Then $\boldsymbol{\beta}_j$ can be expressed as $\boldsymbol{\beta}_j = \mathbf{B}\boldsymbol{\eta}_j$. Let $\boldsymbol{\omega}$ be the $q \times q$ matrix of inner products of the second derivatives of the spline basis functions, with its $(u,v)^{\text{th}}$ entry given by

$$\boldsymbol{\omega}_{uv} = \int_0^1 b_u''(r) b_v''(r)\, dr \tag{96}$$

Based on (96), Lemma 2 is proved as follows:

$$\sum_{j=1}^{2} \lambda_j \int_0^{+\infty} \beta_j''(r)^2\, dr = \sum_{j=1}^{2} \lambda_j \boldsymbol{\eta}_j^{\mathrm{T}} \boldsymbol{\omega} \boldsymbol{\eta}_j = \left[\boldsymbol{\eta}_1^{\mathrm{T}}, \mu_b, \boldsymbol{\eta}_2^{\mathrm{T}}, \sigma_b^*\right] \boldsymbol{\Omega} \left[\boldsymbol{\eta}_1^{\mathrm{T}}, \mu_b, \boldsymbol{\eta}_2^{\mathrm{T}}, \sigma_b^*\right]^{\mathrm{T}} = \boldsymbol{\theta}^{*\mathrm{T}} \boldsymbol{\Omega} \boldsymbol{\theta}^* \tag{97}$$

where $\boldsymbol{\Omega}$ is defined in Equation (51).

Based on Lemma 1 and Lemma 2, $\boldsymbol{\theta}^*$ can be estimated by solving:

$$\partial l_p\left(\boldsymbol{\theta}^* \middle| \mathbf{y}\right) \Big/ \partial \boldsymbol{\theta}^* = \partial l\left(\boldsymbol{\theta}^* \middle| \mathbf{y}\right) \Big/ \partial \boldsymbol{\theta}^* - \partial\left(\boldsymbol{\theta}^{*\mathrm{T}} \boldsymbol{\Omega} \boldsymbol{\theta}^*\right) \Big/ \partial \boldsymbol{\theta}^* = \mathbf{0}_{(2q+2)\times 1} \tag{98}$$

where and $\mathbf{0}_{i\times j}$ is a $i \times j$ dimensional matrix with all elements equaling 0.

Equation (98) can be further derived as

$$\frac{\partial l_p\left(\boldsymbol{\theta}^* \middle| \mathbf{y}\right)}{\partial \boldsymbol{\theta}^*} = \sum_{i=1}^{N} \left[\frac{\partial l\left(\boldsymbol{\theta}^* \middle| \mathbf{y}\right)}{\partial \mu_i} \times \frac{\partial \mu_i}{\partial \boldsymbol{\theta}^*} + \frac{\partial l\left(\boldsymbol{\theta}^* \middle| \mathbf{y}\right)}{\partial \sigma_i} \times \frac{\partial \sigma_i}{\partial \boldsymbol{\theta}^*} \right] - 2\boldsymbol{\Omega}\boldsymbol{\theta}^* = \mathbf{0}_{(2q+2)\times 1} \tag{99}$$

Next, by inserting the results from Lemma 1 and Lemma 2 into Equation (99), we obtain

$$\sum_{i=1}^{N} \left[\frac{y_i - \mathbf{c}_{i1}^{\mathrm{T}} \boldsymbol{\theta}^*}{\exp\left(2\mathbf{c}_{i2}^{\mathrm{T}} \boldsymbol{\theta}^*\right)} \times \mathbf{c}_{i1} \right] + \sum_{i=1}^{N} \left\{ \left[-1 + \frac{\left(y_i - \mathbf{c}_{i1}^{\mathrm{T}} \boldsymbol{\theta}^*\right)^2}{\exp\left(2\mathbf{c}_{i2}^{\mathrm{T}} \boldsymbol{\theta}^*\right)} \right] \times \mathbf{c}_{i2} \right\} - 2\boldsymbol{\Omega}\boldsymbol{\theta}^* = \mathbf{0}_{(2q+2)\times 1} \tag{100}$$

Further, we derive Equation (100) into a matrix form. Specifically, the first item in Equation (100) can be written as

$$\sum_{i=1}^{N}\left[\frac{y_i-\mathbf{c}_{i1}^{\mathrm{T}}\boldsymbol{\theta}^*}{\exp\left(2\mathbf{c}_{i2}^{\mathrm{T}}\boldsymbol{\theta}^*\right)}\times\mathbf{c}_{i1}\right]=\left[\mathbf{c}_{11},\mathbf{c}_{21},\ldots,\mathbf{c}_{N1}\right]\left[k_1,k_2,\ldots,k_N\right]^{\mathrm{T}}=\mathbf{C}_1\mathbf{k}$$
$$=\mathbf{C}_1\left(\mathbf{y}-\mathbf{C}_1^{\mathrm{T}}\boldsymbol{\theta}^*\right)\circ\exp\left(-2\mathbf{C}_2^{\mathrm{T}}\boldsymbol{\theta}^*\right) \tag{101}$$

where $\mathbf{C}_i=\left[\mathbf{c}_{1i},\mathbf{c}_{2i},\ldots,\mathbf{c}_{Ni}\right]$; $k_i=\left(y_i-\mathbf{c}_{i1}^{\mathrm{T}}\boldsymbol{\theta}^*\right)\exp\left(-2\mathbf{c}_{i2}^{\mathrm{T}}\boldsymbol{\theta}^*\right)$; $\mathbf{k}=\left(\mathbf{y}-\mathbf{C}_1^{\mathrm{T}}\boldsymbol{\theta}^*\right)\circ\exp\left(-2\mathbf{C}_2^{\mathrm{T}}\boldsymbol{\theta}^*\right)$; and "○" is the Hadamard operator [120] defined in Equation (51).Similarly, the second item in Equation (100) can be written as

$$\sum_{i=1}^{N}\left\{\left[-1+\frac{\left(y_i-\mathbf{c}_{i1}^{\mathrm{T}}\boldsymbol{\theta}^*\right)^2}{\exp\left(2\mathbf{c}_{i2}^{\mathrm{T}}\boldsymbol{\theta}^*\right)}\right]\times\mathbf{c}_{i2}\right\}=\left[\mathbf{c}_{12},\mathbf{c}_{22},\ldots,\mathbf{c}_{N2}\right]\left[k_1^*,k_2^*,\ldots,k_N^*\right]^{\mathrm{T}}=\mathbf{C}_2\mathbf{k}^*$$
$$=\mathbf{C}_2\left(\left(\mathbf{y}-\mathbf{C}_1^{\mathrm{T}}\boldsymbol{\theta}^*\right)^{\circ 2}\circ\exp\left[\circ\left(-2\mathbf{C}_2^{\mathrm{T}}\boldsymbol{\theta}^*\right)\right]-\mathbf{1}\right) \tag{102}$$

where $\mathbf{k}^*=\left(\mathbf{y}-\mathbf{C}_1^{\mathrm{T}}\boldsymbol{\theta}^*\right)^{\circ 2}\circ\exp\left[\circ\left(-2\mathbf{C}_2^{\mathrm{T}}\boldsymbol{\theta}^*\right)\right]-\mathbf{1}$, and $\mathbf{1}$ is an N-dimensional unit column vector.

By inserting Equations (101) and (102) into Equation (100), Theorem 2 is proved.

REFERENCES

[1] M. Kijima, "Some results for repairable systems with general repair," *Journal of Applied Probability,* vol. 26, no. 01, pp. 89-102, 1989.

[2] Y. Hong, W. Q. Meeker, and J. D. McCalley, "Prediction of remaining life of power transformers based on left truncated and right censored lifetime data," *The Annals of Applied Statistics,* vol. 3, no. 2, pp. 857-879, 2009.

[3] W. Zhao, and E. A. Elsayed, "A general accelerated life model for step-stress testing," *IIE Transactions,* vol. 37, no. 11, pp. 1059-1069, 2005.

[4] G. L. Gilardoni, and E. A. Colosimo, "Optimal maintenance time for repairable systems," *Journal of Quality Technology,* vol. 39, no. 1, pp. 48-53, 2007.

[5] N. Zhang, and Q. Yang, "Optimal maintenance planning for repairable multi-component systems subject to dependent competing risks," *IIE Transactions,* vol. 47, no. 5, pp. 521-532, 2015.

[6] Y. Hong, and W. Q. Meeker, "Field-failure predictions based on failure-time data with dynamic covariate information," *Technometrics,* vol. 55, no. 2, pp. 135-149, 2013.

[7] C. J. Lu, and W. O. Meeker, "Using degradation measures to estimate a time-to-failure distribution," *Technometrics,* vol. 35, no. 2, pp. 161-174, 1993.

[8] Q. Yang, Y. Hong, Y. Chen, and J. Shi, "Failure profile analysis of complex repairable systems with multiple failure modes," *IEEE Transactions on Reliability,* vol. 61, no. 1, pp. 180-191, 2012.

[9] Q. Yang, N. Zhang, and Y. Hong, "Reliability analysis of repairable systems with dependent component failures under partially perfect repair," *IEEE Transactions on*

Reliability, vol. 62, no. 2, pp. 490-498, 2013.

[10] W. Si, and Q. Yang, "A Generalized Mixed Effect Kijima Model and Application in Optimal Maintenance Planning," *IEEE Transactions on Reliability,* vol. 65, no. 3, pp. 1551-1561, 2016.

[11] J. F. Lawless, *Statistical models and methods for lifetime data*: John Wiley & Sons, New York, NY, 2011.

[12] W. Si, and Q. Yang, "Accelerated Life Testing With Semiparametric Modeling of Stress Effects," *IEEE Transactions on Reliability,* vol. 66, no. 4, pp. 989-996, 2017.

[13] Z.-S. Ye, Y. Wang, K.-L. Tsui, and M. Pecht, "Degradation data analysis using Wiener processes with measurement errors," *IEEE Transactions on Reliability,* vol. 62, no. 4, pp. 772-780, 2013.

[14] Z. Pan, and N. Balakrishnan, "Reliability modeling of degradation of products with multiple performance characteristics based on gamma processes," *Reliability Engineering & System Safety,* vol. 96, no. 8, pp. 949-957, 2011.

[15] Z.-S. Ye, and N. Chen, "The inverse Gaussian process as a degradation model," *Technometrics,* vol. 56, no. 3, pp. 302-311, 2014.

[16] H. Liao, and Z. Tian, "A framework for predicting the remaining useful life of a single unit under time-varying operating conditions," *IIE Transactions,* vol. 45, no. 9, pp. 964-980, 2013.

[17] N. Chen, Y. Chen, Z. Li, S. Zhou, and C. Sievenpiper, "Optimal variability sensitive condition-based maintenance with a Cox PH model," *International Journal of Production Research,* vol. 49, no. 7, pp. 2083-2100, 2011.

[18] J. Lankford, and D. Davidson, "Fatigue crack tip plasticity associated with overloads and subsequent cycling," *Journal of Engineering Materials and Technology,* vol. 98, no. 1, pp. 17-23, 1976.

[19] S. Daneshpour, J. Dyck, V. Ventzke, and N. Huber, "Crack retardation mechanism due to overload in base material and laser welds of Al alloys," *International Journal of Fatigue,* vol. 42, pp. 95-103, 2012.

[20] J. Dominguez, J. Zapatero, and B. Moreno, "A statistical model for fatigue crack growth under random loads including retardation effects," *Engineering Fracture Mechanics,* vol. 62, no. 4-5, pp. 351-369, 1999.

[21] Y. Hashimoto, H. Hata, M. Sakai, and H. Negishi, "Local deformation and buckling of a cylindrical Al tube under magnetic impulsive pressure," *Journal of Materials Processing Technology,* vol. 85, no. 1, pp. 209-212, 1999.

[22] O. Kolednik, "The characterization of local deformation and fracture properties–a tool for advanced materials design," *Advanced Engineering Materials,* vol. 8, no. 11, pp. 1079-1083, 2006.

[23] M. Springmann, and M. Kuna, "Determination of ductile damage parameters by local deformation fields: measurement and simulation," *Archive of Applied Mechanics,* vol. 75, no. 10-12, pp. 775-797, 2006.

[24] O. Modi, P. Pandit, D. Mondal, B. Prasad, A. Yegneswaran, and A. Chrysanthou, "High-stress abrasive wear response of 0.2% carbon dual phase steel: Effects of microstructural features and experimental conditions," *Materials Science and Engineering: A,* vol. 458, no. 1, pp. 303-311, 2007.

[25] M. Sarwar, and R. Priestner, “Influence of ferrite-martensite microstructural morphology on tensile properties of dual-phase steel,” *Journal of Materials Science,* vol. 31, no. 8, pp. 2091-2095, 1996.

[26] A. Carpinteri, “Fractal nature of material microstructure and size effects on apparent mechanical properties,” *Mechanics of Materials,* vol. 18, no. 2, pp. 89-101, 1994.

[27] F. C. Campbell, *Elements of metallurgy and engineering alloys*, Materials Park, OH: ASM International, 2008.

[28] S.-B. Lee, “Fatigue failure of welded vertical members of a steel truss bridge,” *Engineering Failure Analysis,* vol. 3, no. 2, pp. 103-108, 1996.

[29] R. Smith, “Railway fatigue failures: an overview of a long standing problem,” *Materialwissenschaft und Werkstofftechnik,* vol. 36, no. 11, pp. 697-705, 2005.

[30] K. Macdonald, *Fracture and fatigue of welded joints and structures*: Woodhead Publishing, Oxford, UK, 2011.

[31] R. O. Ritchie, “Mechanisms of fatigue-crack propagation in ductile and brittle solids,” *International Journal of Fracture,* vol. 100, no. 1, pp. 55-83, 1999.

[32] K. Gotoh, M. Takuno, K. Okada, and S. Kusuba, "Numerical Simulation of Fatigue Crack Growth of a Welded Structural Component Under Block Program Fatigue Test," in Proceedings of the ASME 33rd International Conference on Ocean, Offshore and Arctic Engineering, American Society of Mechanical Engineers, San Francisco, CA, pp. V005T03A011–V005T03A011,2014.

[33] S. A. Kumar, A. Bhattacharya, and N. C. M. Babu, “Fatigue crack growth life prediction around cold expanded hole using finite element method,” *Procedia Materials Science,*

vol. 5, no. 0, pp. 316-325, 2014.

[34] Y. K. Lin, and J. N. Yang, “A stochastic theory of fatigue crack propagation,” *AIAA Journal,* vol. 23, no. 1, pp. 117-124, 1985.

[35] E. Çinlar, "Fatigue Crack Growth," *Reliability and Maintenance of Complex Systems*: Springer, Berlin, Germany, pp. 37-52, 1996.

[36] J. Lawless, and M. Crowder, “Covariates and random effects in a gamma process model with application to degradation and failure,” *Lifetime Data Analysis,* vol. 10, no. 3, pp. 213-227, 2004.

[37] R. R. Zhou, N. Serban, and N. Gebraeel, “Degradation modeling applied to residual lifetime prediction using functional data analysis,” *The Annals of Applied Statistics,* vol. 5, no. 2B, pp. 1586-1610, 2011.

[38] P. Paris, and F. Erdogan, “A critical analysis of crack propagation laws,” *Journal of Fluids Engineering,* vol. 85, no. 4, pp. 528-533, 1963.

[39] P. Dai, S. Li, and Z. H. Li, “The effects of overload on the fatigue crack growth in ductile materials predicted by plasticity-corrected stress intensity factor,” *Engineering Fracture Mechanics,* vol. 111, pp. 26-37, 2013.

[40] C. Shin, and N. Fleck, “Overload retardation in a structural steel,” *Fatigue & Fracture of Engineering Materials & Structures,* vol. 9, no. 5, pp. 379-393, 1987.

[41] C. Shin, and S. Hsu, “On the mechanisms and behaviour of overload retardation in AISI 304 stainless steel,” *International Journal of Fatigue,* vol. 15, no. 3, pp. 181-192, 1993.

[42] P. Bernard, T. Lindley, and C. Richards, “The effect of single overloads on fatigue-crack propagation in steels,” *Metal Science,* vol. 11, no. 8-9, pp. 390-398, 1977.

[43] M. Skorupa, “Load interaction effects during fatigue crack growth under variable amplitude loading - a literature review. Part I: empirical trends,” *Fatigue & Fracture of Engineering Materials & Structures,* vol. 21, no. 8, pp. 987-1006, 08, 1998.

[44] M. Skorupa, “Load interaction effects during fatigue crack growth under variable amplitude loading—a literature review. Part II: qualitative interpretation,” *Fatigue & Fracture of Engineering Materials & Structures,* vol. 22, no. 10, pp. 905-926, 1999.

[45] J. Chang, M. Szamossi, and K. Liu, “Random spectrum fatigue crack life predictions with or without considering load interactions,” *ASTM STP,* vol. 748, pp. 115-132, 1981.

[46] R. I. Stephens, A. Fatemi, R. R. Stephens, and H. O. Fuchs, *Metal Fatigue in Engineering*, 2nd ed: John Wiley & Sons, New York, NY, 2000.

[47] J. K. Kim, and D. S. Shim, “A statistical approach for predicting the crack retardation due to a single tensile overload,” *International Journal of Fatigue,* vol. 25, no. 4, pp. 335-342, 2003.

[48] W. Q. Meeker, L. A. Escobar, and C. J. Lu, “Accelerated degradation tests: modeling and analysis,” *Technometrics,* vol. 40, no. 2, pp. 89-99, 1998.

[49] A. Lehmann, “Joint modeling of degradation and failure time data,” *Journal of Statistical Planning and Inference,* vol. 139, no. 5, pp. 1693-1706, 2009.

[50] N. Gorjian, L. Ma, M. Mittinty, P. Yarlagadda, and Y. Sun, "A review on degradation models in reliability analysis," Engineering Asset Lifecycle Management: *Proceedings of the 4th World Congress on Engineering Asset Management* (WCEAM 2009), Springer London, London, pp. 369–384, 2009.

[51] C. P. Tsokos, "Parametric and nonparametric reliability analysis," *International*

Encyclopedia of Statistical Science, Springer, Berlin, Germany, pp. 1048–105, 2011.

[52] Q. Yang, and Y. Chen, "Monte Carlo methods for reliability evaluation of linear sensor systems," *IEEE Transactions on Reliability,* vol. 60, no. 1, pp. 305-314, 2011.

[53] W. Q. Meeker, and L. A. Escobar, "A review of recent research and current issues in accelerated testing," *International Statistical Review*, vol. 61, no. 1, pp. 147-168, 1993.

[54] Y. Liu, and S. Mahadevan, "Probabilistic fatigue life prediction using an equivalent initial flaw size distribution," *International Journal of Fatigue,* vol. 31, no. 3, pp. 476-487, 2009.

[55] Q. Yang, and Y. Chen, "Sensor system reliability modeling and analysis for fault diagnosis in multistage manufacturing processes," *IIE Transactions,* vol. 41, no. 9, pp. 819-830, 2009.

[56] Q. Yang, and J. Jin, "Separation of individual operation signals from mixed sensor measurements," *IIE Transactions,* vol. 44, no. 9, pp. 780-792, 2012.

[57] Y.-L. Lee, *Fatigue testing and analysis: theory and practice*: Butterworth-Heinemann, 2005.

[58] C. Y. Kim, J. M. Choi, and J. H. Song, "Fatigue crack growth and closure behavior under random loadings in 7475-T7351 aluminum alloy," *International Journal of Fatigue,* vol. 47, pp. 196-204, 2013.

[59] B. Yuen, and F. Taheri, "Proposed modifications to the Wheeler retardation model for multiple overloading fatigue life prediction," *International Journal of Fatigue,* vol. 28, no. 12, pp. 1803-1819, 2006.

[60] C. Shin, and C. Cai, "Experimental and finite element analyses on stress intensity

factors of an elliptical surface crack in a circular shaft under tension and bending," *International Journal of Fracture,* vol. 129, no. 3, pp. 239-264, 2004.

[61] G. H. Hardy, J. E. Littlewood, and G. Pólya, *Inequalities*: Cambridge University Press, New York, NY, 1952.

[62] G. Casella, and R. L. Berger, *Statistical Inference*: Duxbury Pacific Grove, CA, 2002.

[63] L. E. Papke, and J. M. Wooldridge, "A computational trick for delta-method standard errors," *Economics Letters,* vol. 86, no. 3, pp. 413-417, 2005.

[64] M. R. Chernick, *Bootstrap methods: A guide for practitioners and researchers*: John Wiley & Sons, New York, NY, 2011.

[65] G. C. Sih, *Handbook of stress-intensity factors*: Institute of Fracture and Solid Mechanics, Lehigh University, Bethlehem, PA, 1973.

[66] W. Si, Q. Yang, and X. Wu, "A physical–statistical model of overload retardation for crack propagation and application in reliability estimation," *IIE Transactions,* vol. 48, no. 4, pp. 347-358, 2016.

[67] Z. Song, and G. Sih, "Crack initiation behavior in magnetoelectroelastic composite under in-plane deformation," *Theoretical and Applied Fracture Mechanics,* vol. 39, no. 3, pp. 189-207, 2003.

[68] H. Mughrabi, H. Höppel, and M. Kautz, "Fatigue and microstructure of ultrafine-grained metals produced by severe plastic deformation," *Scripta Materialia,* vol. 51, no. 8, pp. 807-812, 2004.

[69] J. Clayton, "Deformation, fracture, and fragmentation in brittle geologic solids," *International Journal of Fracture,* vol. 163, no. 1, pp. 151-172, 2010.

[70] O. Kolednik, and K. Unterweger, “The ductility of metal matrix composites–Relation to local deformation behavior and damage evolution,” *Engineering Fracture Mechanics,* vol. 75, no. 12, pp. 3663-3676, 2008.

[71] M. Müller, L. McMillan, J. Dorsey, and R. Jagnow, "Real-time simulation of deformation and fracture of stiff materials," *Proceedings of the Eurographic Workshop on Computer Animation and Simulation,* pp. 113–124, 2001.

[72] H. S. Kim, “Finite element analysis of deformation behaviour of metals during equal channel multi-angular pressing,” *Materials Science and Engineering: A,* vol. 328, no. 1, pp. 317-323, 2002.

[73] Q. Yang, N. Zhang, and Y. Hong, “Reliability analysis of repairable systems with dependent component failures under partially perfect repair,” *IEEE Transactions on Reliability,* vol. 62, no. 2, pp. 490-498, 2013.

[74] W. Si, Q. Yang, and X. Wu, “A Distribution-based Functional Linear Model for Reliability Analysis of Advanced High Strength Dual-phase Steels by Utilizing Material Microstructure Images,” *IISE Transactions,* vol. 49, no. 9, pp. 863-873, 2017.

[75] W. Si, E. Love, and Q. Yang, “Two-state optimal maintenance planning of repairable systems with covariate effects,” *Computers & Operations Research,* vol. 92, pp. 17-25, 2018.

[76] Y. Hong, Y. Duan, W. Q. Meeker, D. L. Stanley, and X. Gu, “Statistical methods for degradation data with dynamic covariates information and an application to outdoor weathering data,” *Technometrics,* vol. 57, no. 2, pp. 180-193, 2015.

[77] Z. Xu, Y. Hong, and R. Jin, “Nonlinear general path models for degradation data with

dynamic covariates," *Applied Stochastic Models in Business and Industry,* vol. 32, no. 2, pp. 153-167, 2016.

[78] J. P. Kharoufeh, and S. M. Cox, "Stochastic models for degradation-based reliability," *IIE Transactions,* vol. 37, no. 6, pp. 533-542, 2005.

[79] X. Wang, "Wiener processes with random effects for degradation data," *Journal of Multivariate Analysis,* vol. 101, no. 2, pp. 340-351, 2010.

[80] W. Q. Meeker, and Y. Hong, "Reliability meets big data: opportunities and challenges," *Quality Engineering,* vol. 26, no. 1, pp. 102-116, 2014.

[81] E. J. Hearn, *Mechanics of Materials 2: The mechanics of elastic and plastic deformation of solids and structural materials*, Oxford: Butterworth-Heinemann, UK, 1997.

[82] N. Laird, and N. Lange, "[Prediction of future observations in growth curve models]: comment," *Statistical Science,* vol. 2, no. 4, pp. 451-454, 1987.

[83] C. Park, and W. Padgett, "Accelerated degradation models for failure based on geometric Brownian motion and gamma processes," *Lifetime Data Analysis,* vol. 11, no. 4, pp. 511-527, 2005.

[84] C.-H. Hsueh, "Modeling of elastic deformation of multilayers due to residual stresses and external bending," *Journal of Applied Physics,* vol. 91, no. 12, pp. 9652-9656, 2002.

[85] C.-A. Martínez, and L.-F. Blázquez, "Distribution of a sum of weighted noncentral chi-square variables," *Test,* vol. 14, no. 2, pp. 397-415, 2005.

[86] K. Ogi, and N. Takeda, "Effects of moisture content on nonlinear deformation behavior of CF/epoxy composites," *Journal of Composite Materials,* vol. 31, no. 6, pp. 530-551,

1997.

[87] Y. Wu, H. Li, G. Chen, X. Hui, B. Wang, and Z. Lu, "Nonlinear tensile deformation behavior of small-sized metallic glasses," *Scripta Materialia,* vol. 61, no. 6, pp. 564-567, 2009.

[88] F.-K. Wang, and T.-P. Chu, "Lifetime predictions of LED-based light bars by accelerated degradation test," *Microelectronics Reliability,* vol. 52, no. 7, pp. 1332-1336, 2012.

[89] M. A. Alam, and S. Mahapatra, "A comprehensive model of PMOS NBTI degradation," *Microelectronics Reliability,* vol. 45, no. 1, pp. 71-81, 2005.

[90] H. Ghadbeigi, C. Pinna, S. Celotto, and J. Yates, "Local plastic strain evolution in a high strength dual-phase steel," *Materials Science and Engineering: A,* vol. 527, no. 18, pp. 5026-5032, 2010.

[91] N. Zhang, and Q. Yang, "A random effect autologistic regression model with application to the characterization of multiple microstructure samples," *IIE Transactions,* vol. 48, no. 1, pp. 34-42, 2016.

[92] ASTM Standard E8/E8M, *Standard test methods for tension testing of metallic materials,* West Conshohocken, PA: ASTM International, 2013.

[93] N. McCormick, and J. Lord, "Digital image correlation," *Materials today,* vol. 13, no. 12, pp. 52-54, 2010.

[94] Q. Huang, N. J. Alvarez, A. Shabbir, and O. Hassager, "Multiple Cracks Propagate Simultaneously in Polymer Liquids in Tension," *Physical Review Letters,* vol. 117, no. 8, pp. 087801, 2016.

[95] D. Xu, Q. Wei, E. A. Elsayed, Y. Chen, and R. Kang, “Multivariate degradation modeling of smart electricity meter with multiple performance characteristics via vine copulas,” *Quality and Reliability Engineering International,* vol. 33, no. 4, pp. 803-821, 2017.

[96] W. Si, Q. Yang, X. Wu, and Y. Chen, “Reliability analysis by considering dynamic material local deformation,” *Journal of Quality Technology,* vol. 50, no. 2, pp. 183-197, 2018.

[97] D. A. Hughes, and N. Hansen, "9: Metallography and Microstructures," *ASM International,* Materials Park, OH, pp. 192-206, 2004.

[98] A. Dasgupta, and M. Pecht, “Material failure mechanisms and damage models,” *IEEE Transactions on Reliability,* vol. 40, no. 5, pp. 531-536, 1991.

[99] C. Mukhopadhyay, “Maximum likelihood analysis of masked series system lifetime data,” *Journal of Statistical Planning and Inference,* vol. 136, no. 3, pp. 803-838, 2006.

[100] G. M. James, J. Wang, and J. Zhu, “Functional linear regression that's interpretable,” *The Annals of Statistics,* vol. 37, no. 5, pp. 2083-2108, 2009.

[101] Y. Jiao, F. Stillinger, and S. Torquato, “Modeling heterogeneous materials via two-point correlation functions: Basic principles,” *Physical Review E,* vol. 76, no. 3, pp. 031110, 2007.

[102] S. Lin, H. Garmestani, and B. Adams, “The evolution of probability functions in an inelasticly deforming two-phase medium,” *International Journal of Solids and Structures,* vol. 37, no. 3, pp. 423-434, 2000.

[103] A. Tewari, A. Gokhale, J. Spowart, and D. Miracle, “Quantitative characterization of

spatial clustering in three-dimensional microstructures using two-point correlation functions," *Acta Materialia,* vol. 52, no. 2, pp. 307-319, 2004.

[104] A. K. Wong, and P. K. Sahoo, "A gray-level threshold selection method based on maximum entropy principle," *IEEE Transactions on Systems, Man, and Cybernetics,* vol. 19, no. 4, pp. 866-871, 1989.

[105] J. C. Russ, and R. P. Woods, "The image processing handbook," *Journal of Computer Assisted Tomography,* vol. 19, no. 6, pp. 979-981, 1995.

[106] C.-H. Jun, S. Balamurali, and S.-H. Lee, "Variables sampling plans for Weibull distributed lifetimes under sudden death testing," *IEEE Transactions on Reliability,* vol. 55, no. 1, pp. 53-58, 2006.

[107] W. Q. Meeker, and L. A. Escobar, *Statistical methods for reliability data*: John Wiley & Sons, New York, NY, 2014.

[108] G. M. James, "Generalized linear models with functional predictors," *Journal of the Royal Statistical Society: Series B (Statistical Methodology),* vol. 64, no. 3, pp. 411-432, 2002.

[109] T. T. Cai, and P. Hall, "Prediction in functional linear regression," *The Annals of Statistics,* vol. 34, no. 5, pp. 2159-2179, 2006.

[110] M. Yuan, and T. T. Cai, "A reproducing kernel Hilbert space approach to functional linear regression," *The Annals of Statistics,* vol. 38, no. 6, pp. 3412-3444, 2010.

[111] Y. Wu, J. Fan, and H.-G. Müller, "Varying-coefficient functional linear regression," *Bernoulli,* vol. 16, no. 3, pp. 730-758, 2010.

[112] H.-G. Müller, and U. Stadtmüller, "Generalized functional linear models," *Annals of*

Statistics, vol. 33, no. 2, pp. 774-805, 2005.

[113] S. N. Wood, "Stable and efficient multiple smoothing parameter estimation for generalized additive models," *Journal of the American Statistical Association,* vol. 99, no. 467, pp. 673–686, 2004.

[114] S. N. Wood, "Fast stable restricted maximum likelihood and marginal likelihood estimation of semiparametric generalized linear models," *Journal of the Royal Statistical Society: Series B (Statistical Methodology),* vol. 73, no. 1, pp. 3-36, 2011.

[115] V. Rondeau, D. Commenges, and P. Joly, "Maximum penalized likelihood estimation in a gamma-frailty model," *Lifetime Data Analysis,* vol. 9, no. 2, pp. 139-153, 2003.

[116] R. A. Rigby, and D. M. Stasinopoulos, "Generalized additive models for location, scale and shape," *Journal of the Royal Statistical Society: Series C (Applied Statistics),* vol. 54, no. 3, pp. 507-554, 2005.

[117] B. W. Silverman, "Some aspects of the spline smoothing approach to non-parametric regression curve fitting," *Journal of the Royal Statistical Society. Series B (Methodological),* vol. 47, no. 1, pp. 1-52, 1985.

[118] Y. Yu, and D. Ruppert, "Penalized spline estimation for partially linear single-index models," *Journal of the American Statistical Association,* vol. 97, no. 460, pp. 1042-1054, 2002.

[119] D. M. Stasinopoulos, and R. A. Rigby, "Generalized additive models for location scale and shape (GAMLSS) in R," *Journal of Statistical Software,* vol. 23, no. 7, pp. 1-46, 2007.

[120] R. Reams, "Hadamard inverses, square roots and products of almost semidefinite

matrices," *Linear Algebra and its Applications,* vol. 288, pp. 35-43, 1999.

[121] Y. Jiao, F. Stillinger, and S. Torquato, "Modeling heterogeneous materials via two-point correlation functions. II. Algorithmic details and applications," *Physical Review E,* vol. 77, no. 3, pp. 031135, 2008.

[122] A. D. Kammers, and S. Daly, "Digital image correlation under scanning electron microscopy: methodology and validation," *Experimental Mechanics,* vol. 53, no. 9, pp. 1743-1761, 2013.

[123] L. A. Carlsson, D. F. Adams, and R. B. Pipes, *Experimental characterization of advanced composite materials*, 4th ed., Boca Raton: CRC press, FL, 2014.

[124] A. Tishler, and I. Zang, "A maximum likelihood method for piecewise regression models with a continuous dependent variable," *Journal of the Royal Statistical Society. Series C (Applied Statistics),* vol. 30, no. 2, pp. 116-124, 1981.

[125] G. Seber, and C. Wild, *Nonlinear regression*: Wiley, New York, NY, 1989.

[126] A. M. Mathai, and S. B. Provost, *Quadratic forms in random variables: theory and applications*: M. Dekker, New York, NY, 1992.

[127] M. K. Simon, *Probability distributions involving Gaussian random variables: A handbook for engineers and scientists*: Springer, New York, NY, 2006.

ABSTRACT

RELIABILITY ANALYSIS BY CONSIDERING STEEL PHYSICAL PROPERTIES

by

WUJUN SI

August 2018

Advisor: Dr. Qingyu Yang

Co-advisor: Dr. Xin Wu

Major: Industrial Engineering

Degree: Doctor of Philosophy

Most customers today are pursuing engineering materials (e.g., steel) that not only can achieve their expected functions but also are highly reliable. As a result, reliability analysis of materials has been receiving increasing attention over the past few decades. Most existing studies in the reliability engineering field focus on developing model-based and data-driven approaches to analyze material reliability based on material failure data such as lifetime data and degradation data, without considering effects of material physical properties. Ignoring such effects may result in a biased estimation of material reliability, which in turn could incur higher operation or maintenance costs.

Recently, with the advancement of sensor technology more information/data concerning various physical properties of materials are accessible to reliability researchers. In this dissertation, considering the significant impacts of steel physical properties on steel failures, we propose systematic methodologies for steel reliability analysis by integrating a set of steel physical properties. Specifically, three steel properties of various scales are considered: 1) a

macro-scale property called overload retardation; 2) a local-scale property called dynamic local deformation; and 3) a micro-scale property called microstructure effect. For incorporating property 1), a novel physical-statistical model is proposed based on a modification of the current Paris law. To incorporate property 2), a novel statistical model named multivariate general path model is proposed, which is a generalization of an existing univariate general path model. For the integration of property 3), a novel statistical model named distribution-based functional linear model is proposed, which is a generalization of an existing functional linear model. Theoretical property analyses and statistical inferences of these three models are intensively developed.

Various simulation studies are implemented to verify and illustrate the proposed methodologies. Multiple physical experiments are designed and conducted to demonstrate the proposed models. The results show that, through the integration of the aforementioned three steel physical properties, a significant improvement of steel reliability assessment is achieved in terms of failure prediction accuracy compared to traditional reliability studies.

AUTOBIOGRAPHICAL STATEMENT

Wujun Si is currently a doctoral candidate in the department of industrial and systems engineering at Wayne State University. He received a B.Eng. degree in mechanical engineering from the University of Science and Technology of China, Hefei, China, in 2013. His primary research interests include data analytics, statistical methods in reliability and quality engineering, optimal maintenance scheduling and decision making for complex manufacturing and production systems. His research work has been published in *IISE Transactions*, *IEEE Transactions on Reliability*, *Journal of Quality Technology* and *Computers & Operations Research*. He is the awardee of the 2016 ISERC best student paper competition in the Quality Control & Reliability Engineering (QCRE) division, and the recipient of the finalist award of 2017 INFORMS best refereed paper competition in the Quality, Statistics and Reliability (QSR) division. Wujun will start as an assistant professor in the department of industrial, systems, and manufacturing engineering at Wichita State University in Fall 2018.